GEOGRID-SOIL INTERACTION COEFFICIENTS FOR SEISMIC DESIGN

by

SHANE M. DUCKWORTH

B.A.Sc., The University of British Columbia, 1998

A THESIS SUBMITTED IN PARTIAL FULFILMENT OF
THE REQUIREMENTS FOR THE DEGREE OF

MASTER OF APPLIED SCIENCE

in

THE FACULTY OF GRADUATE STUDIES

Department of Civil Engineering

We accept this thesis as conforming
to the required standard

THE UNIVERSITY OF BRITISH COLUMBIA

December 2000

© Shane M. Duckworth, 2000

In presenting this thesis in partial fulfilment of the requirements for an advanced degree at the University of British Columbia, I agree that the Library shall make it freely available for reference and study. I further agree that permission for extensive copying of this thesis for scholarly purposes may be granted by the head of my department or by his or her representatives. It is understood that copying or publication of this thesis for financial gain shall not be allowed without my written permission.

4 DEC 2000.

ABSTRACT

Tensar uniaxial geogrids were subjected to load-controlled monotonic and cyclic pullout testing to determine the relative coefficients of interaction. The variables investigated were geogrid series (UX1500SB, UX1400HS, and UX1600HS), soil type (poorly-graded medium fine sand and poorly-graded silty fine sand-sized glass beads) and normal stress (5, 10, and 20 kPa). The geogrid specimens, roughly 0.5 m wide by 1.5 m long, were strain-gauged to allow description of pullout behavior at small displacements. Results suggest that irrespective of geogrid series, soil type, or normal stress the soil-geogrid interaction is approximately equal under monotonic and cyclic loading. Additionally, at the frequency of cycles used, the geogrids did not pull out catastrophically but instead displaced incrementally in a controlled manner when the cyclic load exceeded the peak load sustained by the geogrid under monotonic loading.

TABLE OF CONTENTS

LIST OF TABLES

LIST OF FIGURES

ACKNOWLEDGEMENTS

CHAPTER 1

INTRODUCTION

1.1   Introduction

Geosynthetics have now been available for wide-spread commercial use for more than thirty years, during which time emphases have been placed variously on product development, market development, engineer/designer education, and regulatory oversight. It could be said fairly that the first three emphases within the industry are moving into "mature" phases where significant effort has been expended, but is still ongoing. However, regulatory oversight by its very nature is reactive and conservative and does not necessarily follow any technical innovation or developments in the field in any kind of timely manner.

Geogrids are one type of geosynthetic that are routinely used in soil reinforcement applications such as slopes, retaining walls, and roadways. In many situations, their use offers a cost advantage over conventional methods of construction, and offers greater aesthetic flexibility. The nature of geogrids and their use in practice are given in Chapter 2.

Of particular interest in this study is the performance of geosynthetic-reinforced soil (GRS) slopes and walls, constructed with geogrids as the reinforcing element, under incremental dynamic loads (caused by earthquakes, blasts, or traffic). Observations of existing GRS structures and specialist model tests suggest excellent performance. However, regulations currently in place do not reflect the limited field data gathered thus far.

To this end, the following aims to address the soil-geogrid interaction under dynamic loading and discuss the likely implications on design practice.

1.2   Current Design Practice

Design practice for GRS structures under seismic loads for public projects is generally specified as being the American Association of State Highway Transportation Officials' (AASHTO) LRFD Bridge Design Specifications (1998). Contained therein is a step-by-step procedure for the analysis of internal and external stabilities of a given GRS structure. External

stability analysis considers bearing capacity of the foundation soil and overturning and sliding of the GRS structure. Internal stability analysis considers pullout capacity of the individual geosynthetic inclusions, geosynthetic rupture, and connection details for facing (if present).

To design the GRS structure to withstand seismic activity, the AASHTO specifications requires three additional loads to be applied to the structure over the static case: the first is an inertial force caused by the mass movement of the soil in the reinforced zone; the second is an incremental dynamic load applied to the back of the reinforced soil (discounted 50 percent due to the unlikelihood of both forces peaking simultaneously); and the third is an incremental inertial load applied to the geosynthetic from an assumed active zone within the reinforced soil. The first two loads are used for external stability analyses, and the third is used for internal stability (geosynthetic pullout). To compute the internal stability, the soil/geosynthetic interaction is taken to be 80 percent of the static value.

1.3   Resesarch Objectives

The objectives of this study are:

- to explore the strain behavior of geogrids undergoing cyclic pullout at a relatively high cyclic frequency, with reference to a previous study (Raju, 1995);
- to identify the level of soil/geogrid interaction under dynamic loading in various conditions of normal stress, soil type, and geogrid type, and contrast that to the level of interaction under static loading;
- to compare two methods of calculating soil/geosynthetic interaction; and
- to explore the potential ramifications findings of this study may have on existing design practice and regulation.

These objectives were met in a program of testing using a large pullout testing apparatus at the University of British Columbia.

1.4   Thesis Organization

Chapter 2 reviews the performance of GRS structures that have been subjected to seismic events and lays a groundwork of theory that the testing program is based on. Chapters 3 and 4

describe the pullout testing apparatus and materials used in the tests, respectively. In Chapter 5 the testing preparation, procedures, and post-test procedures are given. Chapter 6 presents the results and observations regarding the behavior of the geogrids in the pullout tests. Analyses of the test results to provide levels of interaction and describe the strain behavior of embedded geogrids are given in Chapter 7. Chapter 8 presents conclusions drawn from the testing program results and analyses, and suggests possibilities for future research.

CHAPTER 2

LITERATURE REVIEW

2.1   Introduction

This chapter presents a summary of literature that is relevant to the objectives of this study; particular emphases are placed on case studies of GRS structures that have been subjected to seismic events after construction, and prior research that provides the basis for this study. A brief introduction to geogrids, followed by the features and design of GRS structures, is also given.

2.2   Geogrids

According to the International Geosynthetics Society (IGS), the definition of a "geogrid" is:

> A planar, polymeric structure consisting of a regular open network of integrally connected tensile elements, which may be linked by extrusion, bonding or interlacing, whose openings are larger than the constituents, used in contact with soil/rock and/or any other geotechnical material in civil engineering applications. (IGS, 2000)

The Tensar geogrid studied in this program of testing is an extruded polyethylene geogrid that has a series of long, slender ribs intersected by thicker transverse bars at regular spacings. Further details of the geogrids used in this study are given in Section 4.3, and plan and profile views of a typical Tensar geogrid are given in Figure 4.1.

In practice, geogrids are used to reinforce soil or rock masses by taking up tensile stresses generated within these masses due to imposed and self-weight loads. The geogrids are placed with the ribs aligned in the direction of primary stress and the transverse bars perpendicular to the direction of primary stress. Shear stress is transferred to the geogrids through frictional contact with the soil/rock mass on the planar surface area of the ribs and transverse bars and through bearing contact with the mass on the front edge of the transverse bars, perpendicular to the plane of the geogrids. Load tranfer occurs by "mobilization" (displacement) of the geogrid relative to the mass.

2.3   Geosynthetic-Reinforced Soil (GRS) Structures—Features and Design

The concept of reinforcing soil is analogous to reinforced concrete (although the practice of reinforcing soil is much older)—strengthening and stabilizing a mass from within is more intuitive than restraining from without, as well as being more cost-effective.

Typical GRS structures are retaining walls, slopes, abutments, and foundations (for roads or buildings). While the external dimensions and shapes of these applications may differ significantly from each other, they all contain the same two components: soil, reinforced with a geosynthetic that is aligned in such a way as to take up the resultant tensile forces from loads externally imposed on the soil mass (as discussed above). GRS walls, abutments, and slopes typically have an additional facing component that provides additional stability to the system, · prevents soil loss, and adds to the aesthetic value of the structures.

Design of GRS structures varies depending on the structure and application, but generally follows an approach given below:

1. the geometric parameters of the project are defined (e.g., the height of the wall);
2. the soil material properties are defined (usually it is desirable to utilize on-site materials);
3. geosynthetic inclusions are sized and quantified based on steps 1 and 2;
4. internal stability of the system is considered, which is focused on providing a geosynthetic that is capable of withstanding the resultant tensile forces and ensuring the inclusions will not displace exessively as loads are imposed;
5. external stability of the project is investigated, including sliding and overturning (if a wall or abutment), bearing capacity of the foundation soils, and overall site stability if required; and
6. other details are designed, primarily focused on providing positive drainage from the site.

Design of GRS structures to withstand seismic loads is incorporated into Steps 4 and 5 above, with the addition of pseudo-static loads as described in the previous chapter.

More specific design information and guidance can be found in publications such as AASHTO's LRFD Bridge Design Specifications (1998) and NCMA's Design Manual for Segmental Retaining Walls (Simac et al., 1997) with the NCMA Seismic Design Manual (Bathurst, 1998).

2.4   Case Studies

Limited information exists from GRS structures that have undergone seismic loads; the short case studies given below are derived primarily from two sources that have documented two major earthquakes.

On January 17, 1994, a Magnitude 6.7 earthquake hit the Los Angeles, California area (Sandri, 1997). The event was particularly significant in that vertical accelerations were far higher than anticipated, based on previous events. This is a special concern for GRS structures, which derive their strength by the vertical confining stress from the soil self-weight.

Sandri (1997) documented the performance of 11 GRS structures in his paper, all within 110 km of the epicenter. According to site visits after the earthquake and a review of the design and construction records of each structure, it was concluded the performance of all structures was excellent—meaning no failures and only slight displacement and/or cracking of the wall/slope faces.

Two structures were singled out for particular attention. The first is the Valencia Water Treatment Plant wall, located 18 km from the epicenter. The wall is 6.4 m high and approximately 8 km long and was constructed one year prior to the earthquake using Miragrid geogrid and Keystone Standard blocks for the wall facing. It was subjected to an estimated peak horizontal acceleration of 0.5g, substantially higher than its 0.3g design. Inspection after the earthquake showed minor surface tension cracking in the soils at the back of the reinforced soil mass. Fill placed at the toe of the wall was noted to have substantial movement, from consolidation and surface fissures (the fill was supposed to be saturated at the time of the earthquake). No relative movement between the facing and geogrid was noticed. As a point of reference, two cantilevered walls located within 100 m of the Valencia wall "experienced significant cracking causing them to be taken out of service for repairs." The second is the Gould Tank walls, located 35 km from the earthquake epicenter, constructed to support an access road

adjacent to water storage tanks. The wall is 5.8 m high and likewise constructed one year prior to the earthquake event. It was constructed with Miragrid geogrid and Keystone Standard blocks. It was subjected to an estimated peak horizontal acceleration of 0.3g+. Seismic design was not specified for the wall, but overall slope stability analyses were performed using a peak horizontal acceleration of 0.15g. Connection details (geogrid to facing units) were not considered in the design. Prior to the earthquake, construction traffic over-surcharged the top of the wall, causing it to bow outward and create a reverse batter. Post-earthquake inspections showed surface tension cracks near the back of the soil mass and no signs of absolute or relative movement of the wall face.

One year later, on January 17, 1995, a Magnitude 7.2 earthquake hit the Hyogo Prefecture, encompassing Kobe City and its suburbs. Tatsuoka et al. (1996) examined several types of retaining walls after the earthquake, all associated with a major railway system running through the extensively damaged areas of Kobe. These wall types include masonry, leaning unreinforced concrete, gravity, cantilever, and GRS retaining walls. Four GRS walls were constructed between 1990 and 1994 to support either road or railway traffic, to heights of 3 to 8 m. Damage to the GRS structures included small cracks in the facing (usually a concrete monolith poured after full-height completion of the reinforced zone), minor tilting of the walls, and movement of the reinforced soil mass relative to other adjacent structures that had not been tied into the GRS walls. The Tanata wall was singled out for attention. This wall is located on one side of a concrete box culvert on the railway alignment; on the other side of this box culvert is a reinforced concrete retaining wall cast on bored piles (the GRS wall was placed directly on the foundation soils). The performance of both walls was similar during the earthquake—both walls displaced 150 mm relative to the box culvert, even though the GRS wall was designed for a peak horizontal acceleration of 0.2g, much smaller than the estimated peak horizontal acceleration at the site.

It was concluded that the Kobe GRS walls performed "very well" compared to the conventional wall structures; many of the conventional walls failed due to a combination of structural failure and foundation failure, and were subsequently replaced with GRS walls.

From these observations, it can be inferred that there exists a degree of conservatism in the design of GRS structures, particularly for seismic events. Recent research has focused on

identifying and quantifying the poorly understood mechanisms of dynamic pullout behavior in an effort to reduce the design conservatism.

2.5   Previous Research in Static/Dynamic Soil-Geogrid Interaction

Laboratory research into the performance of geogrids used in GRS structures subject to cyclic and/or dynamic loading is limited. Below is a description of relevant research to date.

Sitar and Nova-Roessig (1999) reviewed a number of laboratory and field studies on the seismic behavior of GRS structures. Eighteen tests were reviewed, which comprised tilt-up, shake table, centrifuge, and large-scale (half to full) tests on reinforced walls and slopes. Findings typically showed that longer reinforcement with closer spacing and denser backfill compaction improved the seismic stability of the structures. Most notably, however, was the clear indication that the structures endured large displacements but rarely underwent catastrophic failure unless they were clearly underdesigned by even static design standards. Within the review was a caution that similitude laws were not closely adhered to in some of the studies, casting concern on the applicability of the results to full-scale reinforced structures.

Bathurst and Alfaro (1997) conducted a similar review of laboratory testing programs related to the seismic behavior of GRS structures, but their review encompassed elemental testing programs—those that examined soil/geosynthetic interaction and geosynthetic/facing connections—in addition to shake table and centrifuge tests on model-scale GRS structures. Three studies reviewed specifically addressed pullout tests on geogrids under dynamic loading: Yasuda et al. (1992), Raju (1995), and Min et al. (1995). Yasuda et al. reported dynamic pullout loads in excess of the companion static pullout loads; Raju reported dynamic pullout loads up to 20 percent higher than companion static pullout loads depending on geogrid manufacture; and Min et al. reported a reduced dynamic pullout load as compared the static value, on the order of 20 percent. In their conclusions, Bathurst and Alfaro suggest that the design methodologies used in the United States for seismic design of GRS structures (AASHTO/FHWA) have been based largely on numerical modelling of structures reinforced with inextensible steel strips, and that further testing should be conducted with extensible inclusions to verify (or correct) the current design methodologies. Also indicated was a need for further testing to determine the proper distribution of seismic forces transferred to the extensible reinforcement in GRS structures.

Details of the difficulties encountered in pullout testing and the accompanying interpretations were described in a paper by Wilson-Fahmy et al. (1994). The objective of their research was to quantify and describe the mechanics of anchorage development (development of pullout resistance). The testing program allowed back-calculation of the contribution to pullout resistance the geogrids' transverse bars provide in bearing.

Cai and Bathurst (1995) set out to compare results of the dynamic response of a GRS wall using the conventional seismic pseudo-static limit-equilibrium (AASHTO/FHWA) approach to results of a finite-element analysis (FEA). The comparisons led the authors to conclude that forces calculated in the reinforcing elements were larger using the AASHTO/FHWA method than given by the FEA. Additionally, the static reinforcement loads were predicted to be higher using the AASHTO/FHWA method than given by the FEA. As a sideline, their FEA indicated that horizontal accelerations varied little along the height of the wall, consistent with the standard practice of applying a single acceleration factor to the analysis prescribed by AASHTO/FHWA. This finding is contrary to the results of several laboratory testing programs reviewed by Sitar and Nova-Roessig (1999), which found acceleration magnification occurring with height in the wall.

In 1998, the National Concrete Masonry Association published *Segmental Retaining Walls Seismic Design Manual*, a companion manual to their *Design Manual for Segmental Retaining Walls* (Second Edition, 1997). Although the general design methodology parallels that of AASHTO (1998), the NCMA publication addresses stability issues specific to GRS walls with dry-stacked masonry block facing that are absent in the AASHTO document. The manual includes a commentary expressing a concern for applying a 20 percent discount to the coefficient of interaction for seismic design, because the AASHTO/FHWA discount is based on cyclic pullout tests on steel strip (inextensible) reinforcements.

The research that provides the direct impetus for this study originates in Muthu Raju's 1995 thesis, the relevant results of which are summarized in a paper by Raju and Fannin (1997). The research performed examines three geogrid specimens in displacement- (static) and load-controlled (cyclic) pullout at varying frequencies. Numerous conclusions were drawn from this work, but the relevant ones are given below:

1. loading frequency (in load-controlled monotonic tests) appeared to influence the incremental displacement incurred with each cycle, but not the absolute value of pullout resistance;

2. "stable" versus "unstable" behavior in pullout under cyclic loading was denoted by the tendency toward increasing incremental displacements with each load cycle at a given load ratio (LR), defined as the ratio of demand load in cyclic pullout to the maximum pullout load measured in the corresponding displacement-controlled test; and

3. the ratio of interaction factors generated under cyclic loading to those generated under displacement-controlled loading were equal to or greater than 0.8, a value specified in prominent regulations governing the design of GRS walls for discounting the seismic value of interaction from the static value.

In summary, it appears that GRS structures that have been subjected to seismic loads have performed admirably. Laboratory testing and finite element analyses to date generally indicate a degree of conservatism that exists in the prevalent GRS seismic design methodology used in North America, and conclude by suggesting futher work be completed to justify or correct specific requirements of the design regulations.

Pullout testing on geogrids suggest in some cases better performance of soil/geogrid interaction under dynamic loading compared with static loading, while in other cases better performance was noted under static loading. The variations in performance appear to stem from geogrid geometries and geogrid type.

The intent of this program of testing is to systematically address these variations of soil/geogrid interaction by subjecting three different geogrids of one manufacturer to static and dynamic loads under varying conditions of normal stress and soil type. The results of these tests are then examined in light of current design practice.

CHAPTER 3

TESTING EQUIPMENT

3.1   Introduction

To achieve the objectives stated in Chapter 1, a large pullout apparatus and its associated equipment were used. The apparatus was originally designed and fabricated for displacement-controlled pullout tests (Raju, 1991) and substantially modified to enable load-controlled tests (Raju, 1995). The primary use of the pullout apparatus is to allow a geosynthetic specimen to be pulled out of a soil material with known boundary conditions and provide a means to quantify soil/geosynthetic interaction.

The apparatus and associated equipment provide a means to contain the specimen and soil material, to pull the geosynthetic out of the soil, and to measure the applied loads and resulting displacements, strains, and changes in soil pressure at the pullout boundary. This chapter describes the components of the apparatus and associated equipment.

3.2   The Pullout Apparatus

The pullout apparatus consists of several components: the pullout box, a reaction frame, a clamp assembly for gripping the geosynthetic specimen, a surcharge application system, and an electrically-controlled hydraulic loading system. An ancillary item is the pluviation chamber, which is used to place the sand. Each of these components is described separately below.

3.2.1   Pullout Box

The pullout box itself contains the soil material and test specimen, and is shown in Figure 3.1. Its dimensions are 1300 mm long, 640 mm wide, and 600 mm deep. It is constructed within a heavy steel reaction frame, and is lined with 3 mm glass laminated to 2.5 mm plexiglas along the sides and 13 mm aluminum plates along the front, back, and bottom. The front boundary contains a 25 mm slot at midheight of the box running the width of the boundary, through which the geosynthetic specimen is pulled. To prevent soil loss during a test, the slot was lined with

foam rubberstripping, leaving a 1 mm slit. A 16 mm hole was drilled in the center of the back boundary at mid-height to allow instrumentation wires to exit the box.

In the absence of any standards for construction of pullout devices at the time of design and fabrication, the dimensions of the box were selected to satisfy three requirements: to provide a scale representative of the geosynthetic characteristics; to allow a specimen length-to-width ratio of two; and to minimize boundary effects. For a complete discussion of the design process and rationale, see Raju (1995, 1991).

3.2.2   Reaction Frame

The reaction frame houses the box and a mechanical connection for the hydraulic actuator which applies the pullout load. The frame is constructed of mild steel S-, C-, hollow square, hollow rectangular, and hollow round sections bolted and welded. Figure 3.1 shows the arrangement and sizes of the major components.

A rectangular mild steel plate (760x1485x25 mm) fits over the box and is bolted to the reaction frame through a series of holes at both ends of the plate and frame, and by two cross-beams that bolt to threaded bars extending from the base of the reaction frame on either side of the box. This plate provides a reaction for the surcharge pressure applied by a water-filled PVC bag (see next section).

3.2.3   Surcharge Application System

When tests require a higher normal stress than the weight of the 0.3 m of overburden soil (a nominal 5 kPa), a surcharge pressure is applied through the use of a pressurized PVC water bag placed directly on top of the soil material, as shown in Figure 3.2. The PVC bags, specially made for this purpose, have two hoses extending from the tops of the bags, one end fitting to the water reservior and the other to the water pressure transducer. The bag is filled with water from the laboratory supply through the reservior. The reservior is vented to maintain atmospheric pressure at all times, and pressure within the system is set by the height of the water level in the reservior above the water bag.

3.2.4 Electro-Hydraulic System

An electrically-operated hydraulic system provides the mechanical force required for pulling the geosynthetic specimen out of the pullout box. The system consists of several components: the hydraulic pump, a servovalve, an actuator, and a controller. The pump, servovalve, and actuator are described here; the controller is described in Section 3.3.3. A schematic of the system is shown in Figure 3.3.

The hydraulic pump is a MTS Systems Corp. model 502.03, supplying 3 GPM of hydraulic oil to the actuator at 3000 psi. Operation of the pump is controlled remotely by an MTS Systems Corp. 436 Control Unit.

The servovalve, a Moog Controls 760, acts as the electrical/hydraulic interface and interprets the electrical demand signals from the computer/signal conditioner to mechanical signals and is mounted to the side of the actuator. The servovalve, rated for 3000 psi, is fed signals from the MTS Systems Corp. 406 Controller.

The hydraulic actuator is double acting (applies force in both directions along its axis of operation), and is mounted directly to the reaction frame. It has a 63.5 mm bore and 152.4 mm stroke length and an operating pressure of 3000 psi. It has an internal LVDT that measures displacement for use in feedback control (see Section 3.3.4.1). The actuator is positioned so that its operating axis intersects the center of the slot in the box front boundary.

3.2.5 Clamp Assembly

A clamp assembly attaches to the actuator piston end, after the load cell. It comprises four distinct parts: the upper and lower jaws, a central insert, and a pin (see Figure 3.4).

The lower jaw fits onto the end of the actuator piston, which is fitted with an eye bolt. Once slid onto the eye bolt, the jaw is "locked" to the bolt by a pin that is dropped into the top of the clamp. This swivel joint allows limited full articulation, preventing any transfer of moment to the specimen. The geosynthetic specimen rests on the lower bench of the jaw, which has a series of serrations to positively grip the specimen.

The beveled central insert, placed on top of the geosynthetic specimen, has serrations on its lower edge to grip the upper portion of the geosynthetic. It also has flanges protruding from its ends that provide an area on which the clamp LVDTs can maintain solid contact with the clamp. The insert has a series of tapped holes into which steel lugs can be screwed for a mechanical connection with the specimen. These lugs were only used while testing the aluminum steel plate, and were removed when testing with the geosynthetic specimens.

The upper jaw is placed on top of both the lower jaw and the central insert, and is bolted to the lower jaw through a series of four boltholes tapped into the lower jaw. The upper jaw contains a semi-cylindrical cam running the length of its underside which applies pressure to the central insert to lock it against the lower jaw and press the serrations into the geosynthetic.

All clamp components are aluminum except for the pin, semi-cylindrical cam, and bearing pad on the central insert, which are mild steel.

The weight of the clamp assembly is borne by a wooden support bench. To minimize frictional resistance, a steel plate with stainless steel bearings is placed between an arborite sheet glued to the underside of the clamp lower jaw and an arborite sheet glued to the support bench.

3.2.6 Pluviation Chamber

Sand is placed into the box in a dense state by way of air pluviation. An air pluviation chamber that rests directly on the pullout box was designed and fabricated for this purpose. The chamber is shown in Figure 3.5. Its structure is made of aluminum angles and strips; the sides are 3 mm plexiglas to contain the sand during pluviation. The front plexiglas panel is hinged so that it may be opened after pluvation for access to the pullout box and for cleaning after each pluvation event. Above the chamber and separated by a set of trap doors is a hopper that holds the sand prior to pluviation. Once pluviation is initiated by the pneumatic release of the trap doors, the sand falls through twin perforated steel plates that have been offset to produce specific aperature sizes. The design rationale is disussed in Raju (1991).

3.3 Signal Generation and Data Acquisition

Demand signal generation and processing and data acquisition involve a number of components and steps. The components involved in these operations are described below, while a flow chart showing them is given in Figure 3.3.

Mobilization of pullout resistance is governed by a feedback control system. A demand signal (either displacement or load) is generated by computer, fed through the signal conditioner to the MTS controller, and finally to the servovalve, which results in a displacement. A "feedback" signal is sent either by the actuator LVDT or load cell to the controller and compared to the demand signal. A difference (error) signals the controller to issue a correction to the servovalve. The feedback process is repeated until there is no error.

Data acquisition is done by the computer which scans all incoming signals from instrumentation on a predetermined basis. Instrumentation is powered by a direct current (DC) voltage ("excitation voltage"); any change in load, pressure, or displacement induces a change in this voltage, which is recorded by the computer.

There are four distinct components of these operations: the computer, signal processor, controller, and instrumentation, which are described separately below.

3.3.1 Computer

A 386SX computer is used to generate demand signals and provide data acquisition for the pullout apparatus. The software written to generate demand signals and capture data used Microsoft MS-DOS QBasic, and represents a major upgrade of the code used for the previous testing programs. The program takes advantage of a MetraByte Corporation DAS-16 data acquisition board for digital-to-analog (D/A) and analog-to-digital (A/D) conversions and instrument channel scanning. The board has the capability of scanning up to 16 input (data acquisition) A/D channels and allows D/A output (demand) on two channels. The board is physically mounted in an expansion slot in the computer.

3.3.2 Signal Conditioner

All input and output signals are passed through the signal conditioner that provides several levels of functionality. First, the signal conditioner has an on-board power supply that supplies up to four differing DC voltages for instrument excitation. Second, the processor portion steps input voltages up by variable amounts, and allows variable offsetting of the voltages. Third, the processor filters the voltages by attenuating stray signals ("noise"). The signal conditioner was designed and built at UBC.

3.3.3 MTS Electro-Hydraulic System Controller

The controller receives the demand signal from the computer via the signal conditioner and relays this signal to the servovalve, which triggers an actuator displacement. The controller then monitors returning signals from the actuator LVDT (for displacement control) or load cell (for load control) and compares these signals to the demand signal. Any discrepancy between them is termed "error" and causes the controller to issue a further signal in an attempt to reduce the error to null. The signal from the load cell is passed first through the controller, then into the signal conditioner where it is acquired by the data acquisition system.

3.3.4 Instrumentation

In all, sixteen instruments were used to gather information about the performance of the geosynthetic specimen and soil material before and during testing. These instruments include LVDTs, transducers, and strain gauges. Each type and its use is described below.

3.3.4.1 Displacement

Displacement of the test specimen was measured at the clamped and embedded ends of the specimen by three linear variable differential transformers (LVDTs): one on each end of the clamp assembly and one at the back of the pullout box. The reason for having two LVDTs mounted against the clamp assembly was to yield an average displacement for the exposed end of the geosynthetic.

The front LVDTs are SE Labs SE 373/100 and 374/100 series LVDTs with 240 mm strokes. These are mounted on a weighted stand that remained separate from the pullout apparatus reaction frame. The armature heads (plexiglass balls) rested against the flanges protruding from the clamp assembly central insert, shown in Figures 3.1 and 3.4. The armatures are internally and externally spring-loaded to allow data capture in both directions. The rear tell-tale LVDT is a Trans-Tek 245-0000 series, with a usable stroke of 140 mm. It is mounted on a bracket extending from the back boundary so that the operating axis of the LVDT is in line with the center of the access hole in the back boundary. A small hole was drilled in the extension rod of the armature through which the tell-tale wire was attached; a weight was attached to the back end of the armature and strung over a pulley to ensure the tell-tale wire remained taut during testing.

An additional LVDT (Tempsonics II) is mounted internally on the actuator piston. This LVDT was used to provide error correction to the controller when in displacement-control mode.

3.3.4.2 Load

The pullout load was measured by an Interface, Inc., model 1210AF 5000 lb. capacity load cell. It was placed in-line between the hydraulic actuator and the clamp assembly.

3.3.4.3 Surcharge Pressure

The surcharge pressure was measured by a MagneTek SP100G 0 – 15 psig water pressure transducer. It was mounted to the laboratory wall at mid-height of the PVC water bag. Pressure was monitored by this gauge by the exit tube of the water bag.

3.3.4.4 Boundary Stress

Six Total Pressure Transducers (TPTs) were placed in the center of the front boundary, three above and three below the central slot, flush with the inside face. These transducers, Data Instruments Inc. AB-HP 0-50 and 0-100 psig, were used to monitor the horizontal soil pressure during soil material placement, surcharge application, and testing. Although monitored and recorded the data are not presented or discussed in this thesis.

3.3.4.5 Geosynthetic Strain

Geosynthetic strain was monitored by strain gauges affixed directly to the geosynthetic. Inside the pullout box, the gauges were affixed approximately on the center of the central rib, while the placement of the in-air strain gauge varied in position on the central rib depending on the series of geogrid used. This variation resulted from the constraints imposed by the geometry of the pullout box and the length of the ribs between transverse bars on the geogrid (see Section 4.3), and was necessary to ensure a transverse bar was not pulled through the front slot during testing. The strain gauges were manufactured by the Micro Measurements Division (Measurements Group, Inc.), type EP-08-250BF-350 option E. These were selected because of their high elongation capability (10 to 15 percent) and due to their factory encapsulation. A strain-gauged sample is shown in Figure 3.6 and a schematic of strain gauge locations is given in Figure 3.7.
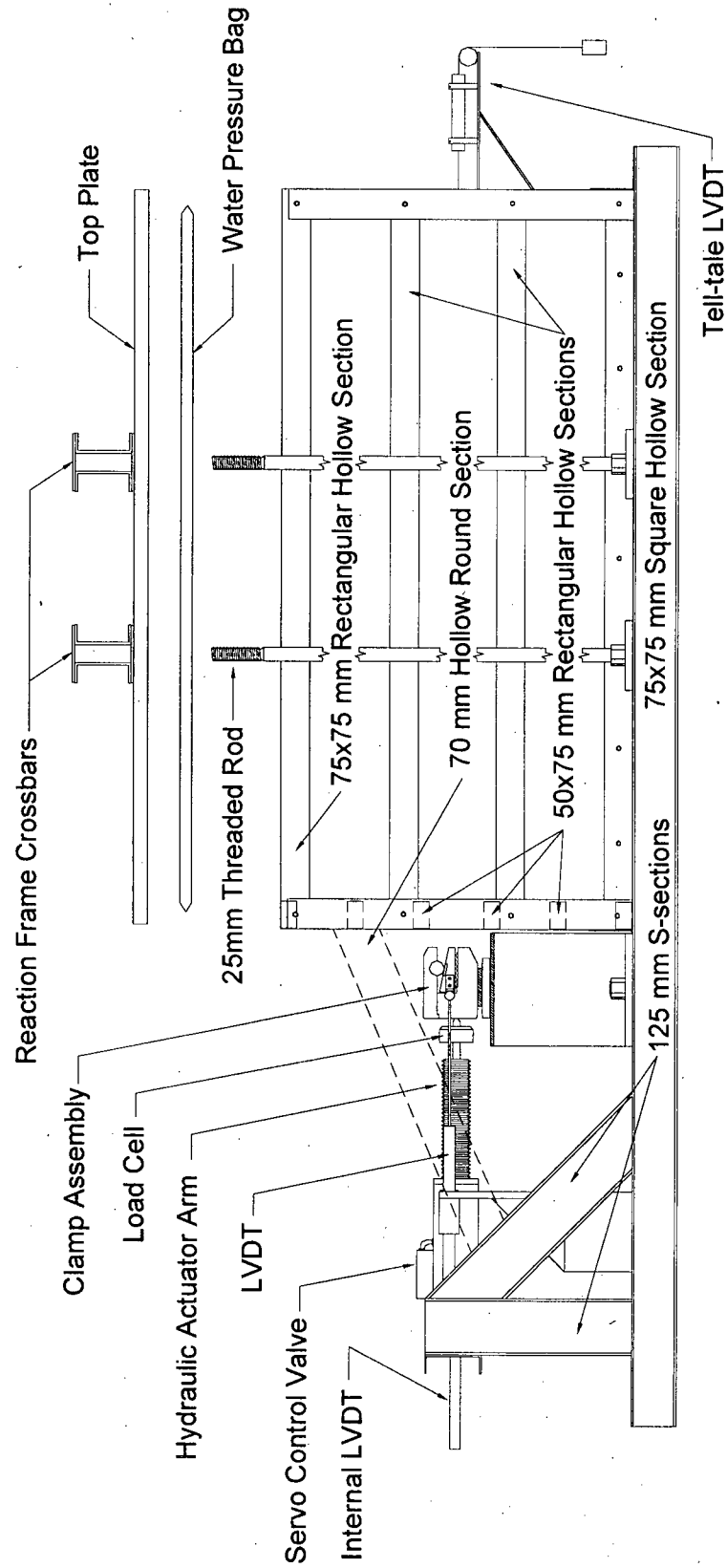
Figure 3.1: The components and structure of the pullout apparatus

Labels in figure: Top Plate, Water Pressure Bag, Reaction Frame Crossbars, Clamp Assembly, Load Cell, Hydraulic Actuator Arm, LVDT, Servo Control Valve, Internal LVDT, 25mm Threaded Rod, 75x75 mm Rectangular Hollow Section, 70 mm Hollow Round Section, 50x75 mm Rectangular Hollow Sections, 75x75 mm Square Hollow Section, 125 mm S-sections, Tell-tale LVDT

Open to atmosphere

Constant water head

To house water supply

Water pressure transducer

PVC Water Bag

Profile View of Pullout Apparatus

760

1485
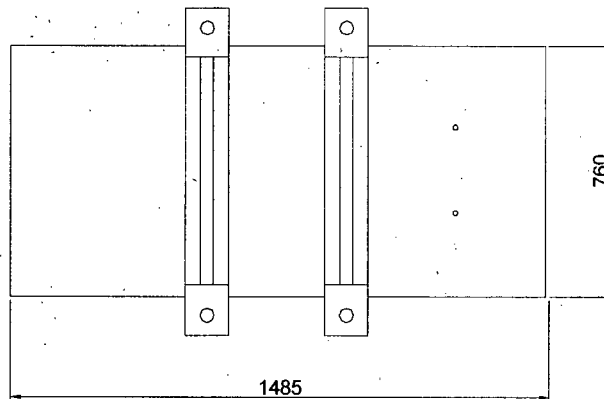
Plan View of Top Plate and Reaction Beams

**Figure 3.2: A schematic of the surcharge pressure application system with a plan
view of the reaction system. All dimensions are in mm.**
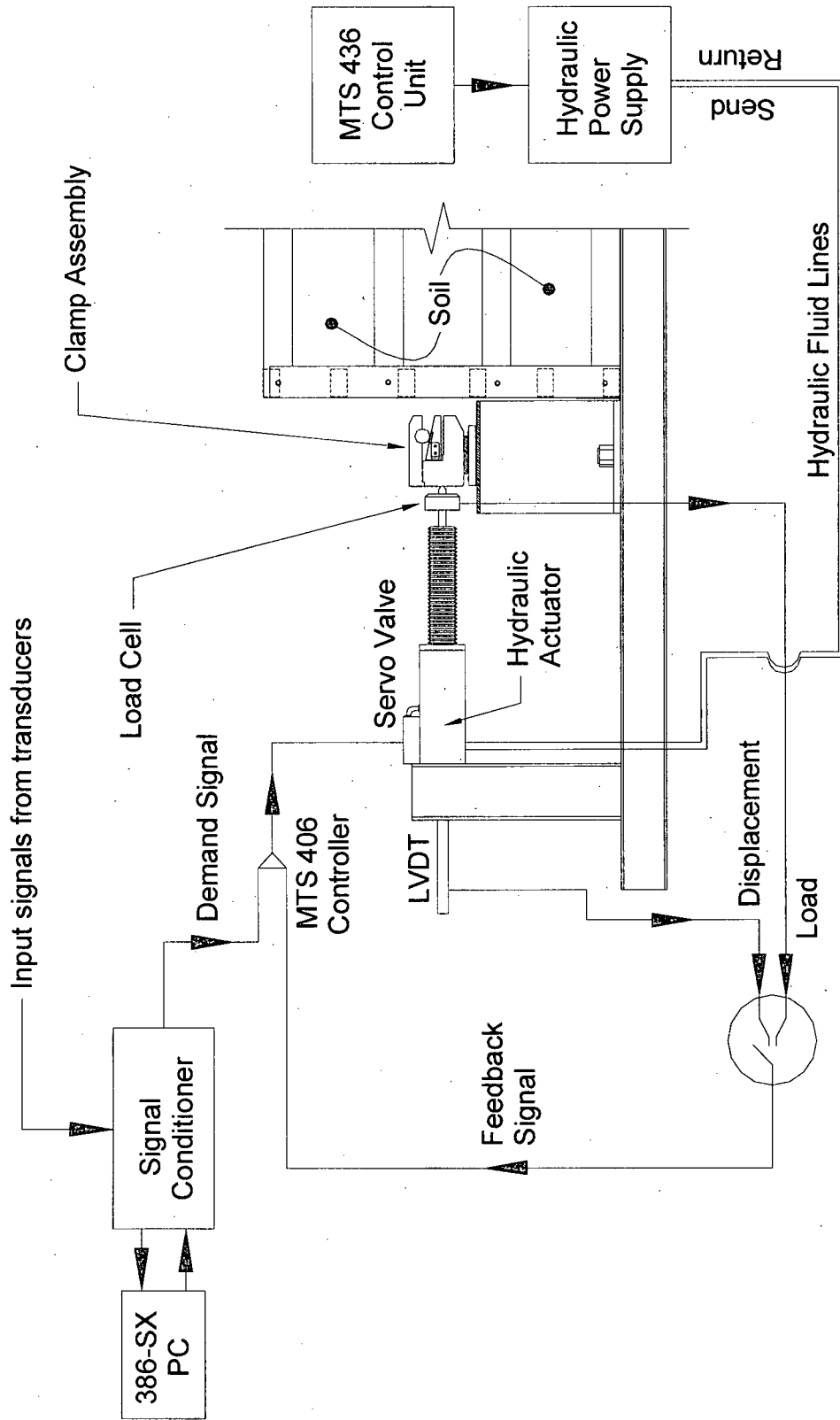
Figure 3.3: The electro-hydraulic system with a flow chart showing control of the system

Profile View

125

95 (when assembled)

Upper Jaw

Locking Pin

Eye Bolt

Lug

Central Insert

Lower Jaw

Arborite Pad

Plan View

645

125
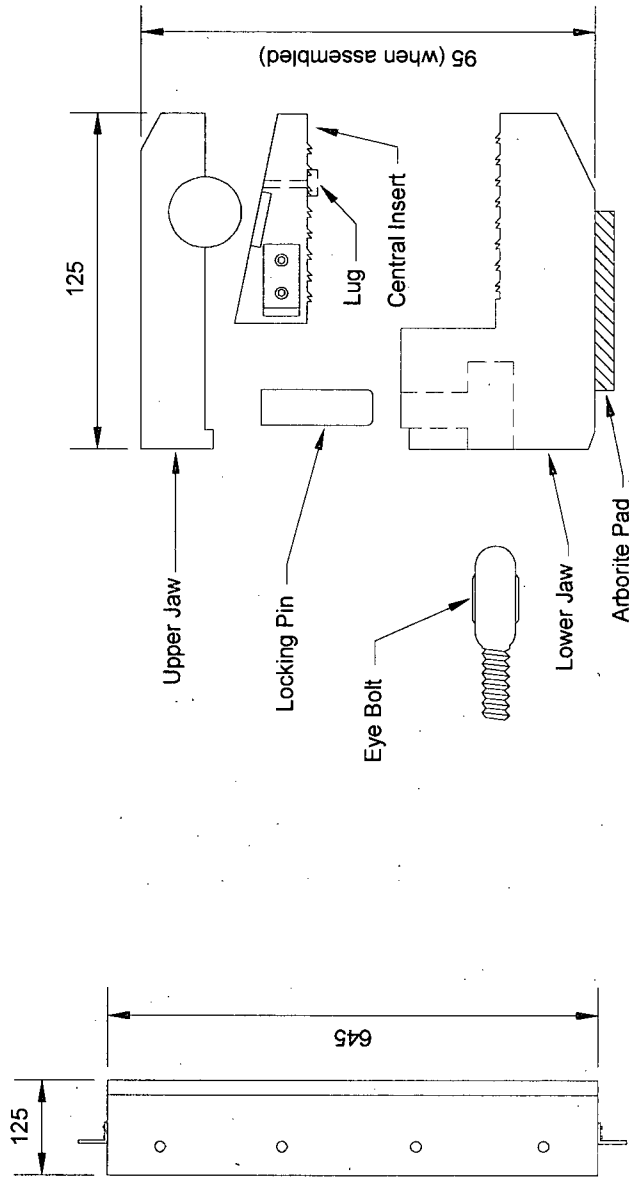
Figure 3.4: Plan and profile views of the clamp assembly. The lug on the central insert was only used for the aluminum plate tests. All dimensions are in mm.
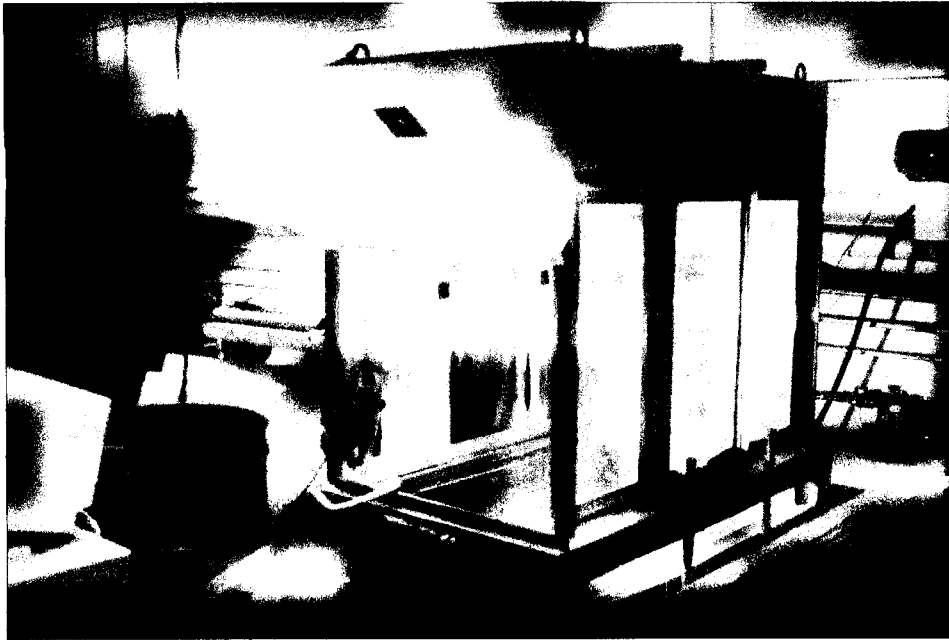
Figure 3.5: The pluviation chamber mounted on top of the pullout box
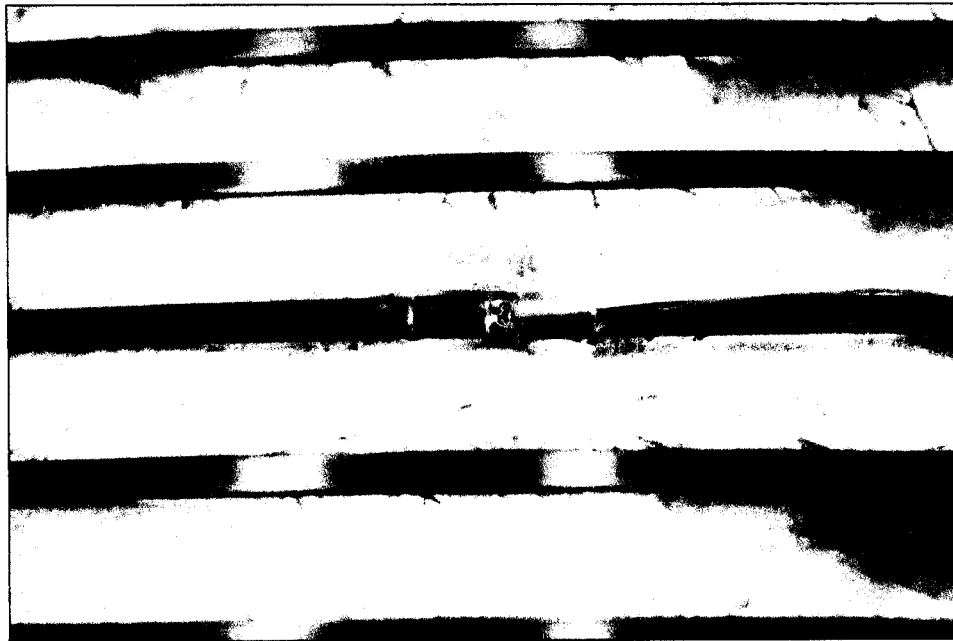
Figure 3.6: A strain gauge mounted to the rib center. Three wires were taped to the rib then soldered to the gauge terminals to prevent any transfer of load to the gauge site.
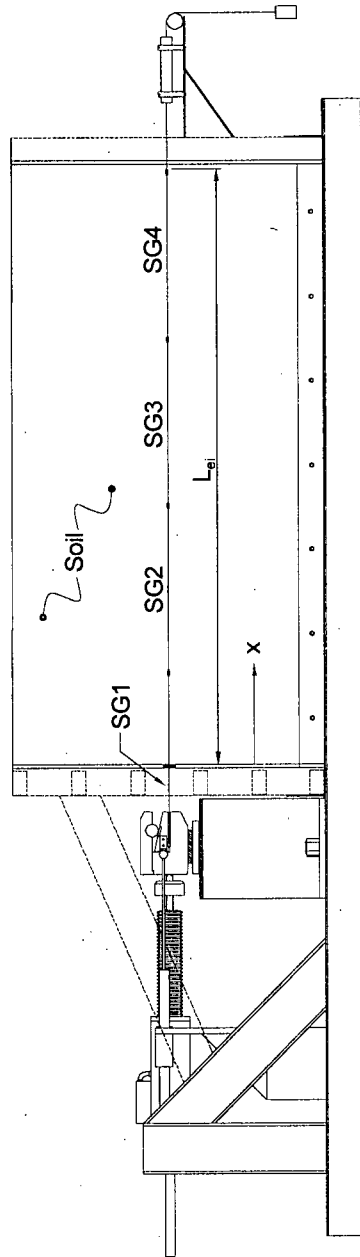
Figure 3.7: A schematic of the strain gauge locations along the length of the 1400 and 1600 series geogrids; the 1500 series geogrids contained two more transverse bearing bars and one more strain gauge.

CHAPTER 4

MATERIALS AND PROPERTIES

4.1   Introduction

The objective of this study is to compare the pullout behavior of three Tensar geogrid series embedded in dissimilar soils. As such, two soils were selected for use in testing. The geogrids, soil materials, and their properties are described below.

Prior to starting the testing program, preliminary pullout tests using a roughened aluminum sheet were conducted to benchmark the results to a previous testing program (Raju, 1995) using the same apparatus described in Chapter 3.

4.2   Fully Roughened Aluminum Plate

Prior to commencing the main body of the testing program, a series of preliminary pullout tests were conducted using a fully roughened aluminum plate as the specimen. The 3 mm thick aluminum plate, 500 x 1127 mm, was roughened by gluing sand particles to both sides of the plate. The purpose of the preliminary tests was to commission the testing apparatus by matching results of these tests to a previous study that used the pullout apparatus (Raju, 1995). Raju's study incorporated the use of the aluminum plate to compare extensible to inextensible pullout behavior; it was roughened to ensure that the friction angle between the plate and sand (δ) was equal to the internal friction angle of the sand (ϕ).

4.3   Tensar Geogrids

Three uniaxial geogrids were selected for use in this study. The UX1400HS and UX1600HS geogrids were selected as the most commonly used products in larger walls and slopes. The UX1500SB series was included to allow a comparison of results from this testing program with those of Raju (1995).

A Tensar uniaxial (UX-) geogrid is formed from a sheet of high-density polyethylene (HDPE) that is punched with rectangular holes then drawn under heat to align the polymer fibers and prestress the grids. The drawing process results in a pattern of stiff, slender ribs crossed by

thicker transverse bars at regular spacings. Figure 4.1 shows the plan and section views of these grids. Of significant note regarding the geometry of Tensar geogrids is the substantial vertical profile of the bars compared to the ribs. Strength and stiffness properties for each grid type are reported in Table 4.1, below.

Table 4.1: Tensar geogrid strength properties

Grid Type	Strength (2%/5% Strain)[1] kN/m	True Initial Modulus[2] (kN/m)
UX1400HS	16.8/31.5	1831
UX1500SB	28.5/50.5	2389
UX1600HS	38.7/75.0	3634

(1) True strength measured via GRI-GG1 ("Geogrid Rib Tensile Strength" standard) at indicated strain
(2) Measured via GRI-GG1 not employing an artificial "offset tangent" or "secant" basis of measurement

4.4 Soil Materials

Two soil materials were used in this testing program. A poorly-graded medium-grained sand with a relatively high friction angle was used to generate upper bound soil-geosynthetic interaction results. Poorly-graded fine-grained glass beads with a relatively low friction angle were used to generate lower bound results.

4.4.1 Sand

A poorly-graded, medium-grained sub-rounded SAND manufactured by Badger Mining Corporation (Berlin, WI, USA) was used as the high-friction angle material. This sand was used in previous testing programs (Raju, 1991 and 1995). The particle sizes range from 0.08 to 2.0 mm, with a D_{50} of 0.9 mm. The coefficient of uniformity is $C_u = 1.5$. A grain-size distribution is shown in Figure 4.2.

Direct shear tests performed by Raju (1995) give a peak friction angle (ϕ_p) of 31 to 33 degrees and a constant volume friction angle (ϕ_{cv}) of 26 to 30 degrees in the stress range of interest (5 to 20 kPa); the variation is attributed to a stress dependency at lower normal pressures. The stress dependency was corroborated by the results of the current testing program (see Section

6.2.1). Results of direct shear tests are given in Figure 4.3. These tests were conducted with the sand in a relatively loose state (D_R = 40 to 60 percent).

The minimum and maximum void ratios determined by ASTM D4254-91 and ASTM D4253-93 are 0.47 and 0.62, respectively, using a specific gravity of G_s = 2.65. The in-place density of the material was 17.3 kN/m^3 plus or minus 2 percent.

4.4.2   Glass Beads

Canasphere No. 10 glass beads were used for the low friction material tests. The glass beads were chosen in lieu of natural soil because of their comparatively low friction angle. The glass beads can be described as poorly-graded round fine silty SAND, with particle sizes ranging from 0.220 to 0.050 mm, with a D_{50} = 0.087. The coefficient of uniformity is C_u = 1.7. A grain-size distribution is given in Figure 4.2.

Direct shear tests were performed on the glass beads. Results give a ϕ_p of 28 to 33 degrees, and a ϕ_{cv} varying between 26 and 27 degrees in the stress range of interest. The variation is again attributed to stress dependency. Figure 4.4 shows the friction angles obtained from direct shear tests. It should be noted that although "loose" and "dense" tests were run for each vertical stress applied, the material tended to settle to a stable state with the slightest jar. The variation in friction angles (for each stress level) probably is more representative of experimental variation.

The minimum and maximum void ratios determined by ASTM D4254-91 and ASTM D4253-93 are 0.55 and 0.70, respectively, using a specific gravity of G_s = 2.47. The in-place density of the glass beads material was typically 15.0 kN/m^3 plus or minus 4 percent.

Plan

Profile

GRID	a	b	c	d	e	f	g	h	i
								All dimensions in mm	
UX1400HS	21.0	352	373	5.2	5.3	15	0.9	0.9	2.6
UX1500SB	16.6	153	170	6.1	N/A	15	1.5 - 1.8	N/A	4.5
UX1600HS	16.7	338	355	5.7	5.1	16	2.1	1.7	6.0
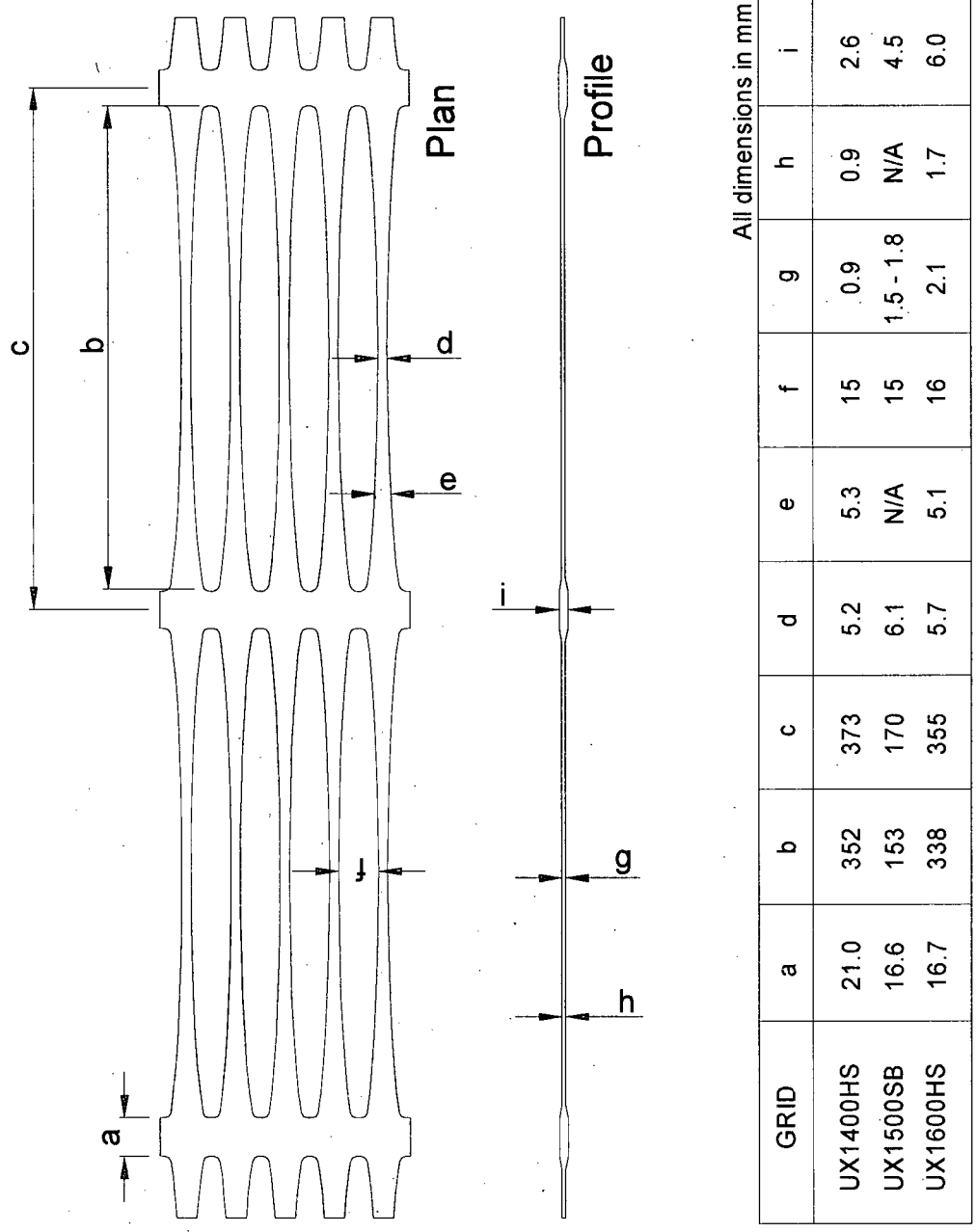
Figure 4.1: Geometry of each Tensar geogrid series
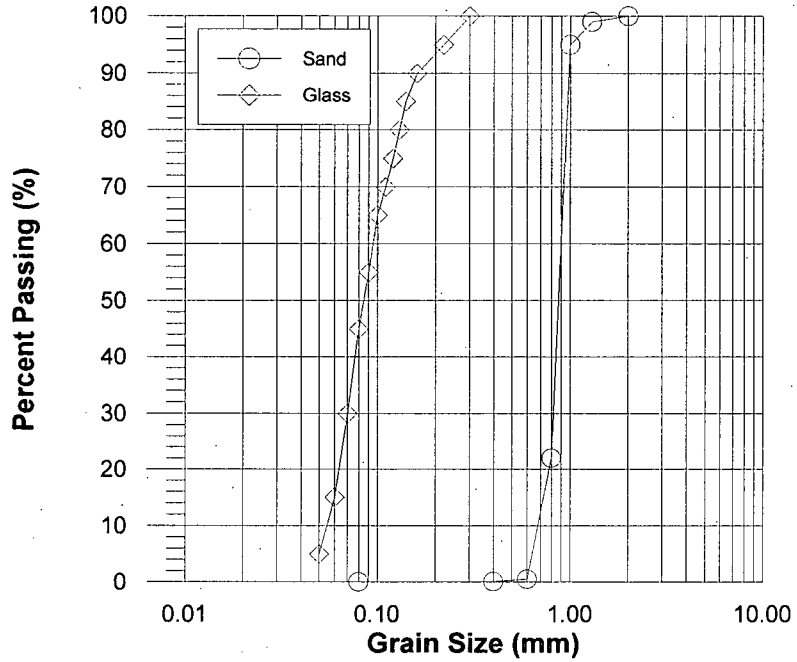
Figure 4.2: Grain size distribution curves for the Badger Mining Sand and Canasphere No. 10 glass beads. The data for the sand are after Raju (1995).
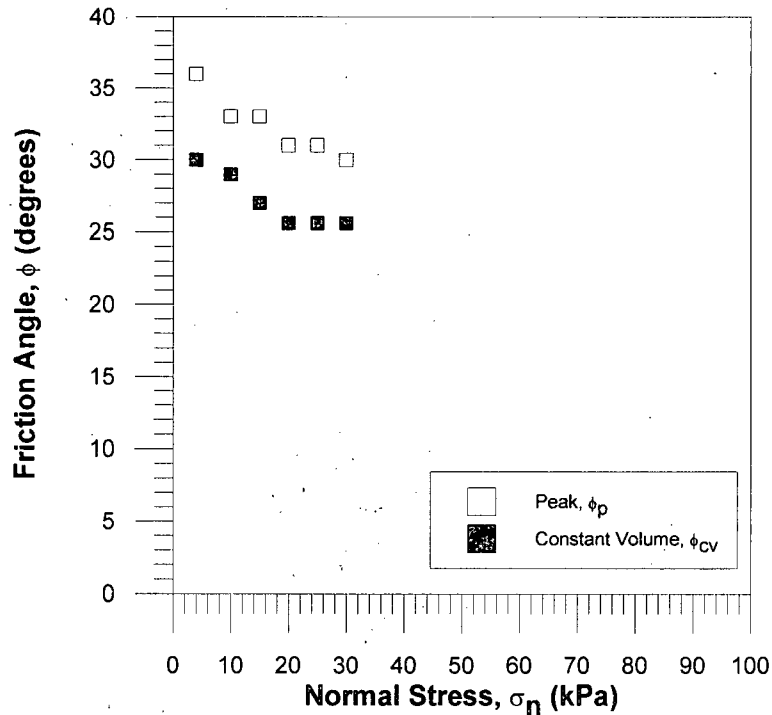
Figure 4.3: Friction angles for the Badger Mining Sand from direct shear tests (after Raju, 1995)
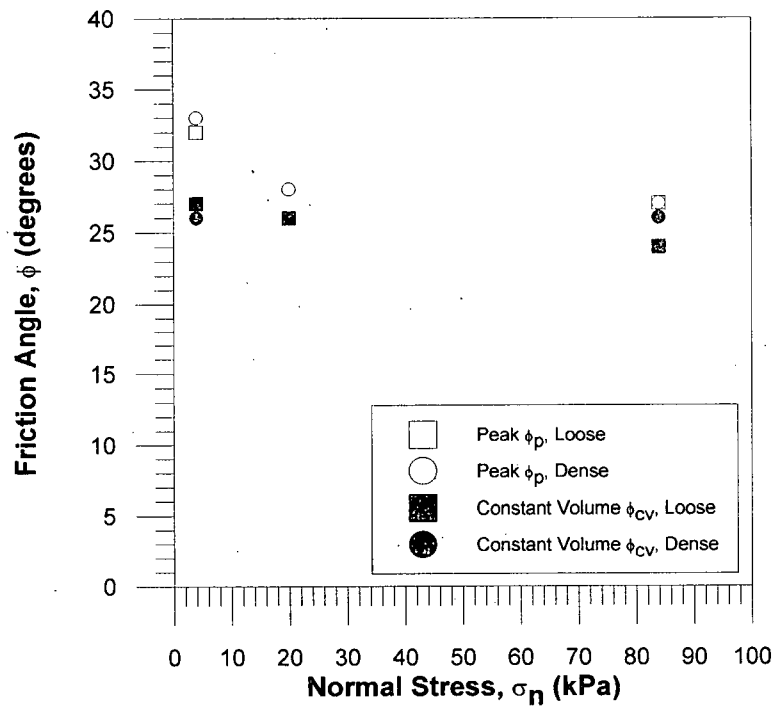
Figure 4.4: Friction angles for the Canasphere No. 10 glass beads from direct shear tests

CHAPTER 5

TESTING PREPARATION AND PROCEDURES

5.1   Introduction

This chapter documents the procedures and methods used to prepare for and complete the pullout tests using the apparatus and equipment described in Chapter 3 and the materials described in Chapter 4. Three types of tests were performed using the pullout apparatus: displacement control, monotonic load control, and cyclic load control. Displacement control was used solely to commission the pullout apparatus and enable comparisons with results from previous studies. Monotonic and cyclic load control comprise the bulk of testing done under this testing program; the methods of each are described below.

The behavior of the geogrids in pullout was characterized from the measured displacement, load, strain, and pressure data generated during testing. The results and analyses are described in the following chapters.

5.2   Test Preparation

Test preparations included geogrid specimen cutting, trimming and strain gauging, pluviation/placement of the soil material, application of the surcharge, attachment and calibration of the transducers and strain gauges, clamping of the geogrid specimen, and initializing the software. These procedures are described below.

5.2.1   Geogrid Preparation

The geogrid specimens were cut from standard 1.3 m rolls supplied by the manufacturer. The specimens were generally cut in rough from the roll and allowed to come flat for several weeks under their own weight. They were then cut to size (length varied by grid type, width was approximately 0.50 m) by hand and trimmed flush with the transverse bars using a metal press. The "roll curl" was then worked out by suspending the grids in air with weights attached or by placing the grids flat underneath weights on a table set aside for this purpose.

Shortly before the grids were to be tested and after they had been pressed flat, strain gauges were attached to the central rib of each grid. Five strain gauges were attached to the UX1500SB grids, while four were attached to the UX1400HS and UX1600HS grids (corresponding to the number of rib sections in each specimen, see Figure 4.1 for details). A detailed procedure for the strain gauge attachment is given in Appendix A. A single hole was then drilled and threaded in the center of the embedded end bar for attaching the tell-tale wire.

5.2.2   Pluviation/Placement of Soil Material

The placement of soil material varied by soil type due to the characteristics exhibited by each soil.

5.2.2.1 Sand Placement

The sand material ["sand"] was placed by air pluviation. A pluviation chamber/hopper specially fabricated to seal onto the top of the pullout box was seated, with a tarp placed over the clamp area and sealed between the box and chamber to catch any leakage of sand from the pluvation process. The trap doors were shut and locked into place, then the front door closed and locked shut. Sand was poured into the hopper from 55-gallon drums lifted by an overhead crane into the hopper to an approximate 8 to 10 cm height. The sand was shaped preferentially in the hopper to yield a level surface once pluviated into the pullout box. The trap doors were opened by a set of pneumatic plungers released by a toggle switch mounted on the chamber, which initiated the pluviation. The pluviation process generally gave a lift thickness in the box of 60 to 80 mm from an initial deposit of 80 to 100 mm in the hopper.

In total, eight lifts of soil were placed by this method—four lifts up to mid-height of the pullout box where the specimens were inserted, and another four lifts to near the top of the box. The fourth and eighth lifts were poured to yield a surface at a specific elevation; any low spots were filled by spot-pluviation through the hopper, then leveled using a set of screeds cut to fit the top of the box and yield a target surface elevation. Any excess sand was removed by a flat-bottomed scoop in small layers to avoid disturbance of the underlying soil.

Density measurements were generally taken at three locations along the centerline of the box on the second and seventh lifts, to ensure consistency in sand placement. The density

measurements consisted of placing 256 mL tins on the sand surface before pluviation; the tins were then retrieved and weighed prior to placement of the next lift. Density variations were consistently under 2 percent for the sand.

5.2.2.2 Glass Beads Placement

The glass beads ["beads"] were placed by compaction. For a discussion of the reasons for the difference in placement methods, see Appendix B.

Prior to placement of any beads, the box was thoroughly cleaned. Beads were placed in the box by scoop at a very low drop height (less than 100 mm), to a lift height of approximately 80 mm. The lift was then leveled using a screed. A 19 mm laminated plywood sheet was placed on the beads, then a 25 mm aluminum plate and 13 mm steel disk was placed on top of the plywood. The beads were compacted in place by locating the disk and plate in three locations and imparting a 7.46 N·m blow 35 times (using a Standard Proctor drop-hammer) in each location. The plywood, disk, and plate were removed and the process repeated.

Eight lifts were placed in this manner, four to mid-height and another four to the top of the box. At the fourth and eight lifts, additional material was placed prior to compaction to yield a surface slightly higher than the target elevation after compaction. The surface was screeded in layers to its target elevation and additional material removed as described above.

Consistent with the procedure for placement of the sand, density measurements were generally taken at three locations along the centerline of the box on the second and seventh lifts, to ensure consistency in bead placement. The density measurements consisted of placing 256 mL tins on the sand surface before pluviation; the tins were then retrieved and weighed prior to placement of the next lift. Density variations for the glass beads were consistently under 4 percent.

5.2.3   Attachment of the Strain Gauges

Once the elevation of the soil material was brought to mid-height of the box, tubes containing the strain gauge wires were fed through the instrumentation exit hole on the back boundary of the box. A wax-paper guide was inserted between the weatherstripping in the front

slot to facilitate placement of the strain-gauged grid. A board was placed on top of the box to form a working surface for soldering of the strain gauges. The geogrid specimen was carefully placed on the board, and the strain gauge wires were soldered to the strain gauges in accordance with the procedures given in Appendix A.

5.2.4 Application of the Surcharge Loading

The surcharge—if above the nominal 5 kPa produced by the self-weight of the soil material—was applied by the use of a pressurized PVC water bag. Once the eighth and final lift of the soil material had been placed and screeded level, the empty PVC water bag was gently lifted into place. The steel top plate was lowered onto the top of the box, with the two hoses from the PVC bag pulled through the holes drilled into the plate for this purpose (see Figure 3.2). The plate was bolted securely to the frame using two reaction bars across the top of the plate. Care was taken not to pinch the bag between the top plate and the box frame.

One hose was connected to the water level reservoir which in turn was connected to the laboratory water supply. The other hose was left open to the atmosphere. The water supply was turned on and pressure was allowed to build in the water level reservoir to speed the filling of the water bag. Once the water level started to rise in the free hose, pressure in the reservoir was returned to atmospheric and the water supply was shut off. The water level in the hose was allowed to equilibrate with the reservoir near the top of the open hose, which was then connected to the pressure transducer. The height of the water level in the reservoir above the water pressure transducer was measured and the water pressure at the top of the soil calculated. This was verified with the measured water pressure in the transducer.

5.2.5 Calibration of the Strain Gauges

With the surcharge applied, the rear tell-tale LVDT was attached to the tell-tale wire and a shunt calibration conducted on the strain gauges. The shunt calibration consisted of "shorting" one leg of the Wheatstone Bridge circuit with a known resistance to produce a given voltage difference at the bridge output. The digital output on the computer could then be directly calibrated to a known "strain". The new calibration factors were then entered into the software and the data collecting process initiated.

5.2.6 Clamping of the Test Specimen

With all transducers and gauges connected and the software in data collection mode, the hydraulic power supply was switched on and the clamp positioned by manual control. The central insert and upper jaw were bolted to the lower jaw, then "C" clamps were installed at the ends of the clamp assembly to prevent any movement of the grid in the clamp while testing.

5.2.7 Software Initialization

The software package allows for three types of control: displacement, monotonic load, and cyclic load. The appropriate control was selected, and the loading/displacement rate, displacement limit, geogrid geometry, and cyclic parameters (if relevant) were specified. The software then began the loading sequence.

5.3 Testing Procedures

Three modes of testing were used: displacement control, monotonic load control, and cyclic load control.

For displacement control, a linearly increasing displacement demand signal was fed from the computer to the controller, which then displaced the hydraulic actuator to match the demand. The rate of displacement for all tests was $r_d = 0.5$ mm/min; the demand signal is shown in Figure 5.1. The test was terminated when the actuator reached its stroke end or a target displacement (depending on the stage in the test, see Table 6.1).

For load control, a demand signal was fed by the computer to the controller, which displaced the actuator to match the demand load. Under the monotonic loading regime, the loading was $r_l = 0.25$ kN/m/min; the demand signal is shown as a dashed line in Figure 5.2. Under the cyclic loading regime, a linearly increasing load (at $r_l = 0.25$ kN/m/min) was specified until the load cell registered a "working load" of $P_w = 3$ kN/m, at which point the demand load became a sinusoidal half-wave of increasing amplitude after each set of "N" cycles. The amplitude increase varied from test to test and was selected on the basis of the corresponding monotonic test, but was generally in the range of $\Delta P = 0.75$ to 1.50 kN/m. For this study, the load frequency was $f = 0.5$ Hz, to best represent a real seismic event while still enabling sufficient data

acquisition to clearly define the cycles. The value of N was chosen to allow pullout to come to dynamic equilibrium yet still allow for enough cycle sets to reach failure conditions. Initially N was set at 10 for all cycles, then was stepped up to 15 to better define stability (see Section 7.3). The test was terminated when the actuator reached its stroke end. The cyclic demand signal is shown as a solid line on Figure 5.2.

Because of the limitations of the MTS hydraulic system, only 75 mm of the available 150 mm actuator stroke could be used under displacement control. However, load control allowed use of the full stroke.

While the tests were underway, the software simultaneously generated the proper demand signal and monitored and recorded 16 channels of data from transducers and strain gauges. For the displacement control and monotonic load controls tests, the input channel scan interval was specified at two seconds; during the cyclic portion of the cyclic load control tests the input channel scan interval was increased to 0.1 second to allow complete numerical reconstruction of the test.

5.4   Post-Test Procedure

Upon termination of the test, data acquisition was stopped and the hydraulic power supply was shut off. The surcharge was removed (if any), and the specimen was released from the clamp. The soil material was scooped by hand back into the barrels until mid-height of the box was reached. The geogrid sample was carefully examined for damage and exhumed from the box, the strain gauge wires and tell-tale removed, and the grid tagged for later identification. The balance of the soil material was scooped into the barrels and the box cleaned in preparation for the next test.
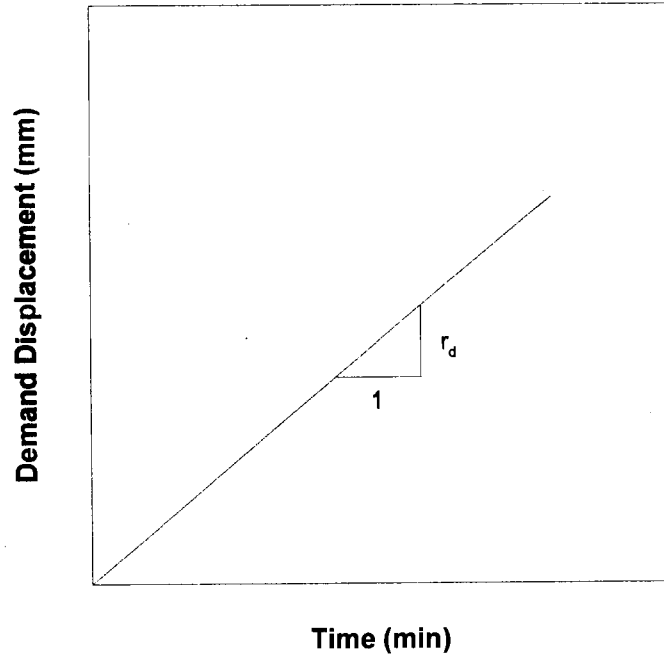
Figure 5.1: The displacement demand signal generated by the computer for displacement-controlled tests
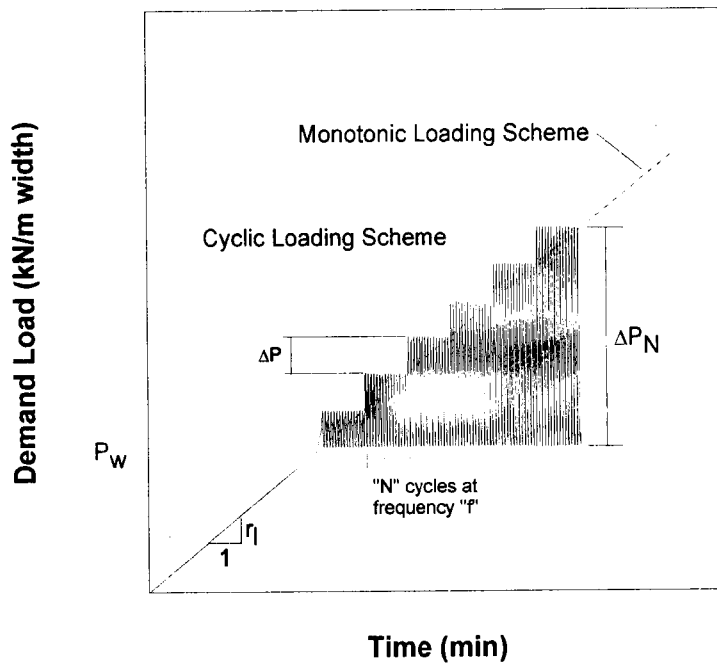
Figure 5.2: The load demand signals generated by the computer for the load-controlled tests (both monotonic and cyclic)

CHAPTER 6

TEST RESULTS

6.1   Introduction

Presented in this chapter are the results from preliminary (roughened aluminum plate), benchmark, and higher and lower friction material tests, see Table 6.2. The results presented are given in graphical format, appended to the end of the chapter. Variables that are examined are: repeatability, normal stress, geogrid type (stiffness and to some extent geometry), soil type, and the effect of dynamic loads versus static (monotonic) loads.

All tests except for the preliminary tests were performed under load control. Test designations are explained in Table 6.1 and are listed with their respective variables in Table 6.2, both shown at the end of this chapter.

6.2   Preliminary Tests

To ensure compatibility in results from this testing program to that of Raju (1995), a series of preliminary tests were run with the same sand material and inclusions used in the previous program. The objectives of running the preliminary tests were to: recommission the testing apparatus with appropriate changes made, test the new system software, and "benchmark" the results of this series of tests with those produced in the previous study.

6.2.1   Roughened Aluminum Tests

Two aluminum plate tests were run under similar conditions imposed by the previous study (Raju, 1995). The rate of displacement was $r_d = 0.5$ mm/min and the applied normal stress varied between 5 and 20 kPa. Plots of measured pullout load versus the plate displacement are shown in Figures 6.1 and 6.2. Both aluminum plate tests were "staged tests", in which a higher surcharge pressure was applied after the pullout force reached an approximate visual constant value (on the computer screen) at the initial surcharge pressure. Each test comprised two parts: two staged tests followed by a drop in load to zero, then another two stages. The limitation on stroke length during displacement-controlled tests required the test to be stopped and reinitialized after the first 75 mm of stroke displacement.

Because the roughened aluminum plate is inextensible, the measured pullout load and displacement were used to calculate an average shear stress (τ) acting on both sides of the plate (assumed to be equal on top and bottom). The shear stress was normalized by the applied normal stress (σ) to yield an instantaneous interaction factor (τ/σ) for each test. These results are given in Figure 6.3, along with data reproduced from a previous study (Raju, 1995). The results from this recent set of tests compare reasonably well with the results obtained by Raju, both in terms of actual instantaneous interaction factors and general behavior. However, the trend of large-displacement interaction factors with varying applied normal stress is exactly opposite from Raju's results to the current tests—the current series suggests higher normal stresses yield lower interaction factors, whereas Raju's tests suggest higher normal stresses yield higher interaction factors, for the range of normal stresses investigated. Based on the results of direct shear tests run on the Badger Mining Corp. sand (Raju, 1995) and work by Houlsby (1994), the trend of decreasing interaction factor with increasing normal stress is considered the correct trend.

6.2.2   UX1500SB Test

Once it was decided the apparatus and software were working properly and producing verifiable results, a load-controlled monotonic test was performed using the same grid series tested by Raju, the UX1500SB. It should be noted that the UX1500SB samples used in this testing program were taken from a different roll than that used in the previous study (Raju, 1995) and contained a notable difference in the rib lengths (145 mm in the previous study, 153 mm in this study). The difference is attributed to manufacturing variation between production runs; the manufacturing process did not produce measurable differences in all other geogrid dimensions. This test was performed at 10 kPa in the same soil material in an attempt to address the difference between load control (used in this study) and displacement control (Raju, 1995). The load-displacement results from this test and two performed by Raju are shown in Figure 6.4. Two of Raju's tests are shown to give an idea of the range of pullout load values that may be expected in repeatable tests. The results suggest that load control will yield a slightly higher pullout load than a test conducted under displacement control, under the same conditions. The embedment length in this test series was approximately 2 percent more than in the previous study due to the geometric difference; a theoretical (calculated) increase in frictional resistance due to more embedded surface area can account for only a small portion of the higher pullout load measured in this study.

6.3   Testing Program

The testing program comprises sixteen (plus two repeated) load-controlled monotonic and cyclic tests. The variables under investigation are: normal stress, geogrid type (geometry and stiffness), and soil type. Each cyclic test for a given geogrid type, surcharge pressure, and soil type is paired with a corresponding monotonic test. All test specimens were strain-gauged as described in Chapter 5 with the exception of s1500m10.

6.3.1   Pullout Load

Figures 6.4 through 6.11 show the measured pullout load versus displacement at the clamped end for each monotonic/cyclic pair. The pullout load profile exhibits a similar pattern in each monotonic test —an initial stiff, linear portion that takes up approximately 70 percent of the ultimate load, a non-linear transition stage, followed by a plateau that defines the approximate failure pullout load. Typically the cyclic tests followed the same initial linear portion of the monotonic curve closely until the cyclic demand load exceeded the monotonic pullout failure load. At this point, the incremental displacement with each cycle increased significantly (see Section 7.3 for a discussion of this incremental displacement). Figures 6.10 and 6.11 show this behavior clearly. Originally the software was programmed to demand seven load cycle sets for the cyclic tests, which was amended to include further cycles after the s1600d5 and s1600d5R tests.

The monotonic tests for the 1600 series grids embedded in both the sand and the glass beads are shown in Figure 6.12. Each test shares the same initial stiff linear loading curve. The sand tests show a smooth, gentle transition to the respective maximum pullout load, whereas the glass beads tests display a markedly short transition to a maximum load, particularly at the lower normal pressures. The ultimate pullout loads for the tests conducted in the glass beads were consistently 65 to 75 percent of the counterpart sand tests.

The performance of each grid series varies significantly, as can be seen in Figures 6.4, 6.6, and 6.8. The stiffest grid—the UX1600HS—has the stiffest response in soil, whereas the least stiff grid, the UX1400HS, shows considerable extensibility at low pullout loads. To enable better comparison of the loads sustained by the grids, the measured loads for each grid were

normalized by the instantaneous embedded length and plotted in Figure 6.13. The UX1500SB grid clearly sustains more pullout load under the same conditions, with the UX1600HS holding more than the UX1400HS. The discrepancy in ultimate pullout load can be explained by the geometric differences in each grid. The UX1500SB is a relatively thick grid (on the order of the UX1600HS) with short ribs; a test with this grid involves six embedded transverse bars. The UX1400HS and UX1600HS grids have longer ribs (giving four embedded bars in a test), and the profile of the UX1400HS is significantly thinner than the 1500 and 1600 series grids (Figure 4.1 gives dimensions for each grid series). Figure 6.13 suggests the number of transverse bars embedded in the soil and the profile differential between the bars and ribs both have a pronounced effect on the unit pullout capacity of the soil/geogrid composite. This discussion is limited to the low tensile forces imposed and does not account for ultimate strength differences between the grid series (i.e., a grid may fail in tension before pullout occurs).

6.3.2 Embedded-End Displacement

The embedded-end displacements (d_e) were measured to quantify the elongation endured by each grid until pullout occurred. Displacement of a grid has been found to follow a simple pattern described in Figure 6.14 (Raju, 1995). Initially the clamped end is displaced (d_c) without any movement occurring at the embedded end; this is termed Stage I. ($d_c>0$, $d_e=0$). As the applied load increases, the embedded end begins to move but the grid is still straining differentially; this is called Stage II ($d_c{\neq}d_e$, $d_c>0$, $d_e>0$). Stage III defines inextensible behavior, where the grid displaces with little or no internal strain ($d_e=d_c$, $d_c>0$, $d_c>0$).

Figure 6.15 shows the embedded end movements for each monotonic 10 kPa tests conducted in this study. The UX1600HS grids reached Stages II and III at approximately 8 and 10 mm. The s1600m10 and g1600m10 curves lay almost on top of each other, implying similar strain behavior for the grid in these two different soils. The 1400 and 1500 series grids began Stage II at approximately 10 mm, but the 1400 series grid did not reach Stage III until approximately 40 mm. This behavior is consistent with the stiffness of each geogrid series; these values can be seen in Table 4.1.

Figures 6.16 and 6.17 show the embedded displacements for the UX1600HS grids in the sand and glass beads, respectively, under monotonic loading. It is expected that the higher surcharges would produce a longer Stage I (progressive elongation of the grid without

displacement of the embedded end); the results indicate this to be the case except for test s1600m5—it is unclear why this particular grid strained to the extent it did before mobilizing the embedded end.

6.3.3 Rib Strain

All tests except for the initial UX1500SB test were strain gauged using high-elongation foil strain gauges. The strain gauges were affixed longitudinally on or near the mid-point of the ribs for the embedded portion of all grids and the exposed portion of the 1500 series grid; the 1400 and 1600 series grids required the in-air strain gauge to be mounted approximately 120 mm from the front transverse bar for proper placement allowing full clamp movement.

Measured rib strains for each test are given in Figures 6.18 through 6.32. Generally, the measured strains follow a pattern (in shape) similar to that of the measured pullout force. The gauges closer to the front of the box indicate progressively higher strains than those further to the back, although this trend is not universal (see Figures 6.18 and 6.21). The peak values of strain in the cyclic tests tend to be less than the corresponding values of strain in the monotonic tests, most likely due to a combination of short periods of peak loading and increased rib stiffness under relatively quick "pulse" loads.

Interesting results occur in four or more of the tests (see Figures 6.20, 6.24, 6.27, 6.28, 6.31, and 6.32). In each of these tests, the last strain gauge (SG4, the furthest embedded) tended toward or became negative at some stage in the test, implying compression of the rib along the rib axis. Although no work was conducted to test this hypothesis, it is felt the embedded portion of the geogrids did not undergo uniform pullout across the width of the specimens. Non-uniform pullout would result in some elements of the grid being placed into compression. Raju's work shows the extent of non-uniformity that was encountered in his pullout tests (see Figure 6.14, 1995) that provides the basis for this conjecture. Because of the regular pattern of the decrease in tension along the center rib in each strain gauge of these tests (see g1600d5, Figure 6.28), it is not felt that this phenomenon is due to error(s) in instrumentation or data reduction but instead represents the true state of strain at the points measured.

The influence of grid stiffness is apparent in the results. At a displacement of $d_c = 60$ mm the UX1400HS strained two to three times the UX1600HS subjected to the same surcharge

pressure (σ_v = 10 kPa) and embedded in the same soil (sand, see Figures 6.25 and 6.26 versus Figures 6.21 and 6.22). This difference is consistent with the ratio of stiffnesses. The UX1500SB grid strained approximately 75 percent more than the UX1600HS grid, again consistent with the ratio of stiffnesses between these grids.

The UX1600HS grid's strain behavior varied with the change of soil types. This was most pronounced at σ_v = 10 kPa, as shown by comparing Figures 6.23 and 6.24 (s1600m/d20) with Figures 6.31 and 6.32 (g1600m/d20). The strains measured during the glass beads tests are typically less than strains measured in the tests conducted in the sand, which is most likely attributable to the lower friction angle of the glass beads (lower measured strains due to a lower stress in the geogrid ribs, due to a lower mobilized pullout load).

6.3.4   Total Normal Stress

Because the applied surcharge pressure above the self-weight of the soil material was applied hydrostatically and hence varied as the tests progressed, the total applied normal stress is reported here. Figures 6.33 to 6.36 show the measured pressures for both the monotonic and cyclic tests in each series.

The surcharge pressure tended to increase as the tests progressed in all but one case (Figure 6.34, test s1600m20) which is to be expected as the soil material dilates during shearing. The cyclic tests show an increase in pressure with increased peak demand pullout force due to sustained clamp displacement through even the bottom end of the cycles (further shearing leading to further dilation).

It is expected that this progressive increase in pressure affected the resistance to pullout. For this reason, calculations performed in the analyses presented in Chapter 7 account for this by normalizing measured pullout loads by the total normal stress.

6.4   Summary of Results

Results of the pullout testing program on Tensar geogrids presented above suggest the following:

1. Roughened aluminum plate pullout tests were conducted to test modifications made to the software and testing apparatus. Comparisons of the results from these tests to results of a previous study (Raju, 1995) are within 20 percent.

2. A load-controlled pullout test was conducted with a UX1500SB placed under conditions of normal stress and soil material identical to two displacement-controlled tests run by Raju (1995). The results suggest that load-controlled tests yield slightly higher pullout loads than displacement-controlled tests under otherwise identical conditions.

3. In all monotonic/cyclic test pairs conducted, the pullout resistance for the cyclic tests met or exceeded the pullout resistance for the corresponding monotonic test. This was irrespective of total normal stress, soil material type, or geogrid series.

4. The UX1600HS pullout behavior differed in the sand and glass beads; the maximum pullout load in the glass beads was approximately 65 to 75 percent of the maximum pullout load measured in the tests conducted in sand.

5. Each grid series' behavior in the sand varied due to geometric and stiffness differences.

6. Embedded-end displacement of geogrids embedded in a soil material follow the pattern shown in Figure 6.14 during pullout testing. The stiffness of a particular geogrid and the applied normal stress both influence how and when the transition from one stage to the next takes place.

7. Peak strains measured in the cyclic tests were less than those measured in the corresponding monotonic tests, most likely due to the faster rate of loading.

8. Measurements of rib strain indicate strain non-uniformity over the geogrids' plan areas and that compression of some areas of the geogrids was taking place.

9. The applied surcharge pressures tended to increase as the tests progressed. The analyses presented in the following chapter account for this effect.

Table 6.1: Key to test designations

| Soil Type	Grid Type	Control Type	Normal Stress (nominal)	Test Characteristics
s = sand g = glass beads	a = aluminum plate 1400 = UX1400HS 1500 = UX1500SB 1600 = UX1600HS	crd = displacement control m = monotonic load control d = cyclic load control	5 kPa 10 kPa 20 kPa	R = repeated test stg = staged test

Table 6.2: Summary of pullout tests, with variables

|		Test Code	Nominal Applied Surcharge Pressure, σ_v (kPa)	Initial Specimen Embedment Length, L_{ei} (mm)	Type of Control (1)	Soil Material (2)	Inclusion Type (3)
	Preliminary Tests	s-a-crd5 (test 1)	5.4	964	crd	s	a
		s-a-crd10stg (test 1)	10.2	919	crd	s	a
		s-a-crd15stg (test 1)	15	887	crd	s	a
		s-a-crd20stg (test 1)	20	853	crd	s	a
		s-a-crd5 (test 2)	5.5	965	crd	s	a
		s-a-crd10stg (test 2)	10.1	919	crd	s	a
		s-a-crd15stg (test 2)	15.1	888	crd	s	a
		s-a-crd20stg (test 2)	20.1	849	crd	s	a
Main Test Program	Higher Friction Material	s1500m10 (benchmark)	10.0	983	m	s	1500
		s1500d10	10.0	974	d	s	1500
		s1600m5	5.2	1270	m	s	1600
		s1600m10	10.0	1255	m	s	1600
		s1600m20	20.0	1262	m	s	1600
		s1600d5	5.2	1259	d	s	1600
		s1600d5R	5.2	1261	d	s	1600
		s1600d10	10.0	1219	d	s	1600
		s1600d10R	10.0	1260	d	s	1600
		s1600d20	20.1	1278	d	s	1600
		s1400m10	10.0	1277	m	s	1400
		s1400d10	9.9	1279	d	s	1400
	Lower Friction Material	g1600m5	4.5	1266	m	g	1600
		g1600m10	10.0	1241	m	g	1600
		g1600m20	20.0	1284	m	g	1600
		g1600d5	4.5	1249	d	g	1600
		g1600d10	10.0	1252	d	g	1600
		g1600d20	19.9	1280	d	g	1600

(1) crd = displacement, m = monotonic (load), d = cyclic (load)
(2) s = sand, g = glass beads
(3) a = aluminum plate, 1400 = UX1400HS, 1500 = UX1500SB, 1600 = UX1600HS
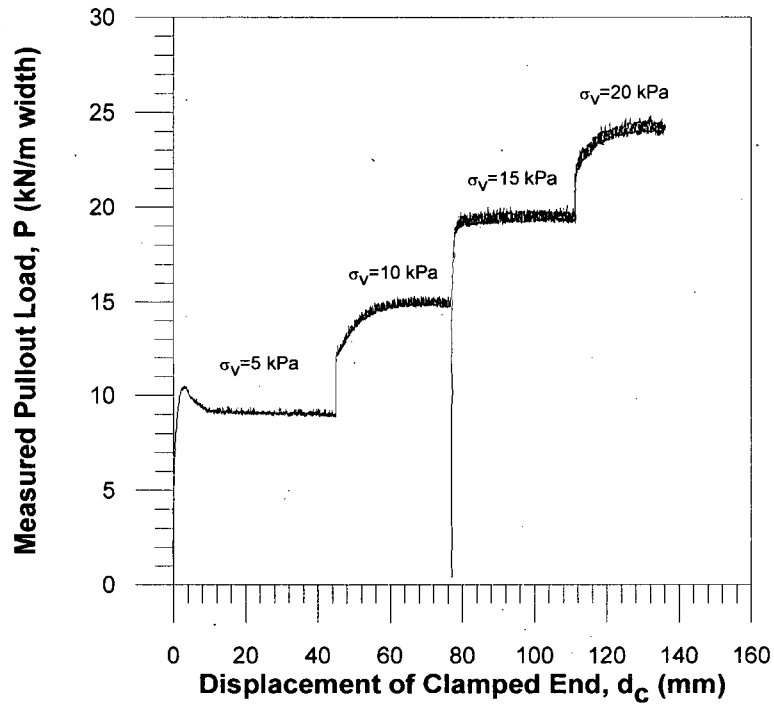
Figure 6.1: Measured pullout load of the fully roughened aluminum plate in the sand at four values of normal stress (Test 1)
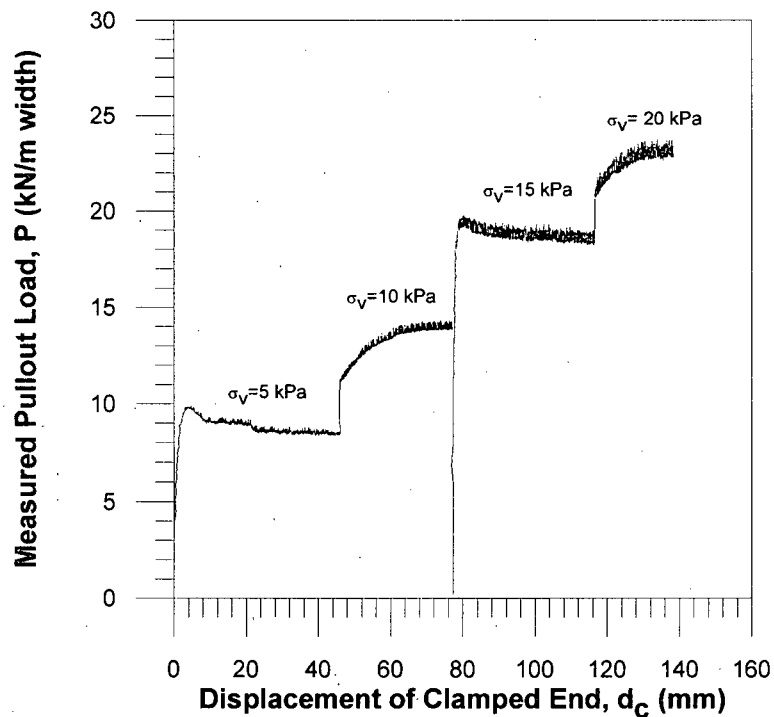
Figure 6.2: Measured pullout load of the fully roughened aluminum plate in the sand at four values of normal stress (Test 2)
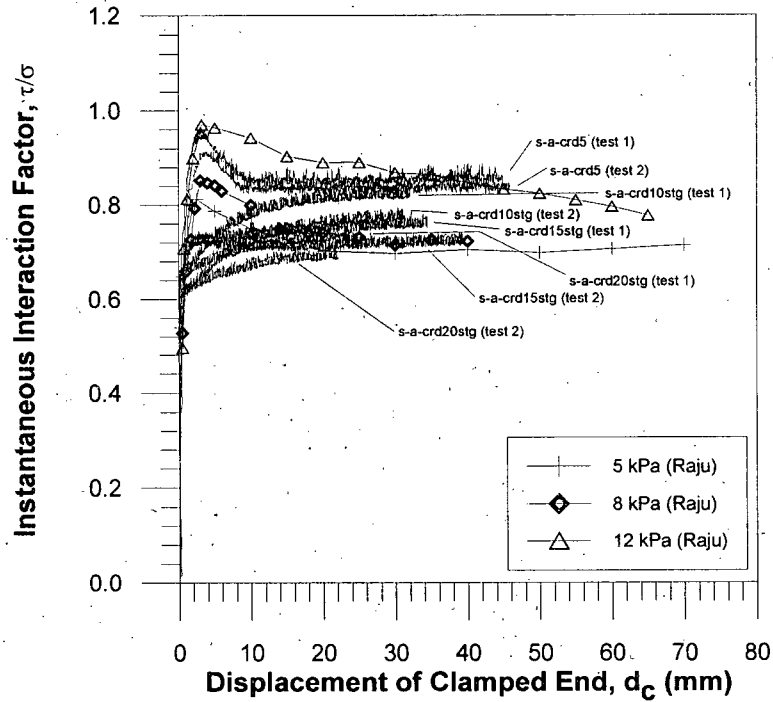
Figure 6.3: Instantaneous interaction factors for aluminum plate pullout tests compared to those performed by Raju (1995)
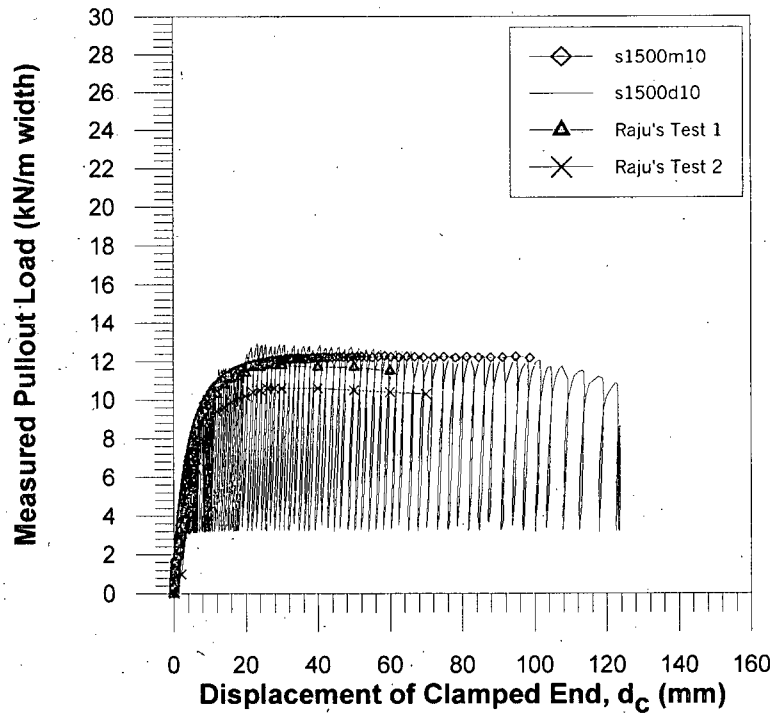
**Figure 6.4: Measured pullout load for the Tensar UX1500HS in sand under $\sigma_v = 10$ kPa. Raju's Test 2 is a repeated test (after Raju, 1995)**
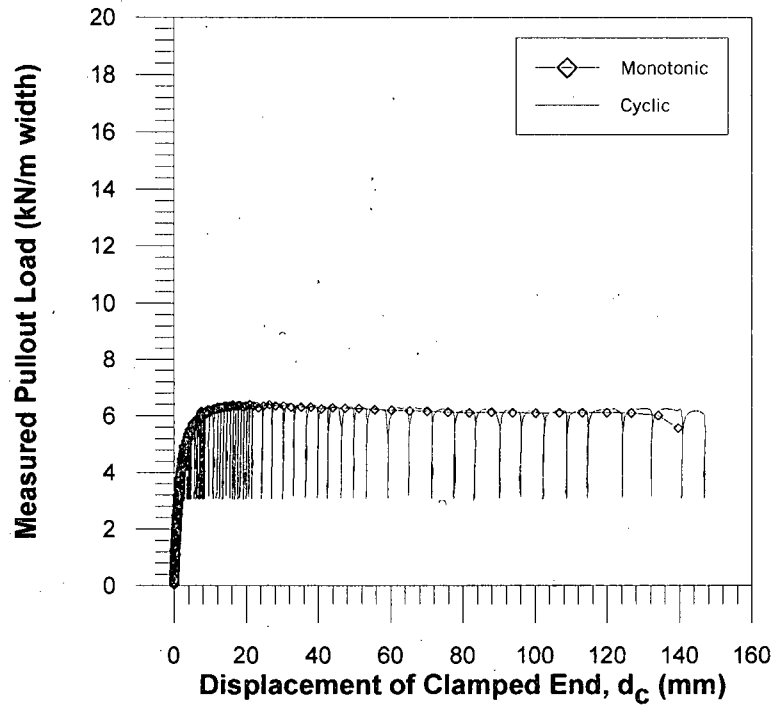
Figure 6.5: Measured pullout loads for the s1600m5 and s1600d5R tests,
σ_v=5 kPa
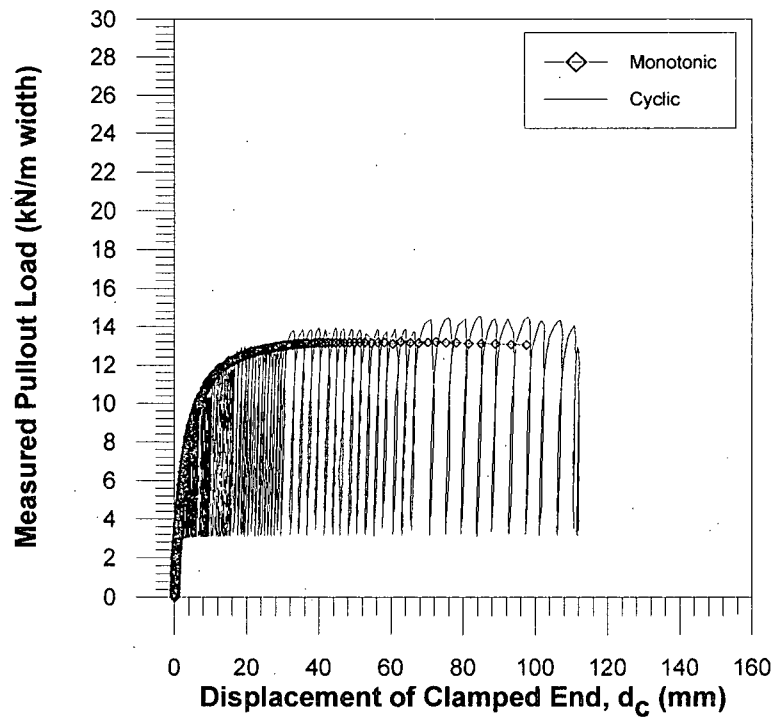
Figure 6.6: Measured pullout loads for the s1600m10 and s1600d10R tests,
σ_v=10 kPa
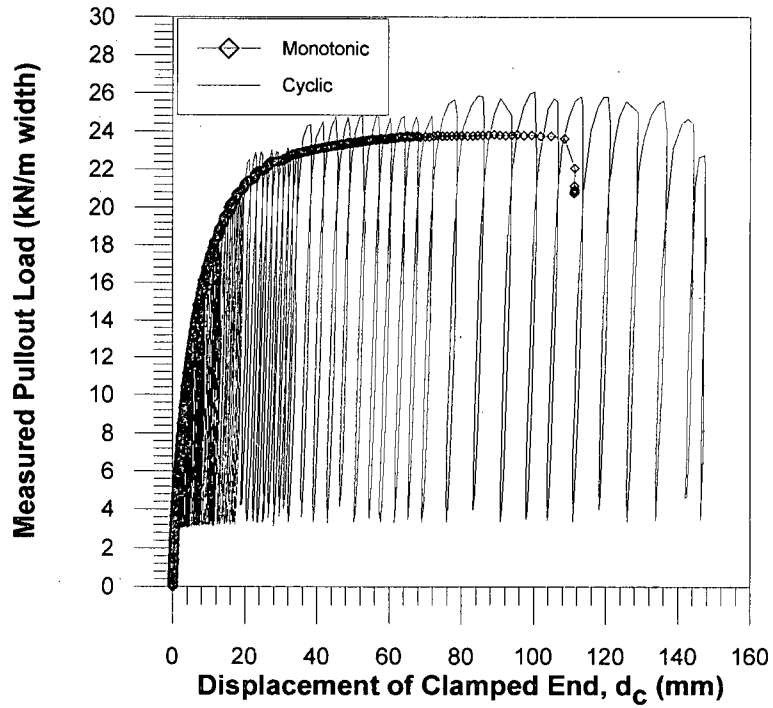
Figure 6.7: Measured pullout loads for the s1600m20 and s1600d20 tests, σ_v=20 kPa
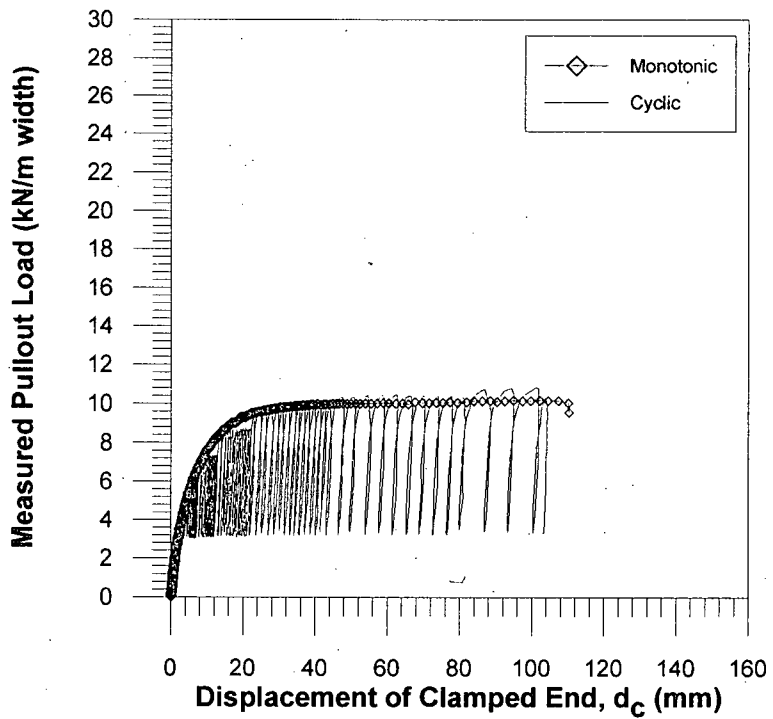
Figure 6.8: Measured pullout loads for the s1400m10 and s1400d10 tests, σ_v=10 kPa
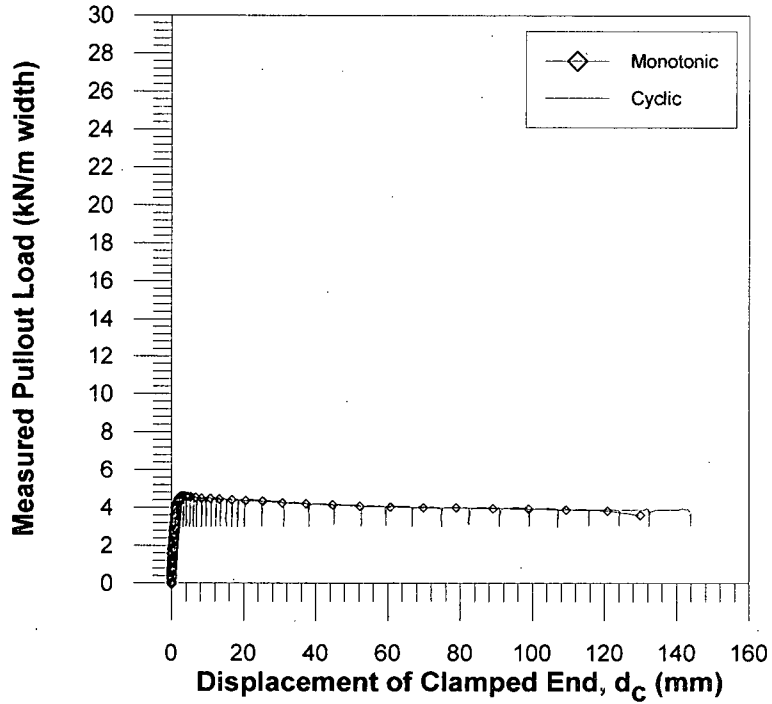
Figure 6.9: Measured pullout loads for the g1600m5 and g1600d5 tests, σ_v=5 kPa
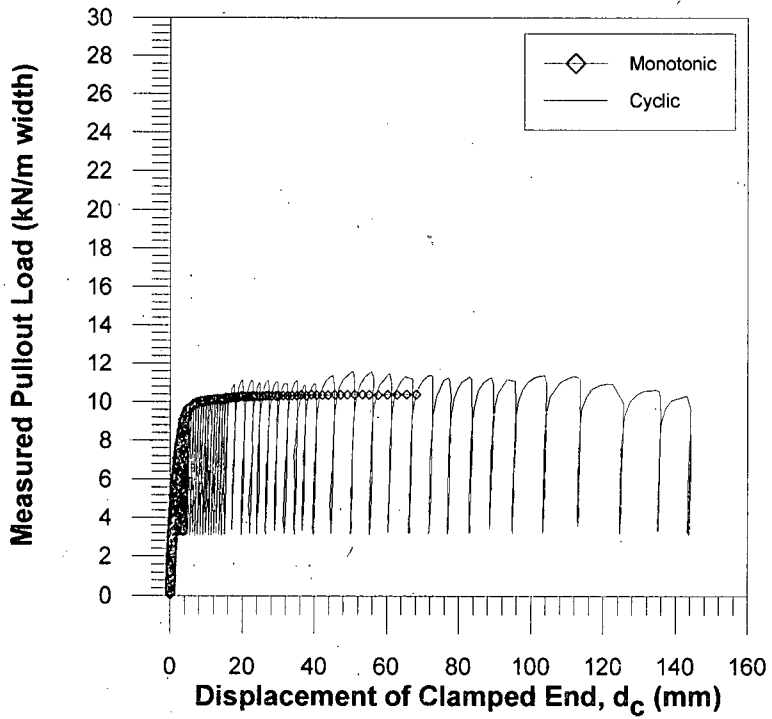

Figure 6.10: Measured pullout loads for the g1600m10 and g1600d10 tests, σ_v=10 kPa
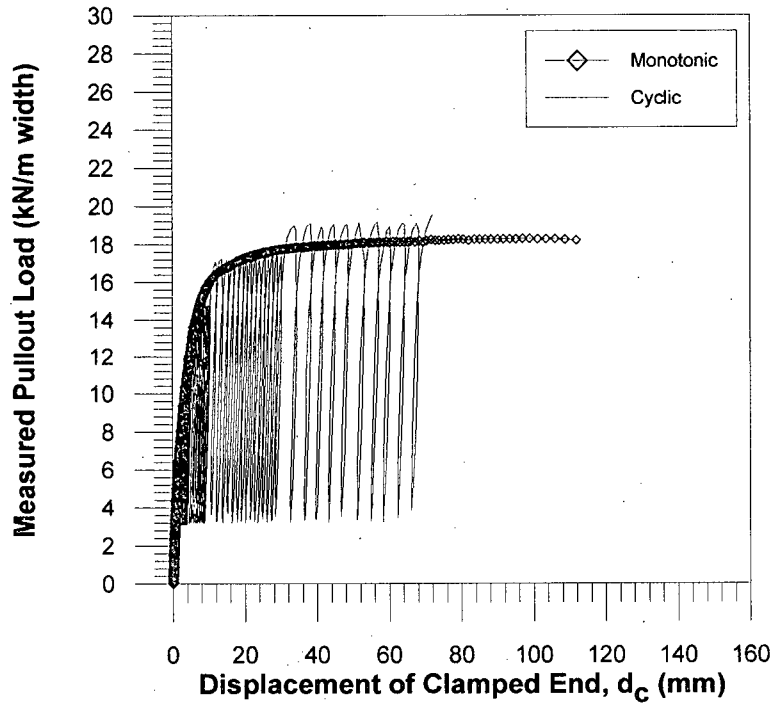
Figure 6.11: Measured pullout loads for the g1600m20 and g1600d20 tests, σ_v=20 kPa
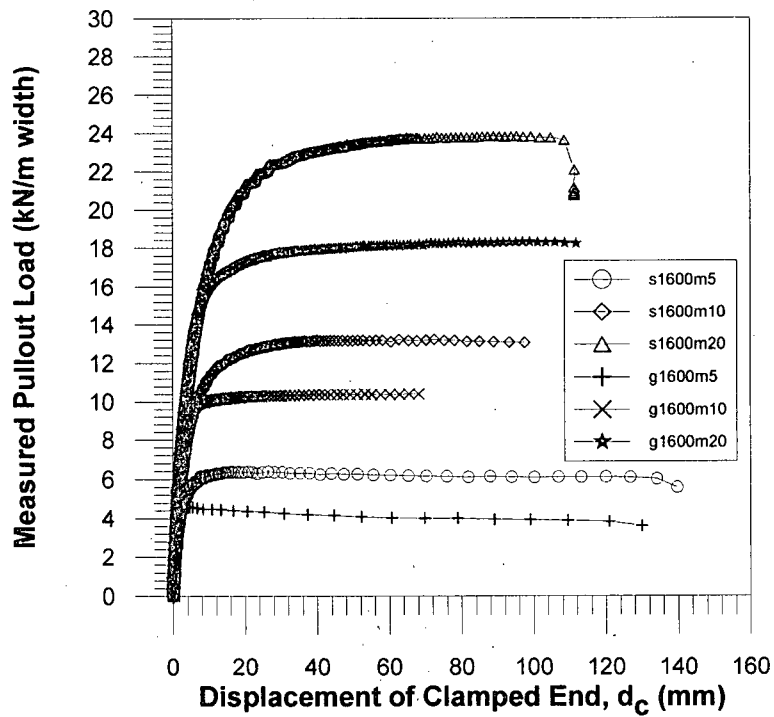
Figure 6.12: Measured pullout loads for the UX1600HS tests in sand and glass beads, at varying normal stresses
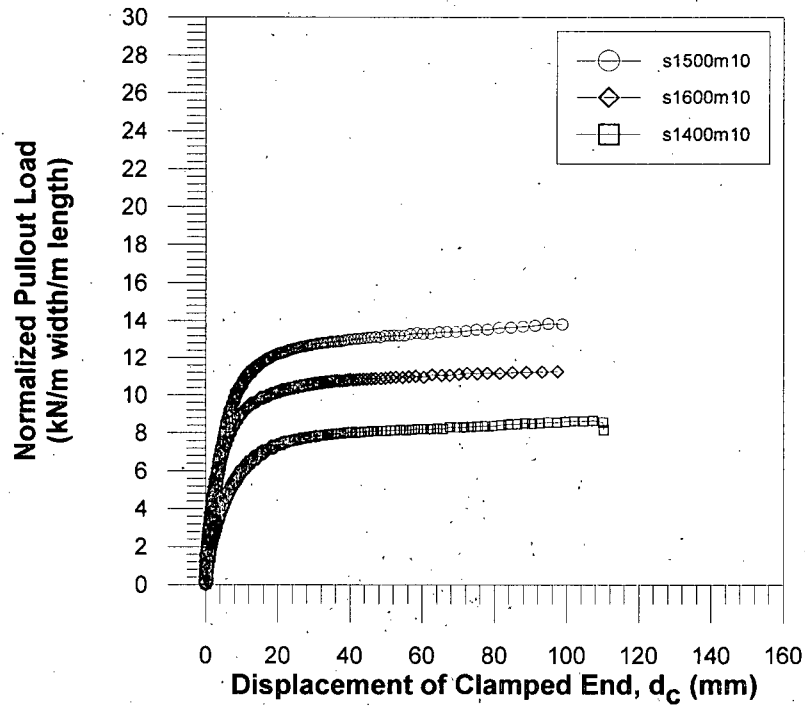
Figure 6.13: Normalized pullout loads for the UX1400HS, UX1500SB, and
UX1600HS tests showing the influence of geogrid geometries
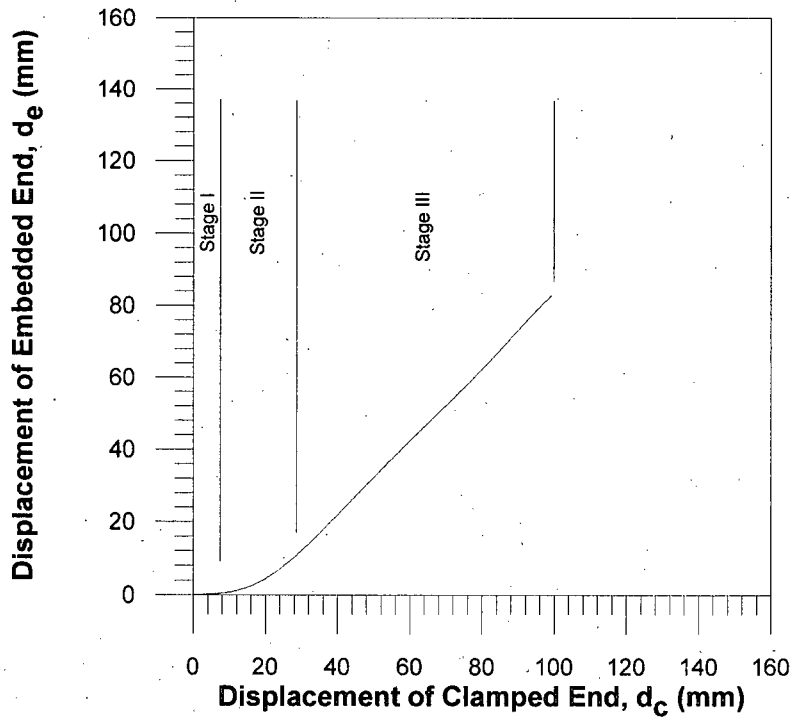
Figure 6.14: An idealized curve showing the progression of embedded-end
displacement of a geogrid, through Stages I, II, and III
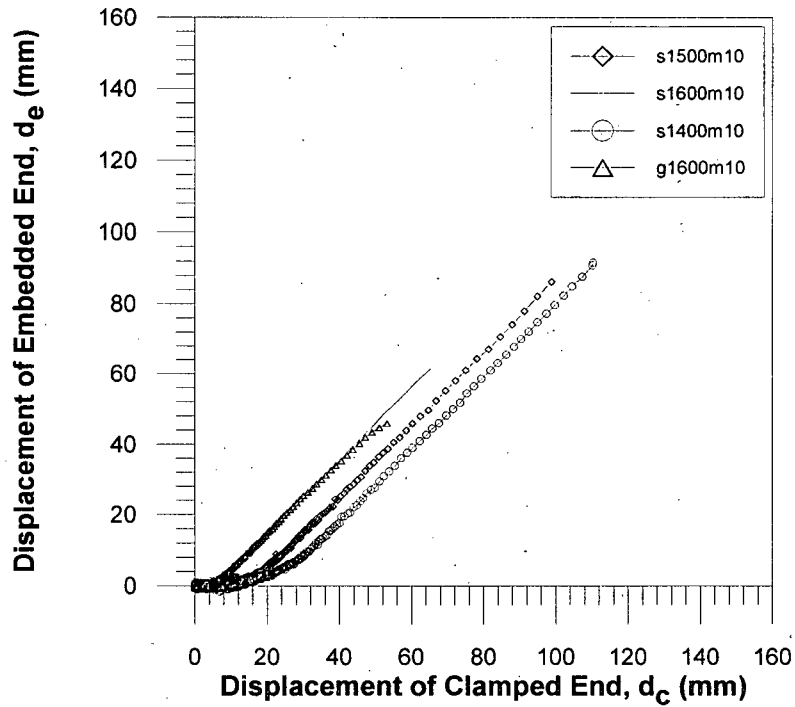
Figure 6.15: Displacement of embedded ends for all monotonic tests at
σ_v=10 kPa, showing the influence of geogrid stiffness and soil type
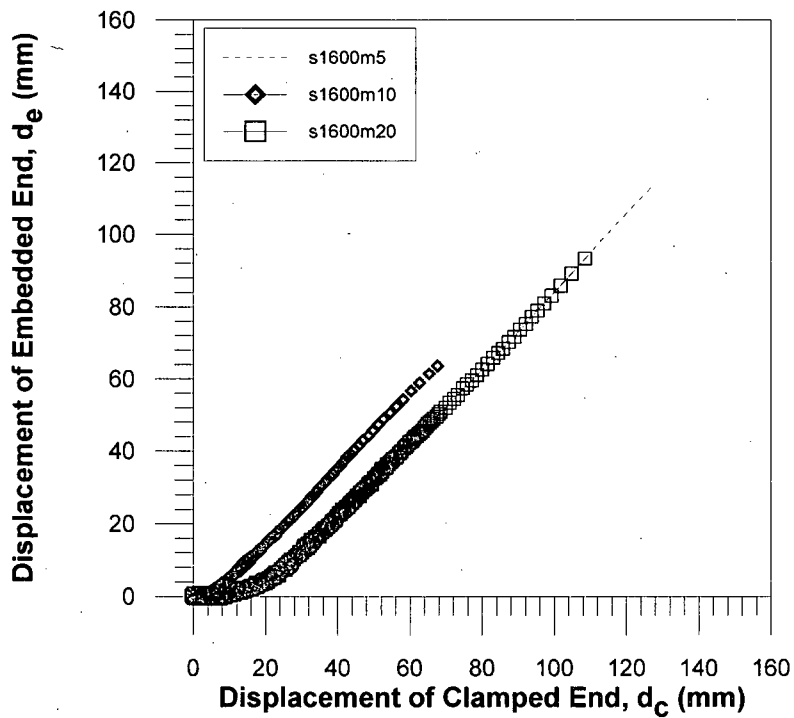
Figure 6.16: Embedded-end displacement for the UX1600HS tests in sand,
showing the influence of changes in nomal stress
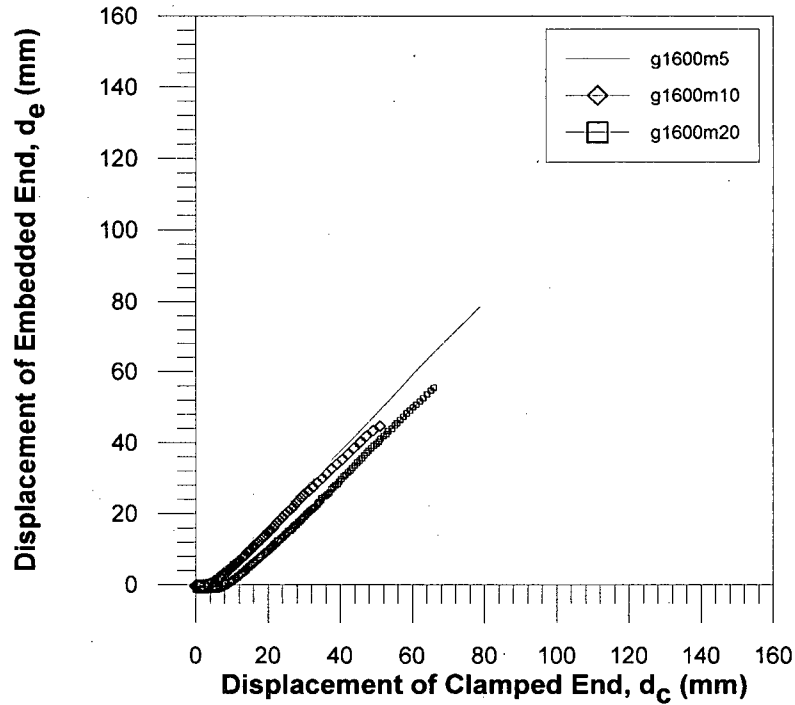
Figure 6.17: Embedded-end displacement for the UX1600HS geogrids in glass beads, showing the influence of normal stress
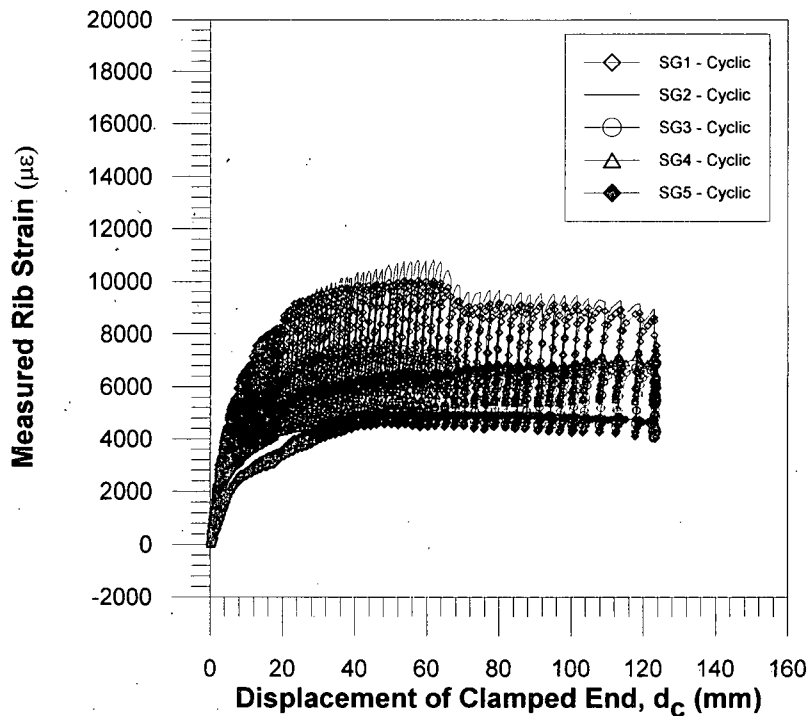
Figure 6.18: Mobilization of rib strain for the UX1500SB at σ_v=10 kPa in sand, using cyclic loading. 10000 $\mu\varepsilon$ = 1 percent strain.
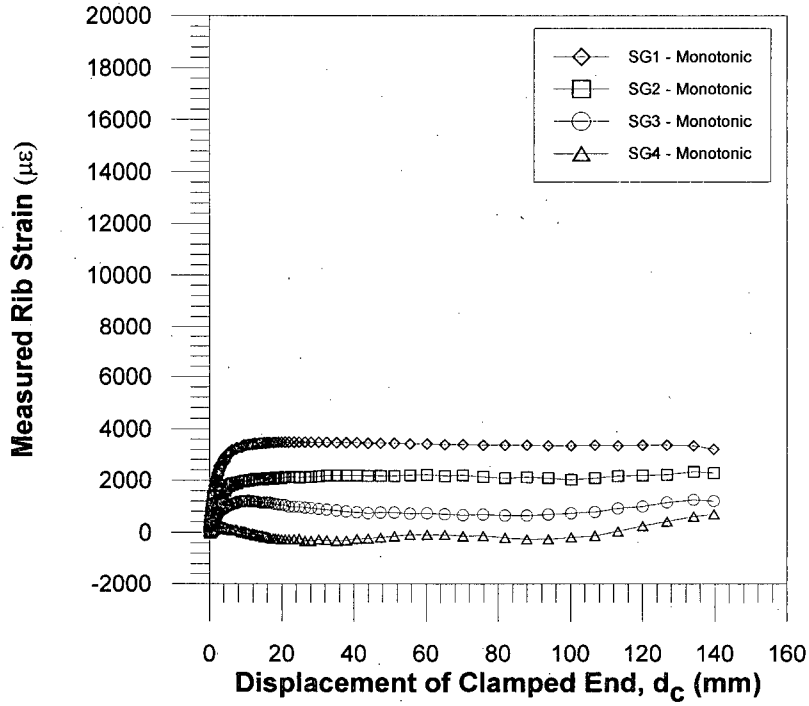
Figure 6.19: Mobilization of rib strain for the UX1600HS in sand under σ_v=5 kPa, using monontonic loading
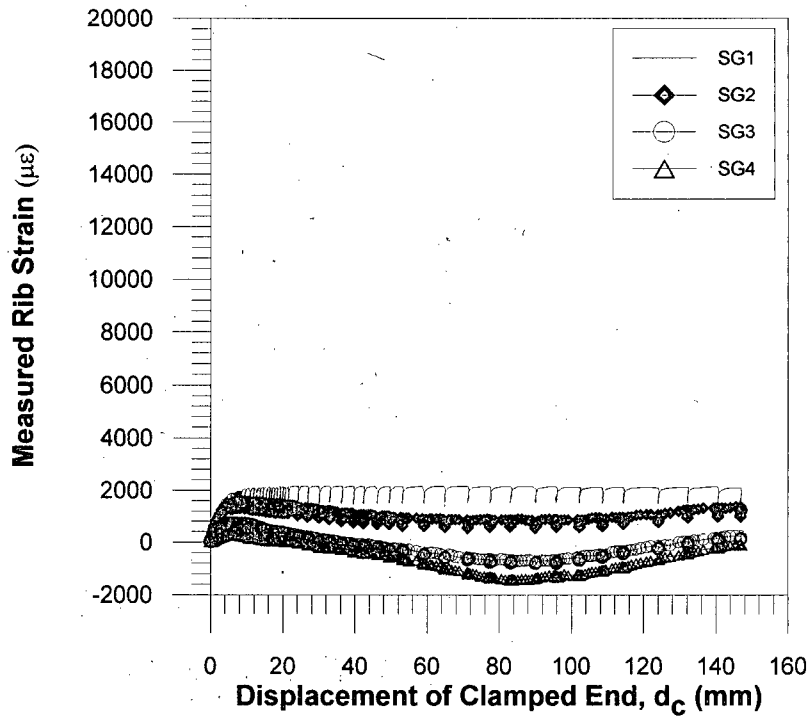
Figure 6.20: Mobilization of rib strain for the UX1600HS in sand under σ_v=5 kPa, using cyclic loading
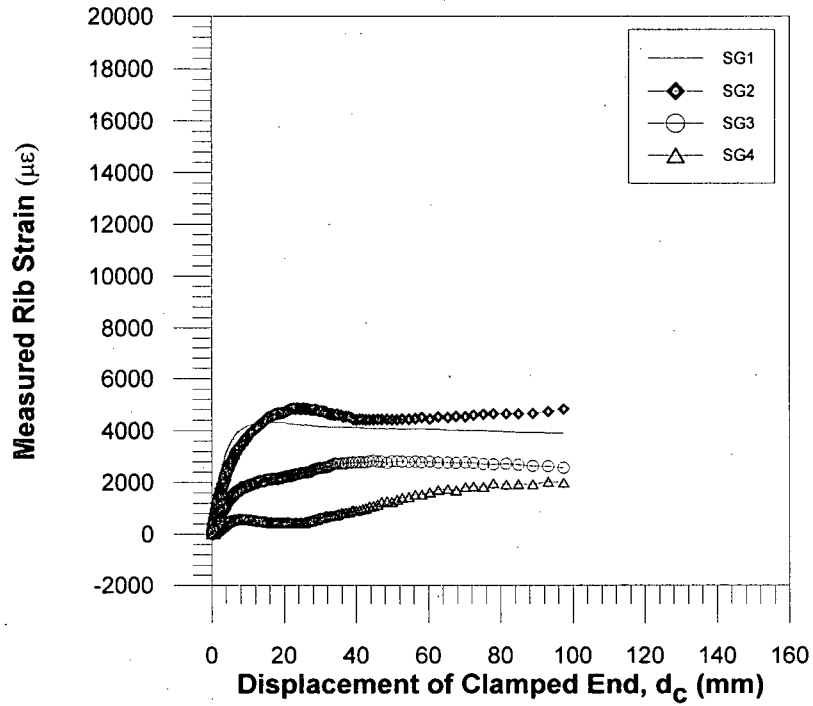
Figure 6.21: Mobilization of rib strain for the UX1600HS in sand under σ_v=10 kPa, using monotonic loading
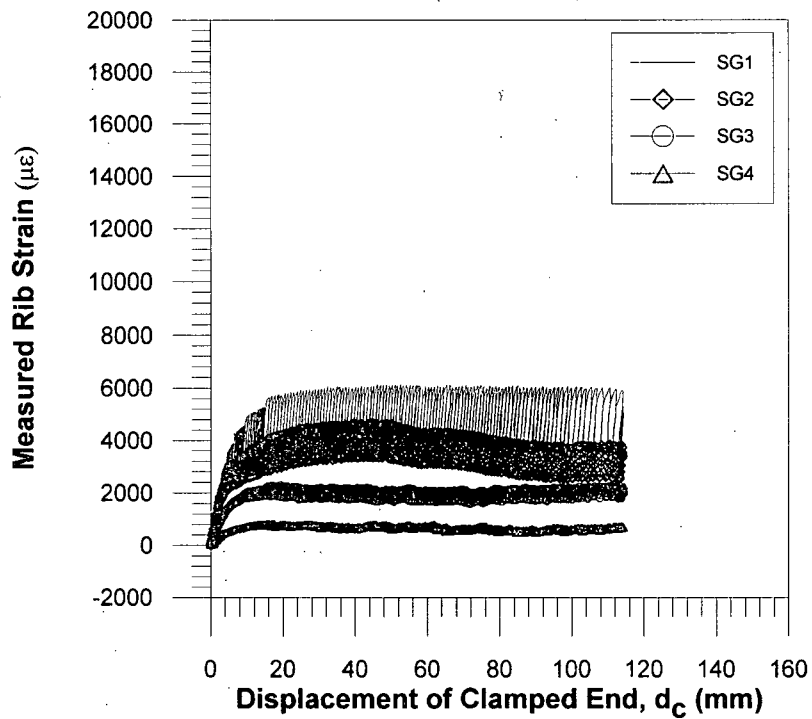
Figure 6.22: Mobilization of rib strain for the UX1600HS in sand under σ_v=10 kPa, using cyclic loading
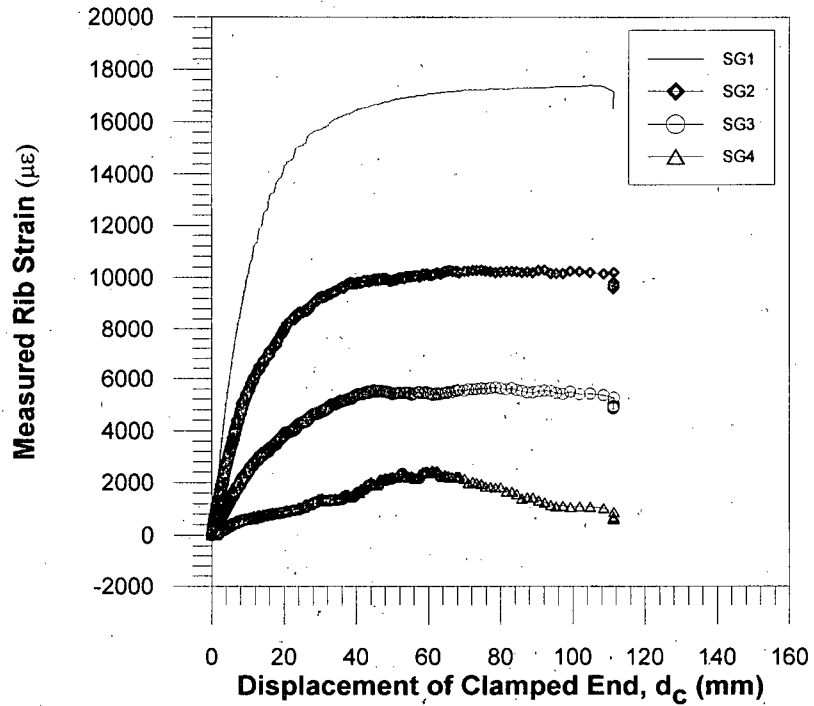
Figure 6.23: Mobilization of rib strain for the UX1600HS in sand under σ_v=20 kPa, using monotonic loading
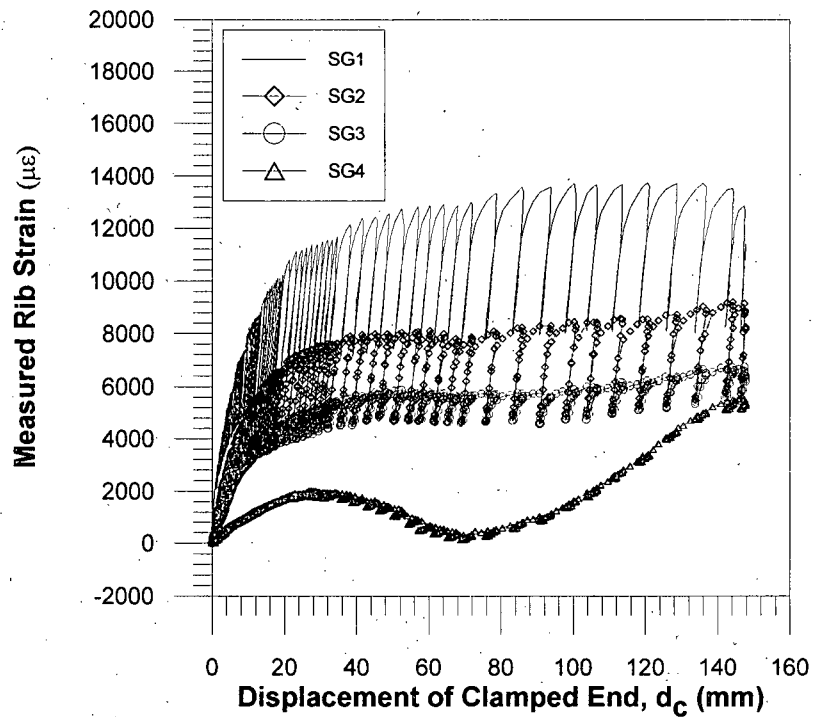
Figure 6.24: Mobilization of rib strain for the UX1600HS in sand under σ_v=20 kPa, using cyclic loading
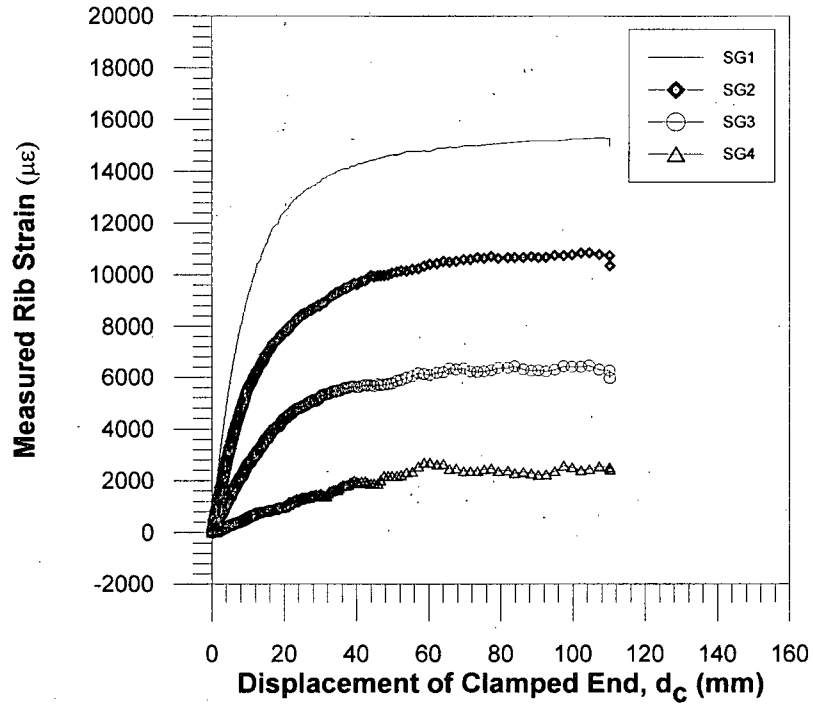
Figure 6.25: Mobilization of rib strain for the UX1400HS in sand under σ_v=10 kPa, using monotonic loading
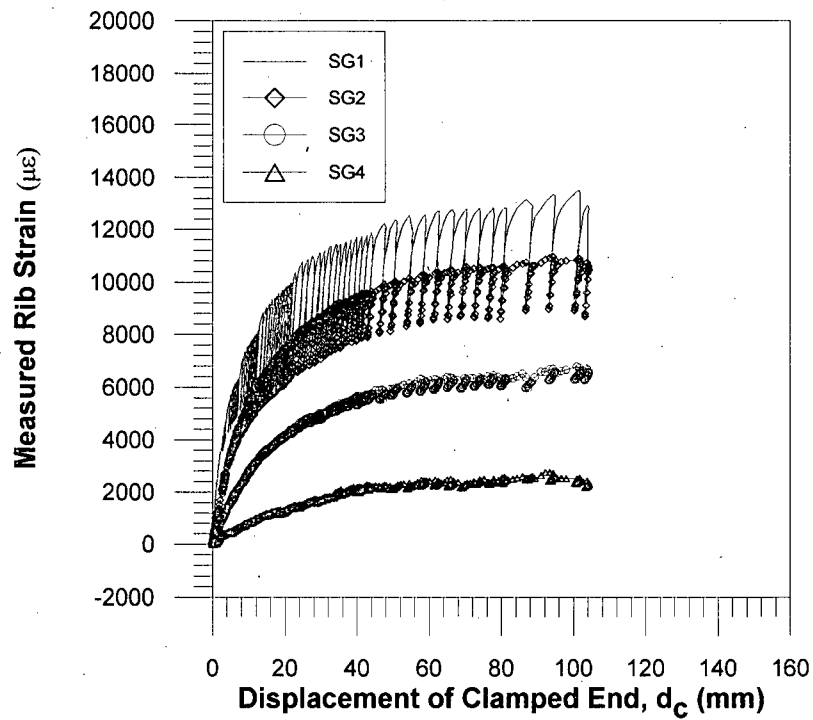
Figure 6.26: Mobilization of rib strain for the UX1400HS in sand under σ_v=20 kPa, using cyclic loading
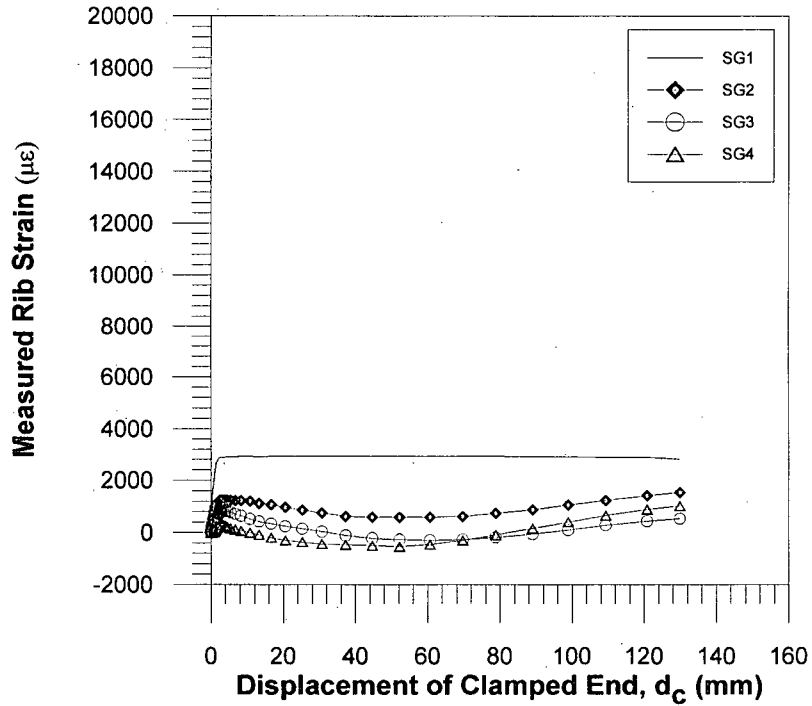
Figure 6.27: Mobilization of rib strain for the UX1600HS in glass beads under σ_v=5 kPa, using monotonic loading
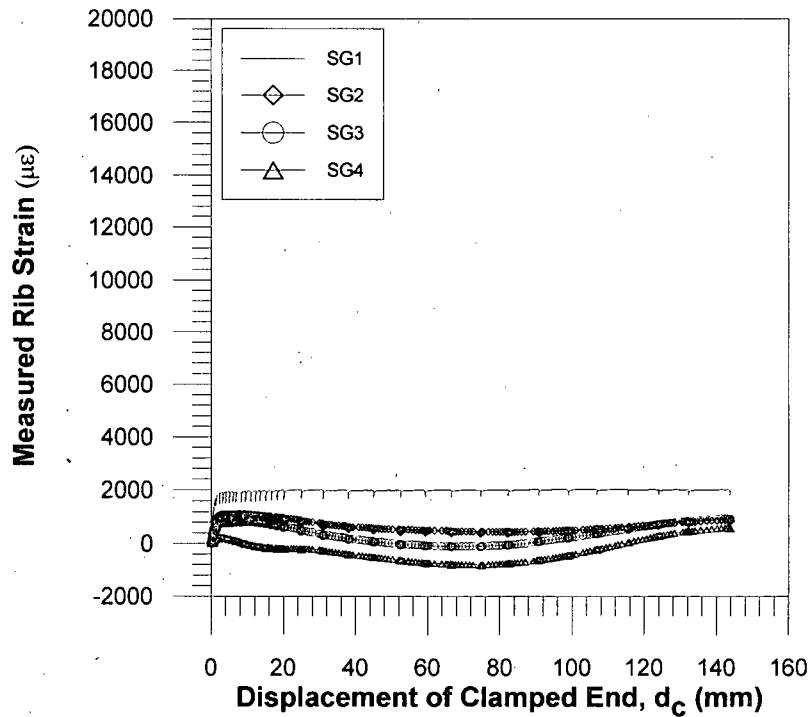
Figure 6.28: Mobilization of rib strain for the UX1600HS in glass beads under σ_v=5 kPa, using cyclic loading
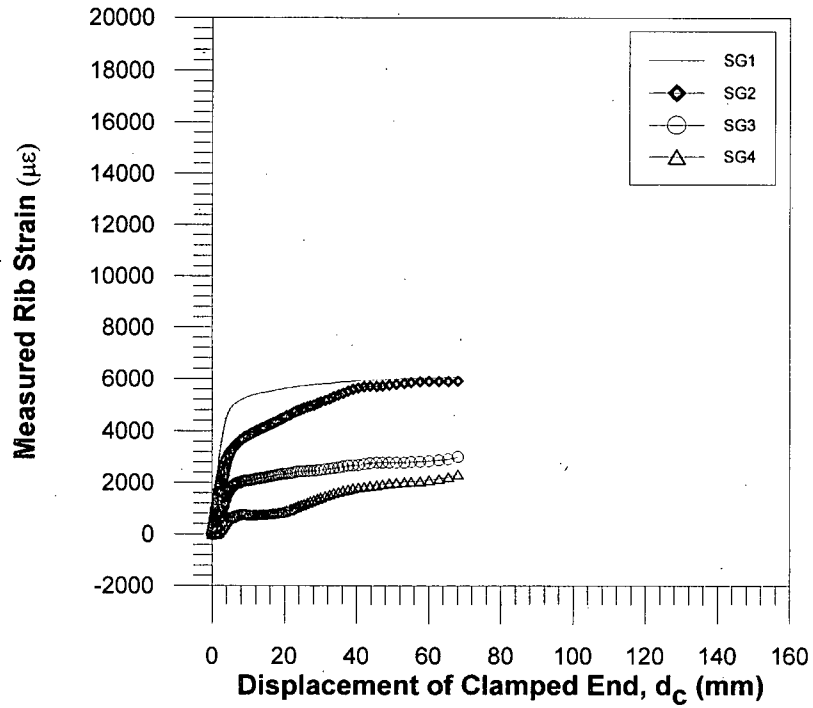
Figure 6.29: Mobilization of rib strain for the UX1600HS in the glass beads under σ_v=10 kPa, using monotonic loading
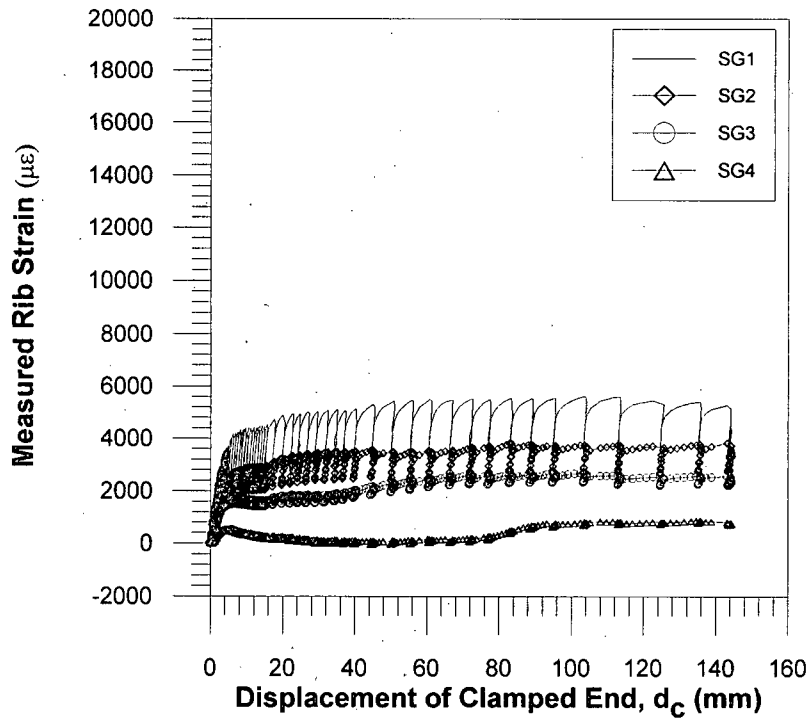
Figure 6.30: Mobilization of rib strain for the UX1600HS in the glass beads under σ_v=10 kPa, using cyclic loading
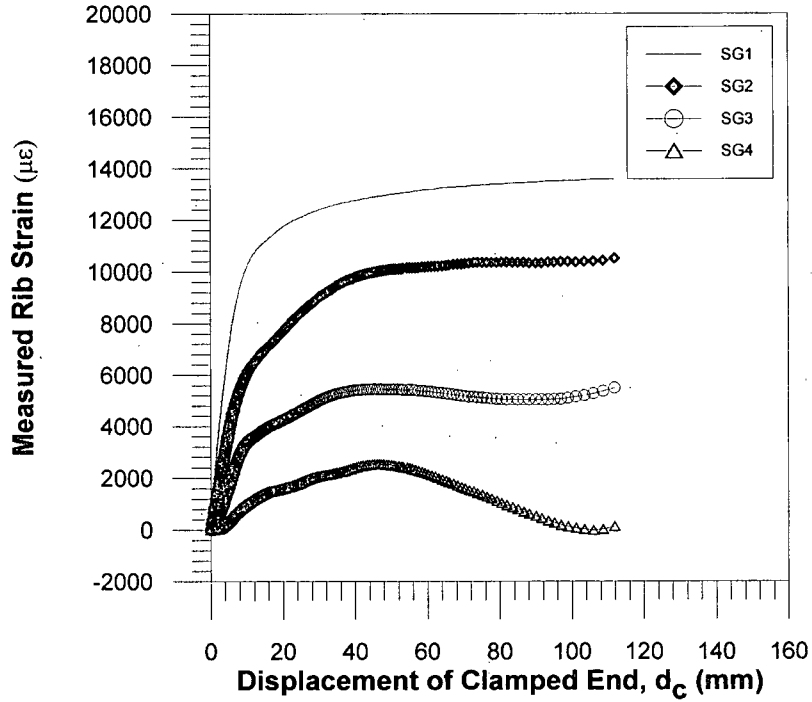
Figure 6.31: Mobilization of rib strain for the UX1600HS in glass beads under σ_v=20 kPa, using monotonic loading
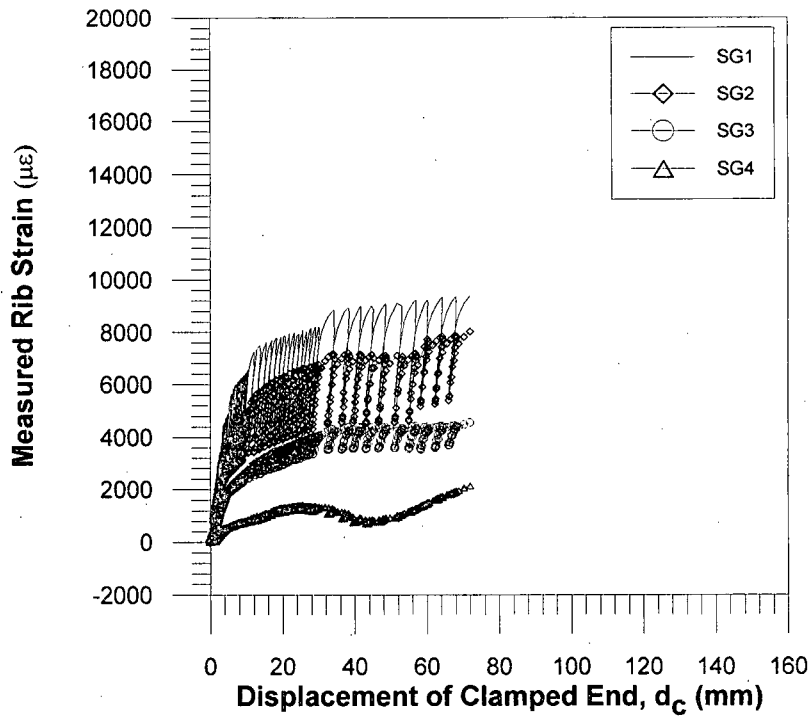
Figure 6.32: Mobilization of rib strain for the UX1600HS in glass beads under σ_v=20 kPa, using cyclic loading
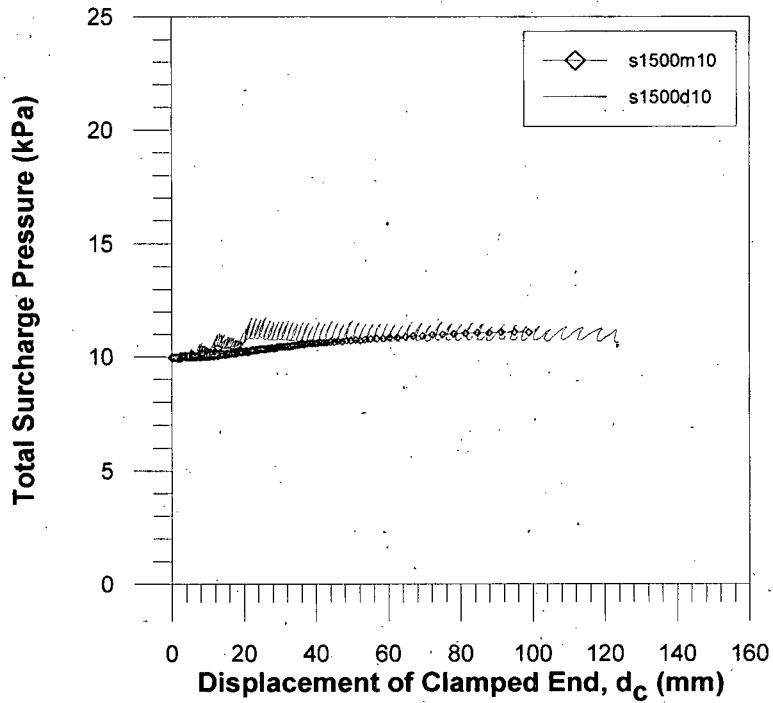
Figure 6.33: Measured normal stress for the UX1500SB in sand using both monotonic and cyclic loadings
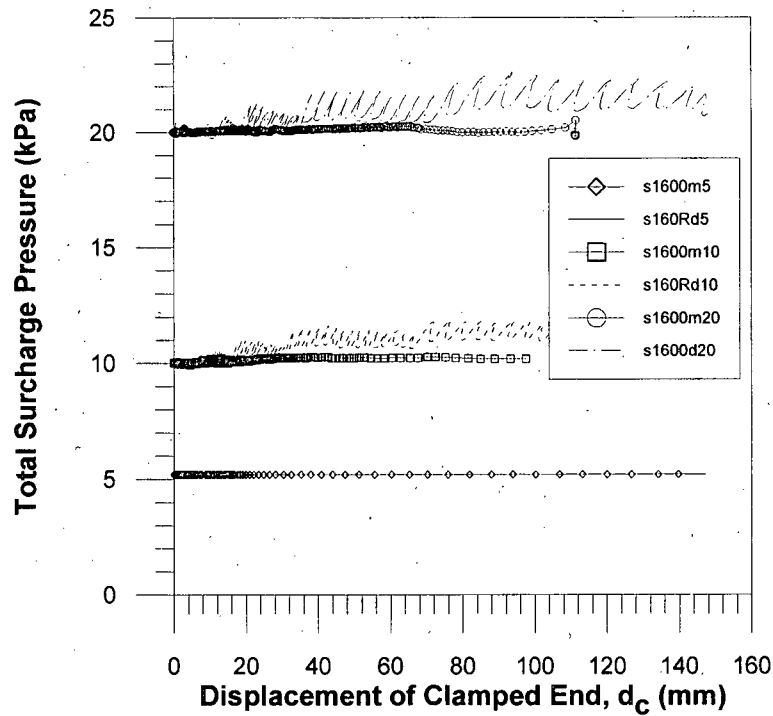
Figure 6.34: Measured normal stress for the UX1600HS in sand using both monotonic and cyclic loadings
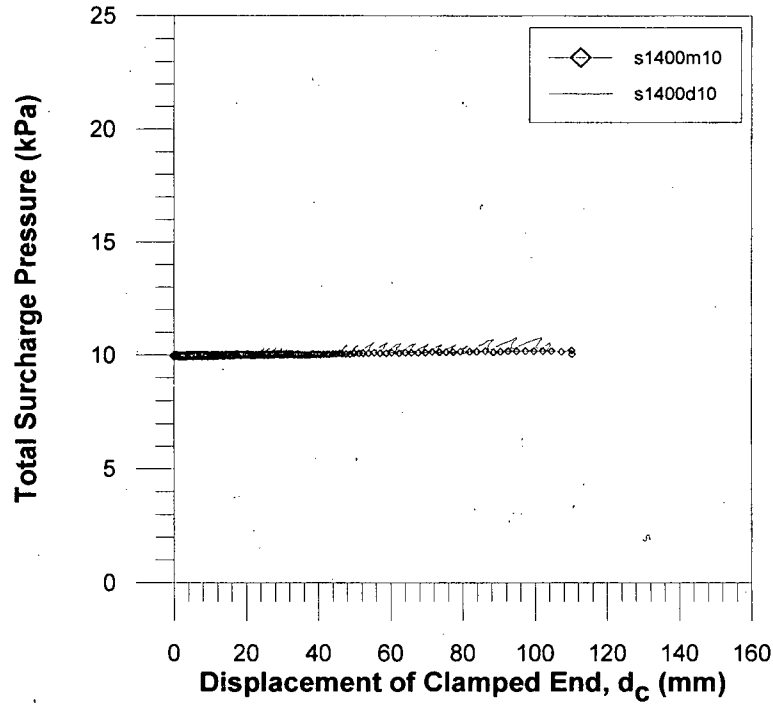
Figure 6.35: Measured normal stress for the UX1400HS in sand using both monotonic and cyclic loadings
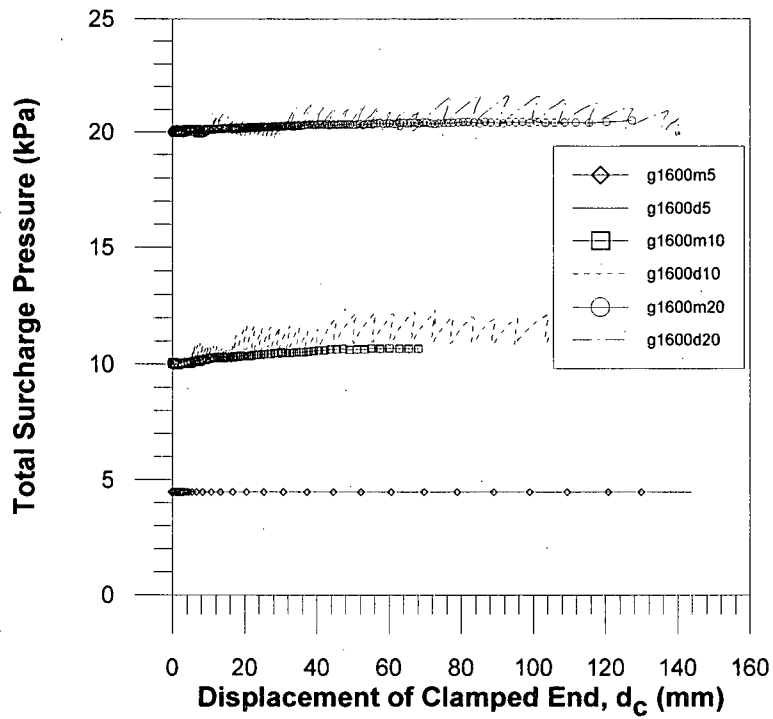
Figure 6.36: Measured normal stress for the UX1600HS in glass beads using both monotonic and cyclic loadings

CHAPTER 7

ANALYSES OF TEST RESULTS

7.1   Introduction

In the previous chapter, results of the testing program are reported together with comments on the apparent variations in pullout behavior of the soil/geogrid composites with surcharge pressures, soil materials, and grid materials. This chapter discusses the results of analyses performed on the generated data that will provide insight into the objectives posed at the beginning of this project. Specifically, interaction factors and coefficients of interaction for both monotonic and cyclic load-controlled tests were calculated; this chapter aims to address the interpretation of these coefficients, the challenges and assumptions made to generate them, and the implications the interpretations have on seismic design practice for geosynthetic-reinforced structures.

7.2   Interaction Factors and Coefficients of Interaction (Improved Total Area Method)

Factors for soil/geosynthetic interaction have been expressed in a number of ways, including $F^*\alpha$ (Christopher et al. 1990), $f_b\tan\delta$ (Jewell et al., 1984), $a'\tan\phi'_p$ (British Standards Institution, 1995), and $C_i\tan\phi$ (Simac et al., 1997), where F^* is a pullout resistance factor, α is a scale effect correction factor, f_b is a bond coefficient, δ is the angle of interface friction, a' is an interaction coefficient, ϕ'_p is the peak angle of soil friction, and C_i is a coefficient of shear stress interaction. The primary reason for establishing an interaction factor is to assess the pullout resistance of a geosynthetic embedded in soil.

For reporting purposes, interaction factors are given as a ratio of the shear stress (τ) to the applied surcharge pressure (σ). The shear stress was calculated from:

$$\tau = \frac{P}{2L_e W} \qquad [7.1]$$

where P is the measured pullout load, L_e is the instantaneous embedded length, and W is the specimen width. Because this measure is only valid when the entire geogrid specimen is moving

inextensibly (Stage III), this is referred to as the large-displacement interaction factor, $(\tau/\sigma)_{ld}$.
Figures 7.1 through 7.8 show the instantaneous interaction factors for each monontonic/cyclic test
pair ("instantaneous" is used to indicate values calculated during the test, and differentiate them
from a single test-specific or terminal value of interaction factor). It is cautioned that any data
appearing below the peak interaction factors in the cyclic tests are meaningless (but are included
for curve continuity) because the shear stress cannot be calculated from the measured load at any
point other than the cycle peaks (due to changes in length of the geogrid upon decrease of the
pullout load). Additionally, interaction factors appearing before Stage III are not representative
of the true mobilized interaction because the geogrids are still undergoing extension, which this
method of calculation cannot account for.

Inspection of these figures show that $(\tau/\sigma)_{ld}$ values for the cyclic tests lie very close to
their respective monotonic tests irrespective of normal stress level, soil material, or geogrid type.
A comparison of $(\tau/\sigma)_{ld}$ is given by geogrid type in Figure 7.9 and by surcharge pressures and soil
materials in Figure 7.10. Consistent with the comparison of pullout load by grid type in Section
6.3.1 and Figure 6.13, the 1500-series grid has the highest interaction with the embedding soil,
followed by the 1600 and 1400 series, in that order. It is again conjectured that the geometry and
distribution of transverse bearing bars account for this behavior. For the same grid series (1600),
the interaction factor is higher in the sand than in the glass beads, on the order of 30 to 50 percent.
The disparity in interaction factors is consistent with the disparity in pullout load for the
UX1600HS embedded in the two types of soil material; it is again proposed this disparity is due
to the differences in shear strength of the soil materials.

Figure 7.11 shows the results from one of Raju's displacement control (DC) – load
control cyclic (LC) test pairs (UX1500SB, 10 kPa surcharge, 0.1 Hz cyclic frequency), plotted
against test s1500m10. The interaction factors from s1500m10 compare well with the DC test,
suggesting that Raju's LC-DC test comparisons for interaction factors appear to be reasonable
despite the two types of loadings applied.

Because shear stress is related to a "coefficient of interaction", C_i, through the following
relationship:

$$\tau = C_i \cdot \sigma \tan \phi \qquad [7.2]$$

the interaction factor plots allow a direct calculation of the coefficient of interaction. Tabulated below in Table 7.1 are the coefficients and a ratio of the cyclic to monotonic coefficients, given as:

$$R_{ci} = \frac{(C_{i,c})_{60}}{(C_{i,m})_{60}}$$ [7.3]

where $(C_{i,c})_{60}$ is the cyclic coefficient of interaction at 60 mm displacement and $(C_{i,m})_{60}$ is the monotonic coefficient of interaction at the same displacement. The displacement was chosen based on a review of the interaction factor data to ensure that pullout was inextensible and that reliable data existed at that displacement for all tests. It will be noticed that for each test the coefficients are given twice, one using ϕ_p and the other using ϕ_{cv}, specific to each soil and the normal stress. These values of friction angles are taken from Figures 4.3 and 4.4.

Table 7.1—Coefficients of Interaction from Tensar Geogrid Pullout Tests, using the Improved Total Area Method (ITAM)

Test	$(C_{i,x})_{60}$ – Using ϕ_p	$(C_{i,x})_{60}$ – Using ϕ_{cv}	R_{ci} (ITAM)
s1500m10	0.9	1.1	
s1500d10	0.9	1.1	1.0
s1600m5	0.7	0.8	
s1600d5R	0.7	0.9	1.0
s1600m10	0.8	1.0	
s1600d10R	0.8	0.9	0.9
s1600m20	0.8	1.0	
s1600d20	0.8	1.0	1.0
s1400m10	0.6	0.7	
s1400d10	0.6	0.7	1.0
g1600m5	0.6	0.8	
g1600d5	0.6	0.8	1.0
g1600m10	0.7	0.8	
g1600d10	0.7	0.8	1.0
g1600m20	0.7	0.8	
g1600d20	0.7	0.8	1.1

It is immediately apparent from this table that R_{ci} is stable at approximately 1.0, suggesting that the geogrids' pullout behavior in this soil material under cyclic loading (e.g., earthquake) is as good as that under monotonic loading (e.g., service load).

Generally, $(C_{i,x})_{60}$ at large displacements for the UX1500SB is in the range of 1.1, the UX1600HS in the sand is approximately 0.9 and in the glass beads is approximately 0.8, and the UX1400HS in the sand is approximately 0.7. These coefficients are consistent with the findings in Figures 6.13 and 7.11.

7.3   Stability Under Cyclic Loading

Stability under a rapid loading (earthquake or blast) is a concern because of the higher load imposed for a short duration of time. A key consideration is the stability of the soil/geosynthetic composite when the rapid loading occurs. Will it fail rapidly or will it displace until enough resistance is mobilized?

Raju and Fannin (1997) proposed a method of comparing the stability of three manufacturers' grids under cyclic loading, which focused on the incremental displacement of each loading cycle applied. The underlying principle is that if the composite is stable, it will tend to decreasing incremental displacement with each subsequent cycle of loading. If the composite is unstable, the geosynthetic will either fail catastrophically in pullout or at the least tend to increasing incremental displacements with each loading. Figure 7.12 presents a stability graph from the Raju and Fannin paper (Tensar UX1500SB, $\sigma_v = 10$ kPa, f = 0.1 Hz).

Figures 7.13 to 7.20 show "stability curves" for each dynamic test. Each curve represents the loading cycles imposed at a given load ratio, which is defined here as the peak cyclic load against the peak monotonic load:

$$LR = \frac{P_w + \Delta P_N}{P_{P,m}}$$

[7.4]

where LR is the load ratio, P_w is the working load (3 kN/m in all tests), ΔP_N is the load increment applied (demand load) above the working load in the cyclic tests, and $P_{P,m}$ is the peak load measured in the corresponding monotonic test (see Figures 6.4 to 6.11). Incremental displacements (Δd_c) are measured from the onset of each series of load cycles (the same load ratio).

Because of the high frequency at which the cyclic loading took place, the peak load was maintained for a very short time before the load was dropped to below the peak monotonic load. As a result, catastrophic pullout did not occur in any of these tests, and discernment of "unstable" behavior from the stability curves generated from this study are more open to question (for an example, see Figure 7.15). However, it is clear that the pullout behavior of each grid remains stable to a load ratio of one or greater.

7.4   Strains in Cyclic Loading

Interpretation of pullout test results is fraught with its own set of difficulties if anything beyond a simple interaction factor at large displacements is required because of the polymeric nature of geosynthetics. Plastics are thermoviscoelastic/plastic materials that strain variably under differing conditions of temperature, strain rate, and loading history. Additionally, and more to the point for pullout tests, geosynthetics are extensible materials that yield a non-uniform stress distribution along the length of the grid as long as the grid continues to elongate. The stress distribution becomes uniform and constant once the grid has reached its extensible limit (Stage III, see Section 6.3.2) *provided* the geosynthetic has no bearing component that resists pullout; otherwise the stress distribution will become constant but remain non-uniform. Clearly, the latter is the case with the Tensar geogrids that derive a good deal of pullout resistance from the bearing areas on the transverse bars.

Because the principal objective of this research is to investigate the variation of interaction factors for geogrids undergoing both monotonic and cyclic pullout, the interest is focused primarily on large displacements. However, small-strain (progressive) pullout remains an important part of the development of the full pullout load. The challenge becomes, then, to properly account for the pullout resistance when the strain (and hence shear stress) along the length of the specimen is both non-uniform and dynamic. In this light, the following section takes a closer look at the strain data collected during tests.

7.4.1   Mobilization of Strain

Section 6.3.3 presents the rib strain data measured during pullout. Figures 6.18 through 6.32 show that the specimens strained progressively from the in-air end to the embedded end, and that the measured strains attenuated with distance from the clamped end. Consider test s1600m20

as given in Figure 7.21, which shows the variation of strain with increasing clamp displacement. The key features of this figure are that the strains are non-uniform along the length of the specimen even at large displacements and the strains reach a constant value (Stage III in Figure 6.25) at approximately 40 mm (with some variation).

Because of work by Perkins and Lapeyre (1997) and results generated by Raju (1995), the need for tests conducted to address differential strains in the geogrid along a rib from transverse bar to transverse bar became clear. Due to geometric variability in both plan and profile of the geogrids' ribs (see Figure 4.1), a strain gauge attached to a rib in one location may or may not represent the strain at another location or over the rib length as a whole. Perkins and Lapeyre refer to this phenomenon as "global versus measured" strains—global strains representing the strain over the length of the rib, from transverse bar to transverse bar. Hereinafter the measured strains will be referred to as "local" strains.

Two tests were conducted to address the local/global strain issue. After removing the soil material from test s1600d5R to expose the UX1600HS grid, the free end was clamped to the back of the pullout box then subjected to a modified cyclic test routine (monotonic loading to $P_w = 2$ kN/m at $r_1 = 0.25$ kN/m/min, then cyclic loading at $f = 0.5$ Hz and $\Delta P_N = 0.75$ kN/m). Similarly, the UX1400HS grid from test s1400m10 was uncovered, clamped to the back of the pullout box, and subjected to the same cyclic test routine. Loads, clamp displacements, and local rib strains were measured. Figures 7.22 through 7.26 document the results of the two tests.

Figures 7.22 and 7.23 show the strain data from the UX1600HS and UX1400HS tests, respectively, plotted against time. Readily apparent from the Figure 7.22 is the separation of SG1 data from the other gauges' data. This indicates that the location of the strain gauge along the rib can make a significant difference to the measurements that are taken, if there are significant geometric variations in the rib. This is the case for the UX1600HS grid, but much less so for the UX1400HS, shown in Figure 7.23.

The load-strain relationship for SG2 during the UX1600HS test is given in Figure 7.24. The load-strain relationship is initially linear until the cyclic loading begins. At this point, the relationship becomes stiffer due to an increase in clamp displacement rate, and the strain signatures form hyperbolic unload-reload loops that follow a plastic hyperbolic load-strain envelope (shown as a dashed line). Each set of load-unload cycles becomes increasingly less stiff

(flatter) as the displacement rate increases to meet the demand load at the given frequency. This suggests that the geogrid stress-strain behavior is non-linear (approximated very well by a hyperbolic relationship, as found by Cai and Bathurst, 1995) and that plastic strains occur at a very low strain level (on the order of 0.25 percent). As will be shown later, this makes calculation of the interaction factor very difficult at anywhere other than the loading peaks during the cyclic stage of the tests.

To compare local and global strains, the displacement measured at the clamped end was rendered into a global strain for each of the four rib sections that were strain-gauged (a rib section is defined as the centerline of one transverse bar to the next, see Figure 4.1), using the following relationship:

$$\varepsilon_{g,x} = \frac{d_c}{nL_0} \qquad [7.5]$$

where $e_{g,x}$ is the global strain for the "x"th rib, d_c is the clamp displacement, n is the number of rib sections along the length of the geogrid (in this case, n = 4), and L_0 is the unstrained geogrid length. The ratio of the global to local strain was then plotted against the measured local rib strain for each of the strain gauges; one example is shown for each grid series (1400 and 1600) in Figures 7.25 and 7.26. Although it cannot be seen well in the figures, the curves incorporate load-unload cycles; it appears the global-local strain ratio is unaffected by any plastic strains that occur during the load portion of the cycles. Both curves follow a distinctive and clear pattern, implying any analysis done with the strain data should be corrected for the true strain over a longer gauge length than represented by the strain gauge.

In summary, the strain gauge data appear to suggest six behaviors of the geogrid:

- while embedded in soil, an applied load mobilizes strain in the grid progressively;
- if there are bearing surfaces on the grid, the strains will not become uniform over the surface of the grid;
- strains may not be uniform along the length of one rib in Tensar's geogrids due to geometric variations;

- strains registered locally may not represent the "global strain" along the length of one rib section;

- Tensar geogrid load-strain behavior is non-linear and can be represented by a hyperbolic function, consistent with the findings of Cai and Bathurst (1995); and

- plastic strains occur at very low strains, consistent with the findings of Moraci and Montanelli (1996).

7.4.2 A Method for Determination of Interaction Factors from Strain Data

In an attempt to deduce interaction factors at small displacements in pullout tests, Raju (1995) proposed a "Generalized Method" for the determination of interaction factors to account for geosynthetic extensibility and progressive mobilization of pullout resistance. It was used with minor modifications in this testing program, and is described briefly below.

The Generalized Method uses local strain measurements to describe the progressive pullout displacement of the geogrid and hence the stress distribution on the surface. From the calculated stress distribution, interaction factors and coefficients of interaction can be computed. This is accomplished in the following steps.

7.4.2.1 Step 1—Determination of Instantaneous Strain Profile and Related Displacement

Using software written in QBasic, local strains were first converted to global strains using the relations shown in Figures 7.25 and 7.26, then used to generate a "strain distribution" as a fifth-order polynomial function. It was assumed that the strain was uniform over the exposed portion of the specimen, so the total function was a discontinuous linear/fifth-order polynomial. Using Simpson's Rule for approximate integration the cumulative strain over the entire length of the geogrid was calculated, then computed as an elongation. The QBasic program then compared the measured clamped-end displacement to the calculated elongation; any deficit in elongation was assigned to the embedded end as displacement.

The calculated embedded-end displacements were compared to the measured embedded-end displacements to give an idea of the resolution and accuracy with which the measured strains could describe the overall pullout behavior. Figures 7.27 and 7.28 show the best and worst matches, giving an idea of the range of accuracy that can be expected using this method.

Calculated results from the previous study (Raju, 1995) provide better matches to the measured data than in this program due to a closer spacing of strain gauges.

7.4.2.2 Step 2—Determination of Stress Profile and Average Stress

Measured strain data were processed by another QBasic program that converted them to equivalent SG1 measurements (SG1 was mounted closer to the transverse bar, compare Figures 3.6 and 7.22). Then, using the load-strain relationships established from Figures 7.29, 7.30, and 7.31, the strains were rendered into loads. Using the same procedure for the strains above, a force distribution was calculated by fitting a fifth order polynomial through the force data for the embedded portion of the specimen. Using Simpson's Rule, the total force on the geogrid was calculated from the calculated force distribution (area under the curve) and compared with the measured load; an example of this is shown in Figure 7.32. A few quick calculations from the previous study's results (Raju, 1995) shows the same disparity between measured and calculated forces.

Individual stresses as small increments were then calculated using the force profile found above. To find the average stress, Simpson's Rule was once again applied to find the total stress acting over the instantaneous embedded length of the specimen, which was then divided by the instantaneous embedded length.

7.4.2.3 Step 3—Calculation of Interaction Factors and Coefficients of Interaction

Calculation of interaction factors and coefficients of interaction was exactly as described above in section 7.2. Plots of interaction factors versus clamped-end displacement are given in Figures 7.33 to 7.39. Coefficients of interaction and R_{ci} calculated from the Generalized Method are given for the tests in Table 7.2. For comparison, values of R_{ci} calculated from the Improved Total Area Method are shown as well.

Table 7.2—Coefficients of Interaction from Tensar Geogrid Pullout Tests, using the Generalized Method (GM)

| Test	$(C_{i,x})_{60}$ – Using ϕ_p	$(C_{i,x})_{60}$ – Using ϕ_{cv}	R_{ci} (GM)	R_{ci} (ITAM)
s1600m5	0.7	0.9	1.2	1.0
s1600d5R	0.8	1.0		
s1600m10	0.6	0.7	1.1	0.9
s1600d10R	0.7	0.8		
s1600m20	0.7	0.9	0.9	1.0
s1600d20	0.7	0.8		
s1400m10	0.5	0.6	1.1	1.0
s1400d10	0.5	0.6		
g1600m5	0.7	0.9	1.0	1.0
g1600d5	0.6	0.8		
g1600m10	0.4	0.5	1.3	1.0
g1600d10	0.6	0.7		
g1600m20	0.5	0.6	1.1	1.1
g1600d20	0.6	0.7		

7.4.2.4 A Critique of the Generalized Method

Consideration of the previous plots and values of C_i implies use of the Generalized Method should be done with caution and a knowledge of the limitations. First, it is highly dependent upon the quality and quantity of strain gauges present in order to describe a reasonable strain distribution. A polynomial strain distribution cannot approximate the true strain profile along the length of a Tensar geogrid due to the variety of geometrical variations present. Second, the calculated force should match the measured force as a check of the model. Using this method, calculated loads were only approximately 70 percent of the measured loads in both this testing program and Raju's study. Third, at large displacement the interaction factors should match those calculated by the Improved Total Area Method. This is again not the case; however, the values of R_{ci} calculated by the Generalized Method are only generally slightly higher than the corresponding values calculated by the Improved Total Area Method.

7.5   Pullout Testing Analyses Summary

Analyses performed on the pullout tests in this study suggest the following:

1. At the given surcharge levels, the coefficients of interaction for Tensar uniaxial geogrids are virtually the same for monotonic and cyclic loading, independent of the grid series, soil material in which they are embedded, and normal stress level;

2. the Tensar uniaxial geogrids appear to remain stable (i.e., resist catastrophic pullout) under cyclic loading to load levels at or above the static (monotonic) loads the grids are capable of sustaining;

3. plastic geogrids strain progressively from the point of load application to the back end, whereupon the grids behave inextensibly;

4. Tensar uniaxial geogrids derive a good deal of pullout resistance from transverse bearing members, which results in a non-uniform but constant strain distribution at large displacements;

5. because of geometric variations along the length of a rib, the strain measured at one location may not represent the strain at another location or over the rib length as a whole; and

6. the Generalized Method, used to determine interaction factors at small displacements, should be used with caution, mostly with respect to the quantity of strain measurements available to describe the strain profile over the length of the geogrid specimen.
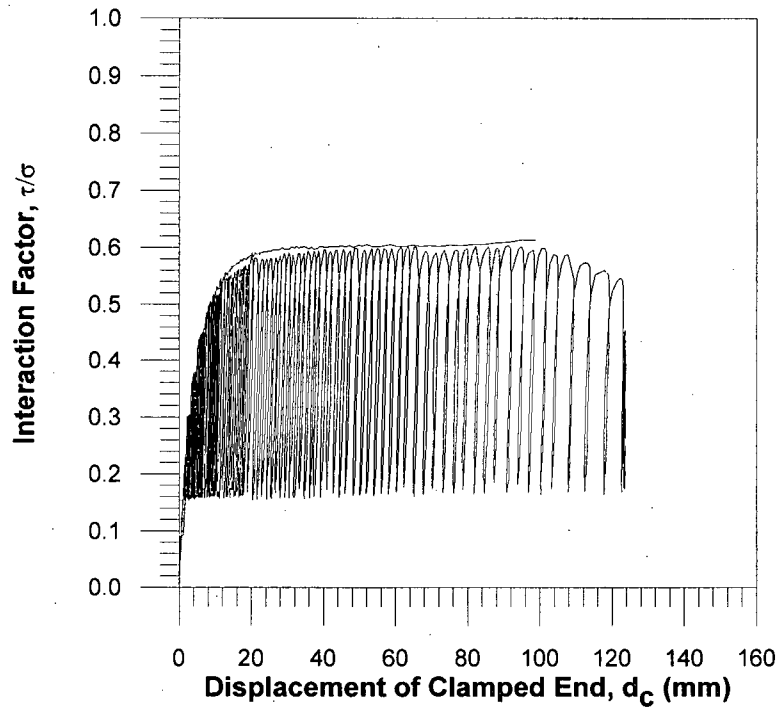
Figure 7.1: Interaction factors for the UX1500SB monotonic and cyclic tests
in sand under σ_v=10 kPa
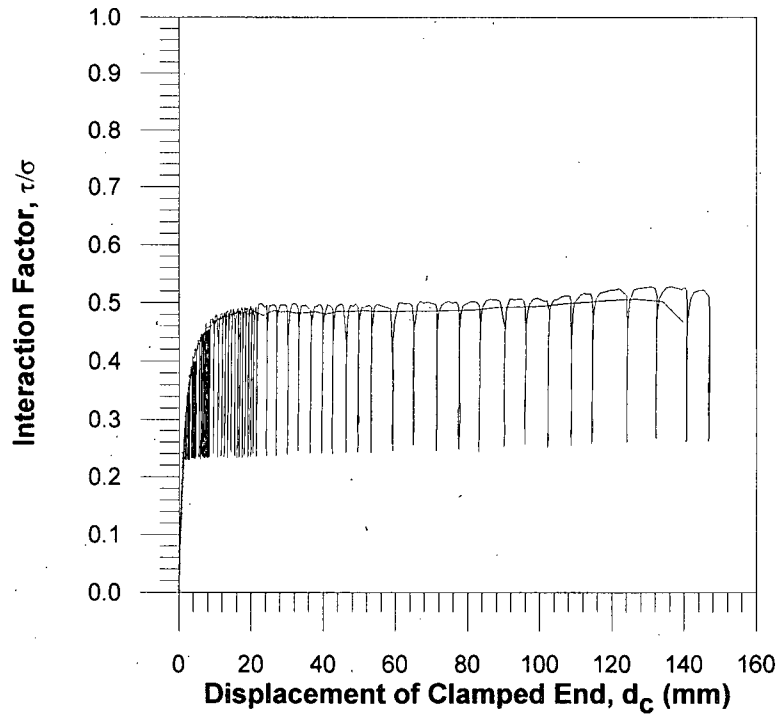
Figure 7.2: Interaction factors for the UX1600HS monotonic and cyclic tests
in sand under σ_v=5 kPa
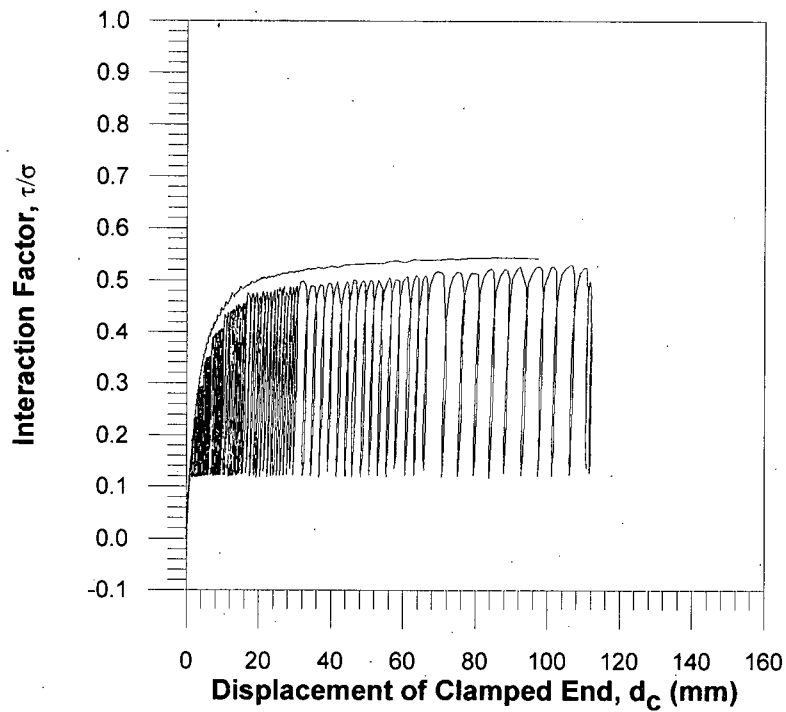
Figure 7.3: Interaction factors for the UX1600HS monotonic and cyclic tests in sand under σ_v=10 kPa
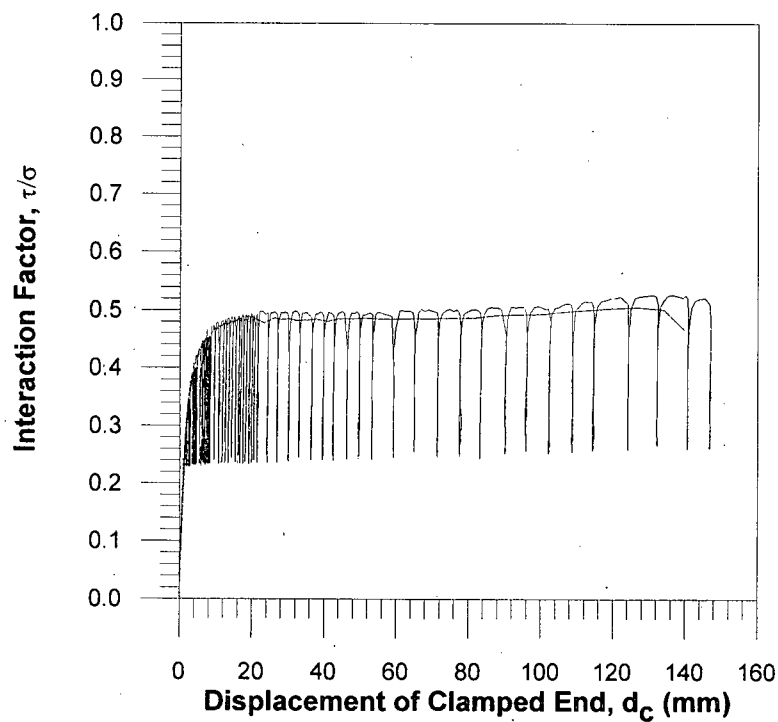
Figure 7.4: Interaction factors for the UX1600HS monotonic and cyclic tests in sand under σ_v=20 kPa
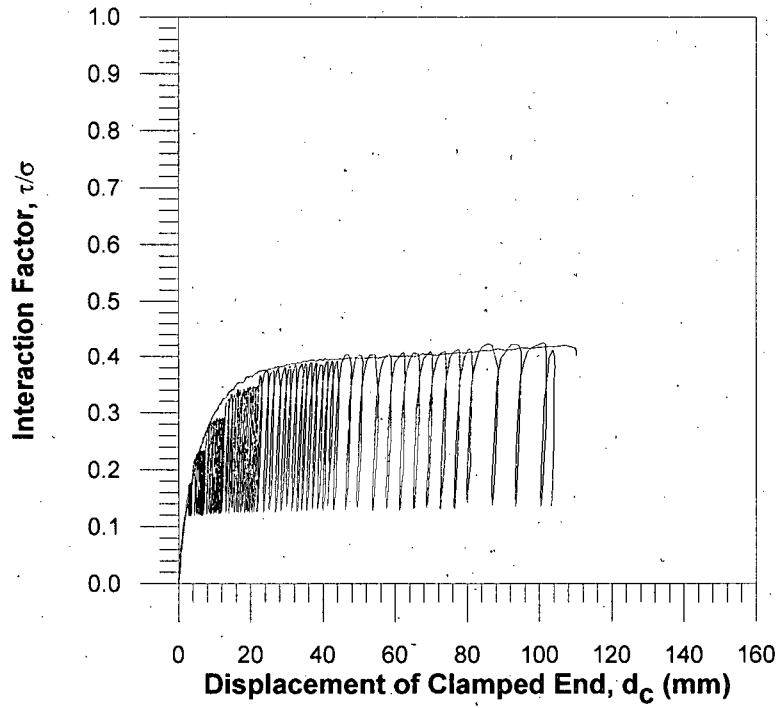
Figure 7.5: Interaction factors for the UX1400HS monotonic and cyclic tests in sand under σ_v=10 kPa
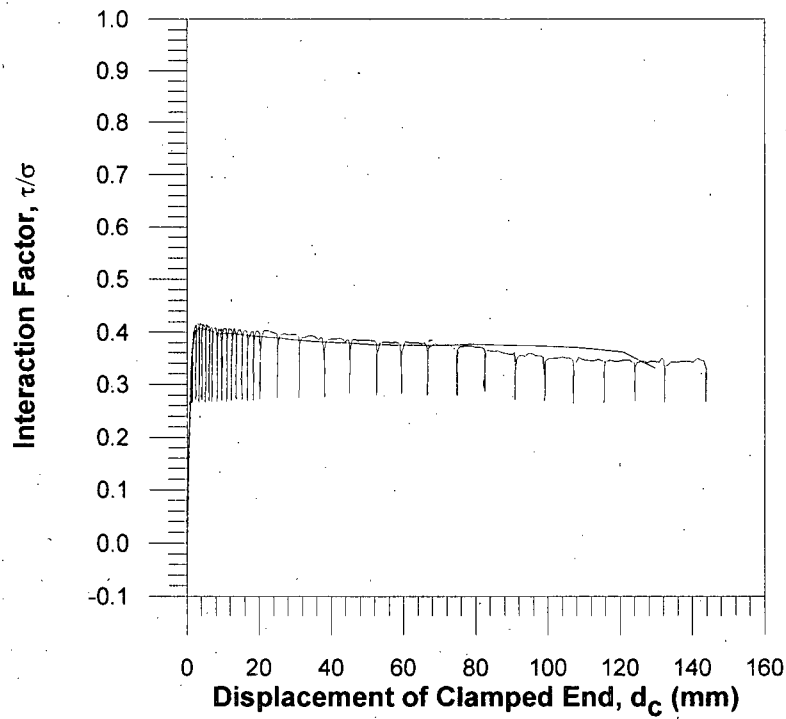
Figure 7.6: Interaction factors for the UX1600HS monotonic and cyclic tests in glass beads under σ_v=5 kPa
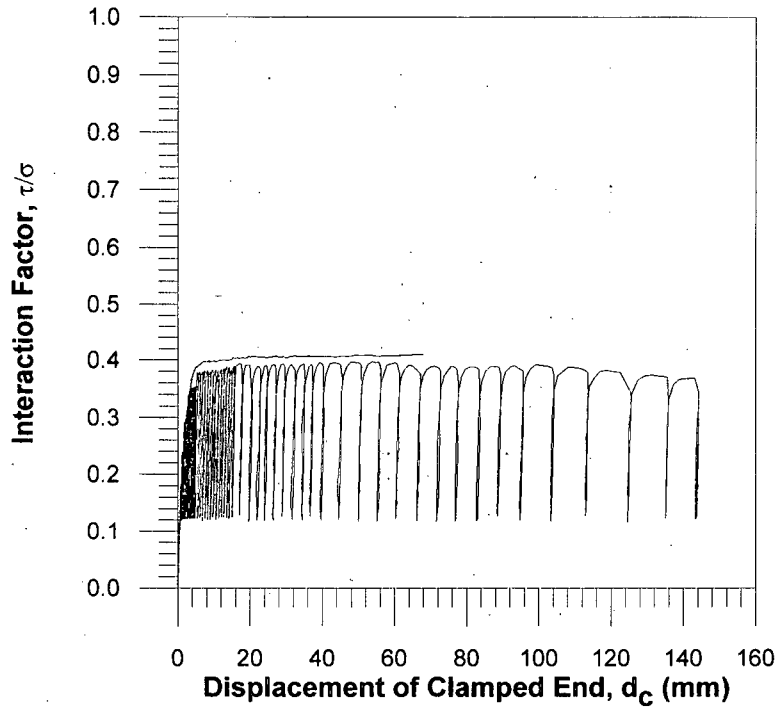
Figure 7.7: Interaction factors for the UX1600HS monotonic and cyclic tests in glass beads under σ_v=10 kPa
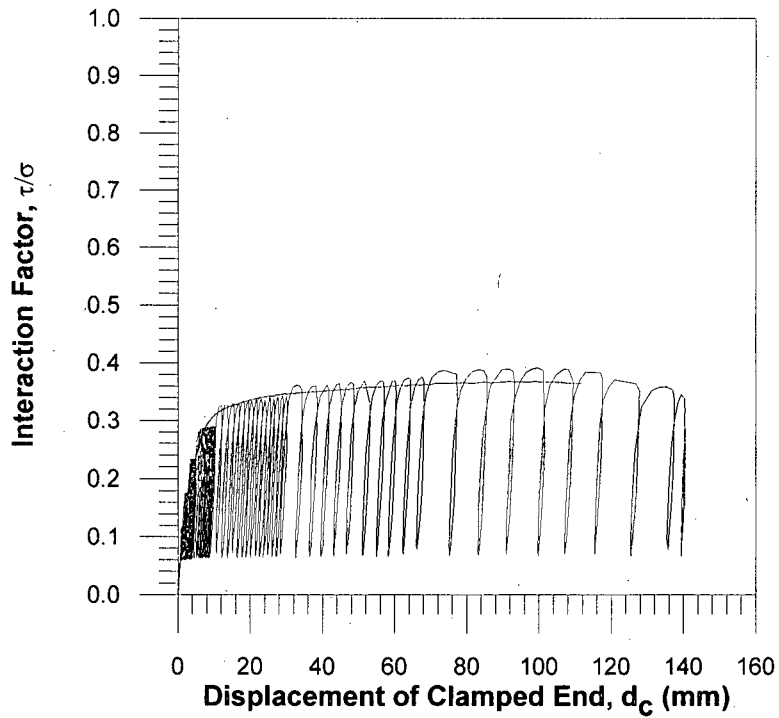
Figure 7.8: Interaction factors for the UX1600HS monotonic and cyclic tests in glass beads under σ_v=20 kPa
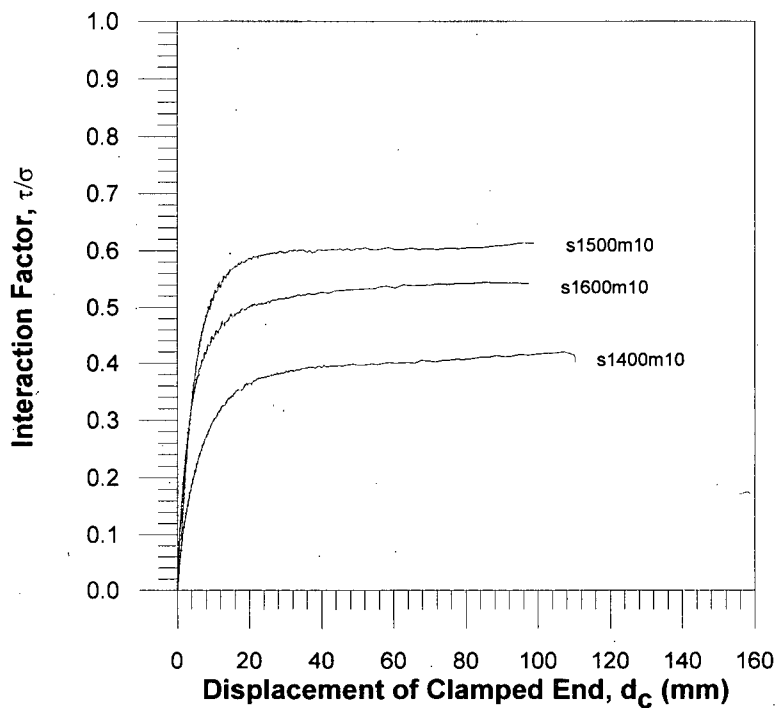
Figure 7.9: A comparison of interaction factors for each geogrid series in sand under σ_v=10 kPa
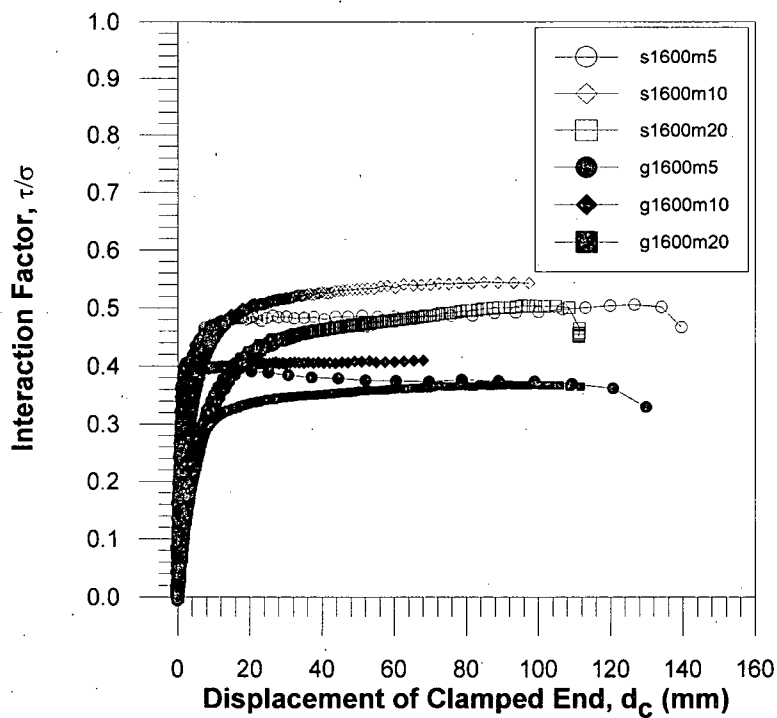
Figure 7.10: A comparison of interaction factors for the UX1600HS by soil material and normal stress
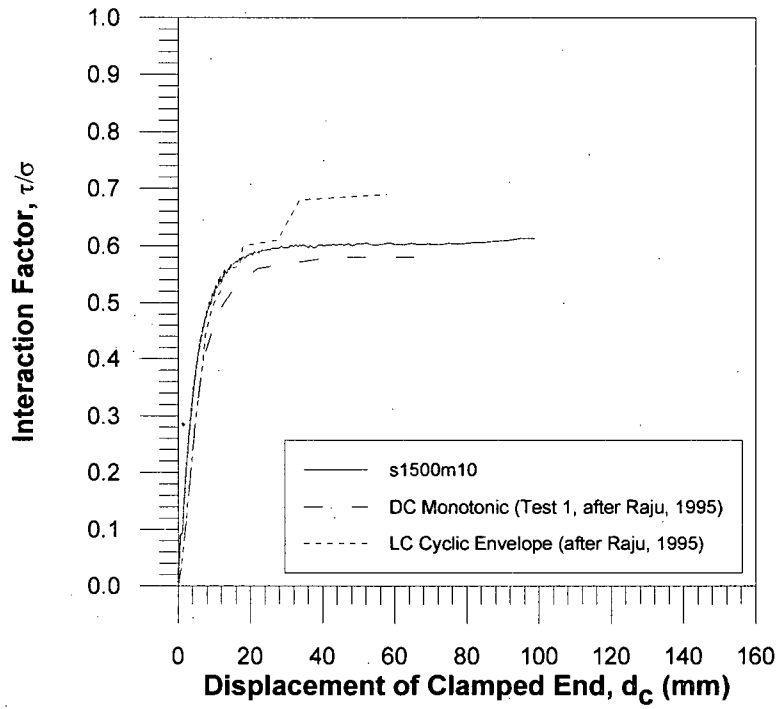
Figure 7.11: A comparison of interaction factors from a displacement-controlled monotonic test, s1500m10, and a load-controlled cyclic test (after Raju, 1995)
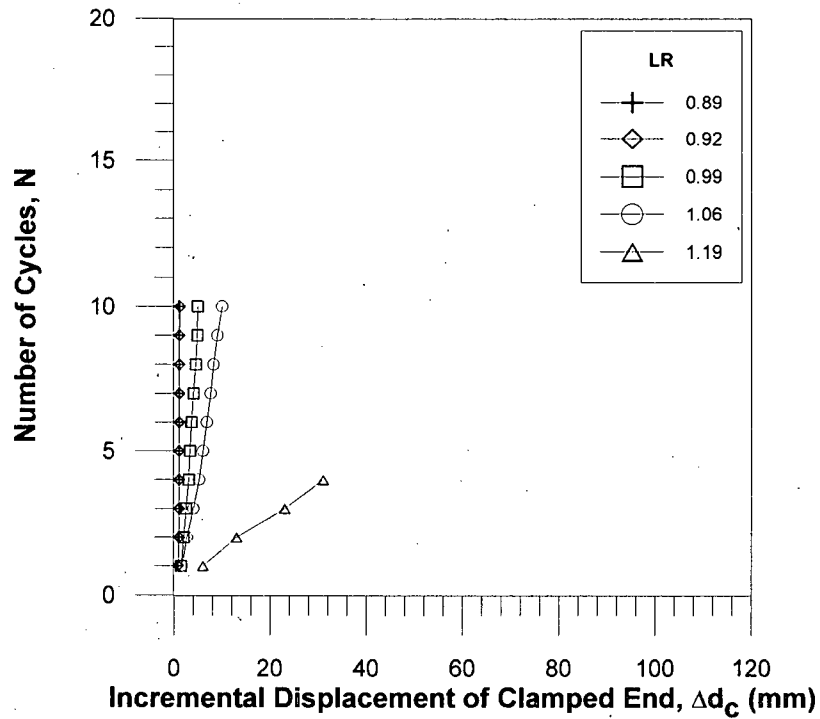
Figure 7.12: Stability curves for a UX1500SB cyclic test in sand under $\sigma_v=10$ kPa, f=0.1 Hz (after Raju, 1995)
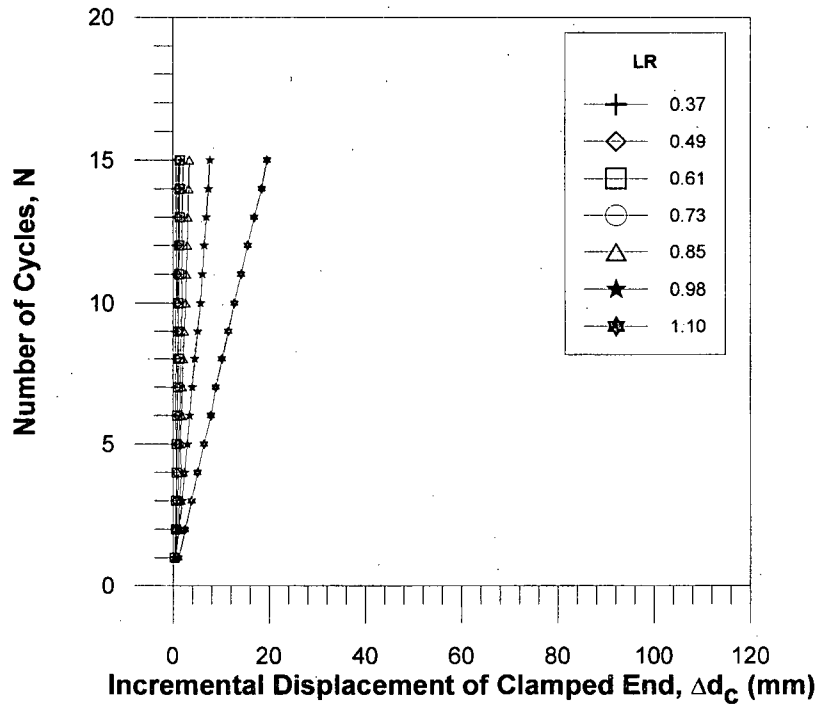
Figure 7.13: Stability curves for a UX1500SB cyclic test in sand under σ_v=10 kPa, f=0.5 Hz
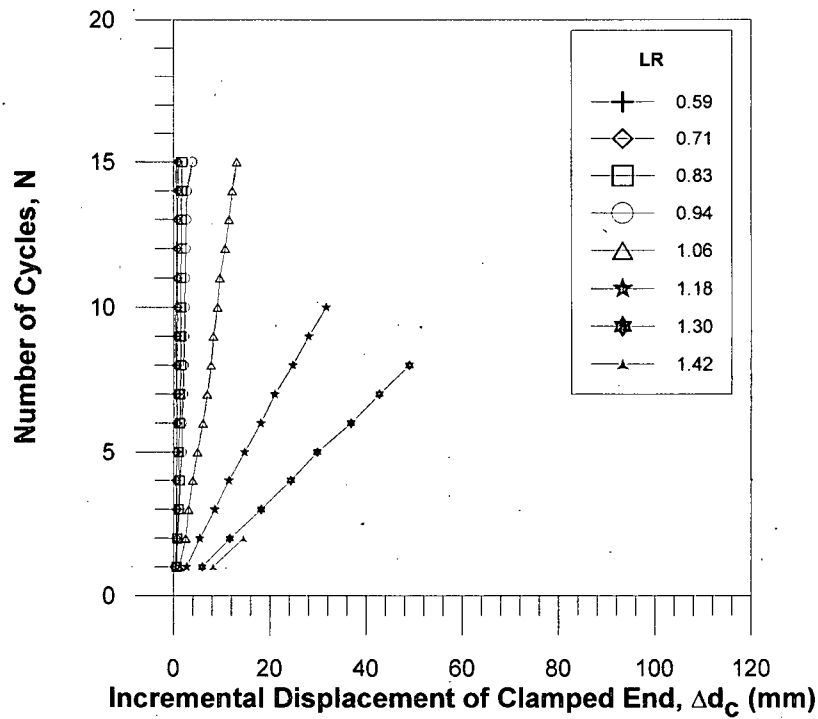
Figure 7.14: Stability curves for a UX1600HS cyclic test in sand under σ_v=5 kPa, f=0.5 Hz
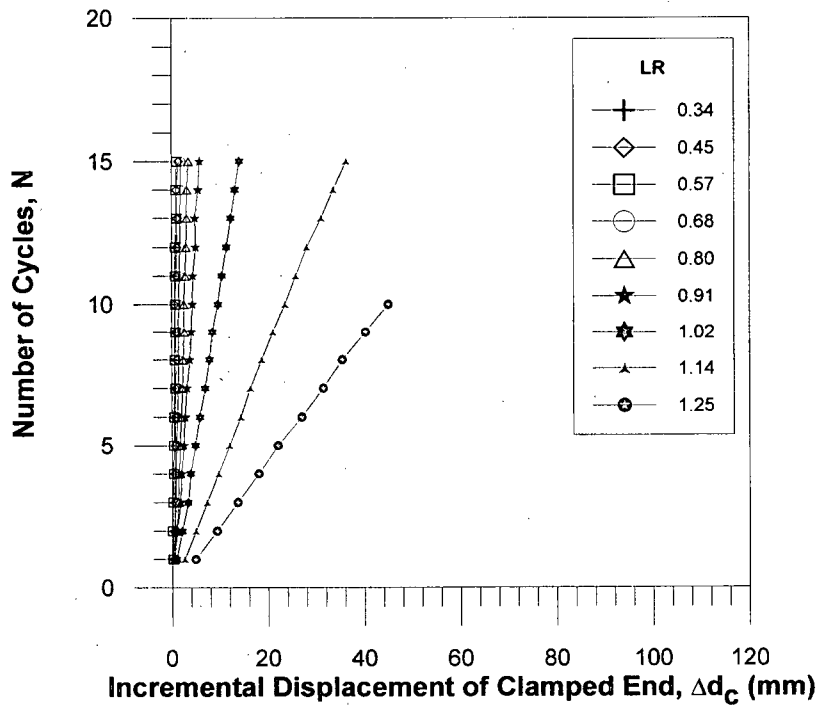
Figure 7.15: Stability curves for a UX1600HS cyclic test in sand under σ_v=10 kPa, f=0.5 Hz
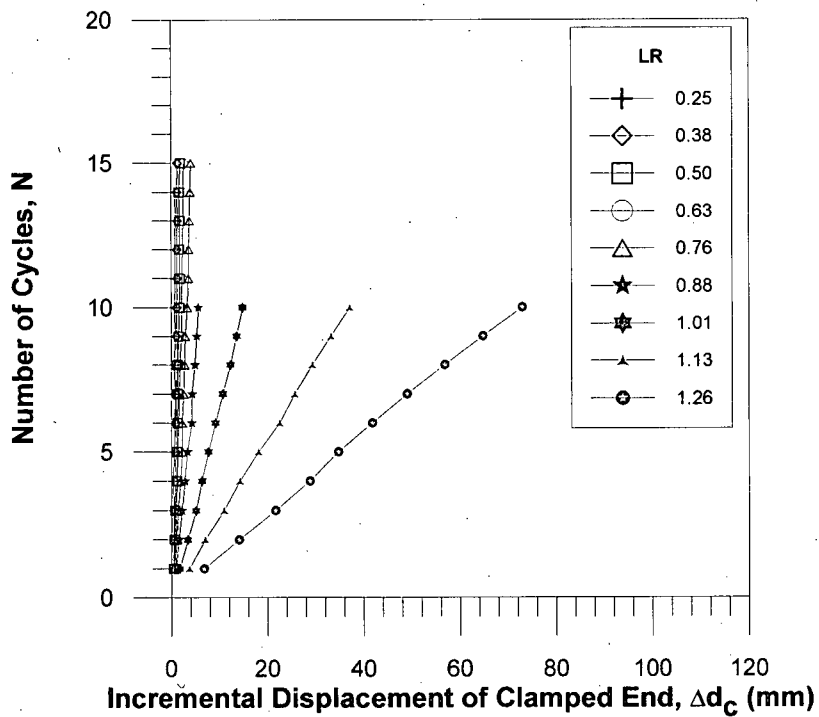
Figure 7.16: Stability curves for a UX1600HS cyclic test in sand under σ_v=20 kPa, f=0.5 Hz
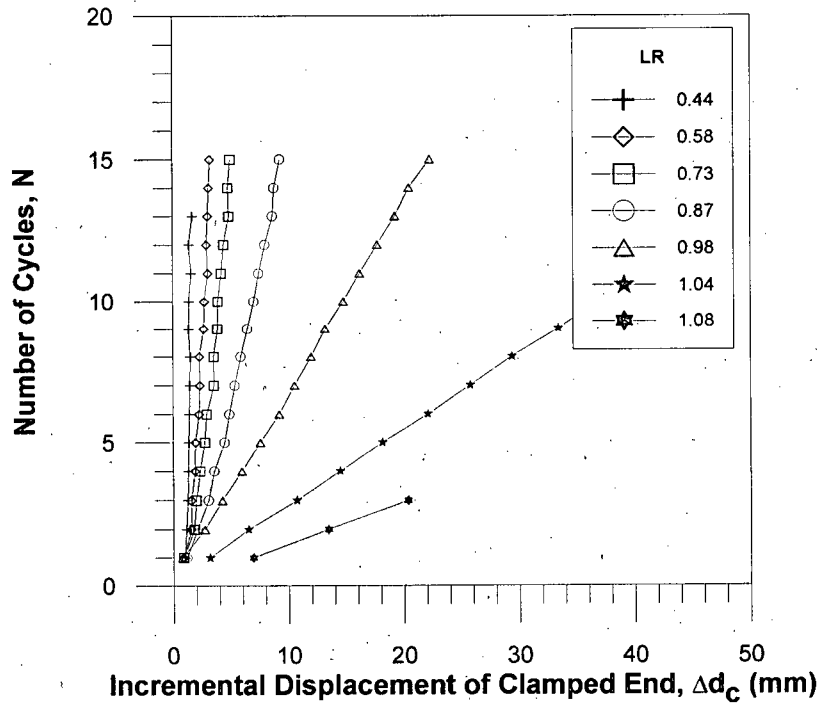
Figure 7.17: Stability curves for a UX1400HS cyclic test in sand under
σ_v=10 kPa, f=0.5 Hz

Figure 7.18: Stability curves for a UX1600HS cyclic test in glass beads
under σ_v=5 kPa, f=0.5 Hz
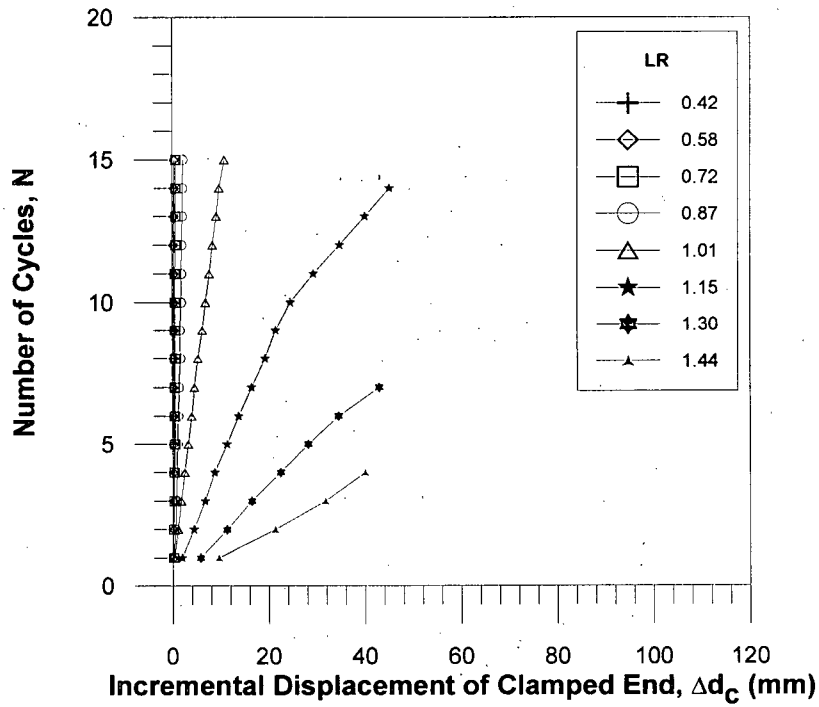
Figure 7.19: Stability curves for a UX1600HS cyclic test in glass beads under σ_v=10 kPa, f=0.5 Hz
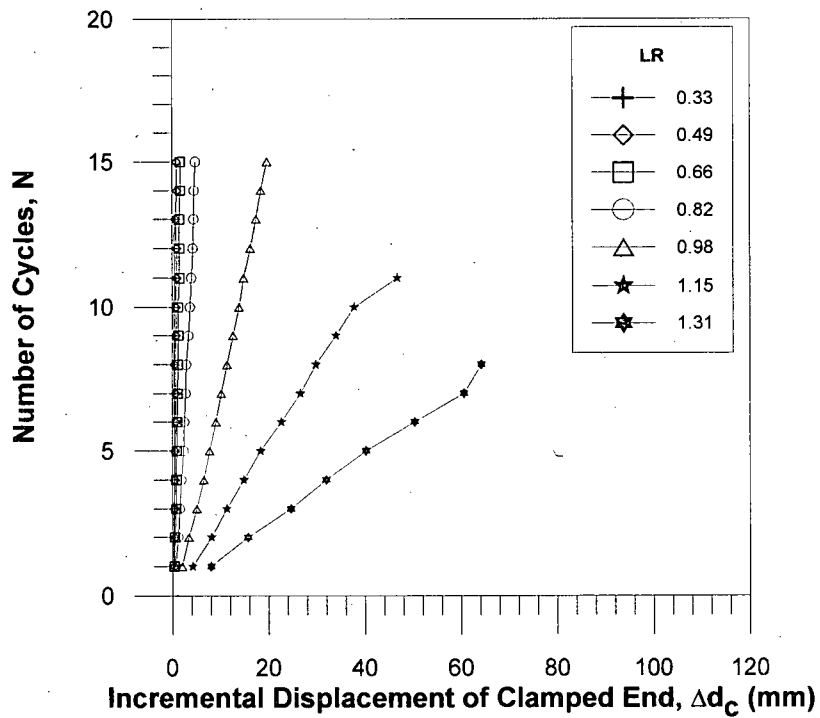
Figure 7.20: Stability curves for a UX1600HS cyclic test in glass beads under σ_v=20 kPa, f=0.5 Hz
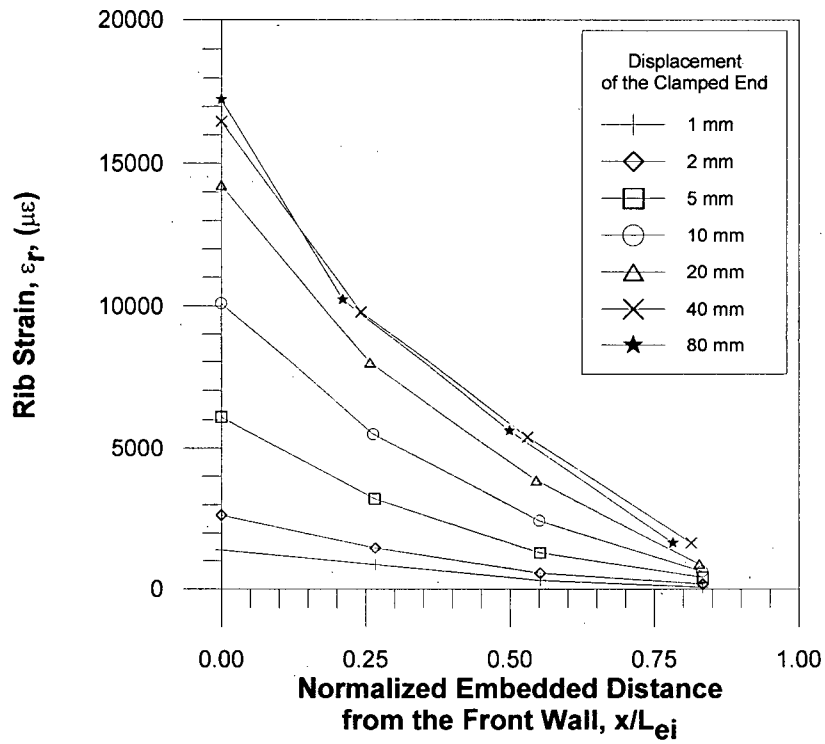
Figure 7.21: Strain profiles for a UX1600HS monotonic test in sand under σ_v=20 kPa at discrete values of clamp displacement
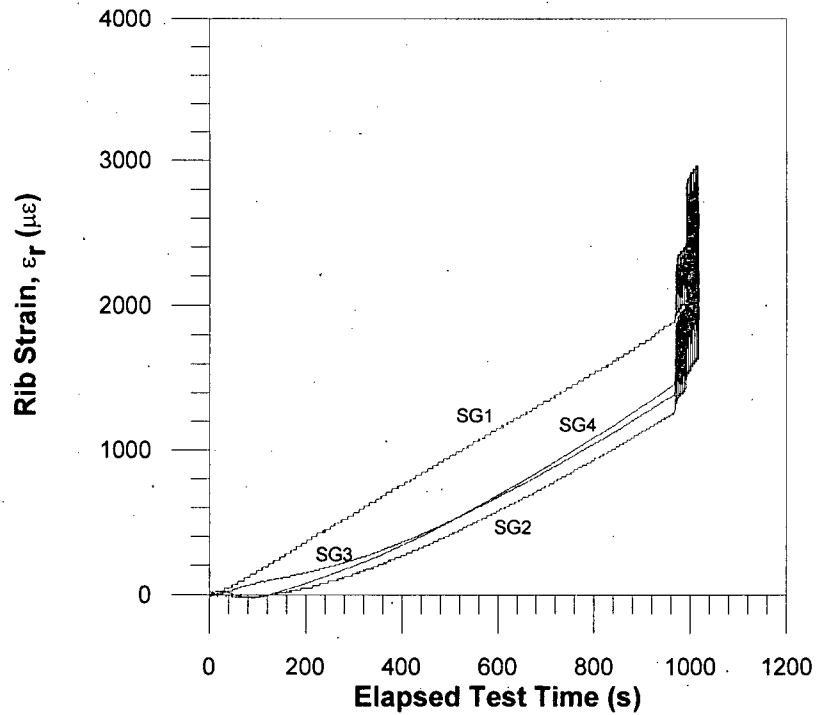
Figure 7.22: Rib strain measured during an in-air test performed on a UX1600HS geogrid (additional cycles were omitted for greater detail)
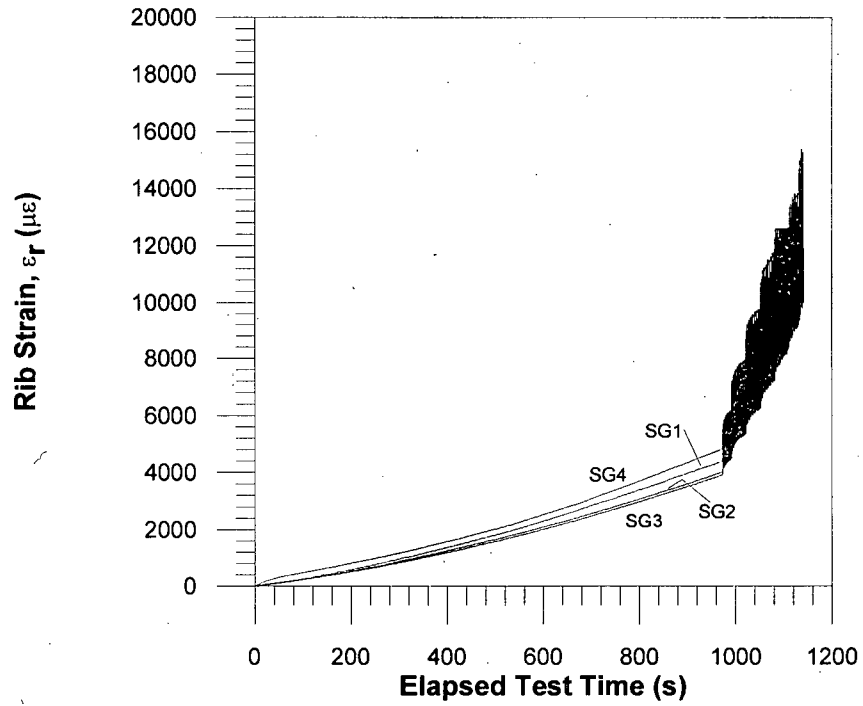
Figure 7.23: Rib strain measured during an in-air test performed on a UX1400HS geogrid (additional cycles were omitted for greater detail)
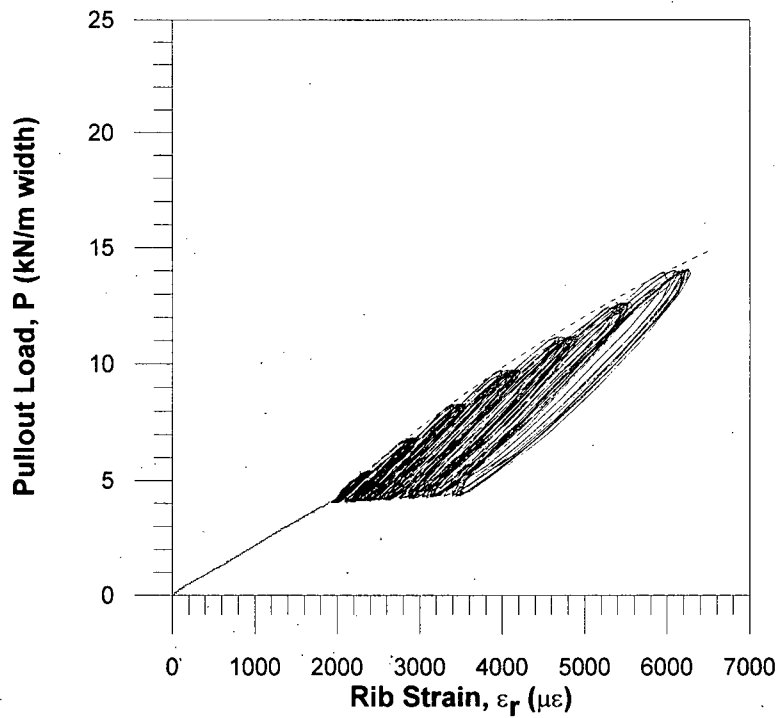
Figure 7.24: The load-strain relationship for SG-2 in the in-air UX1600HS test (the dashed line shows a fitted hyperbolic envelope)
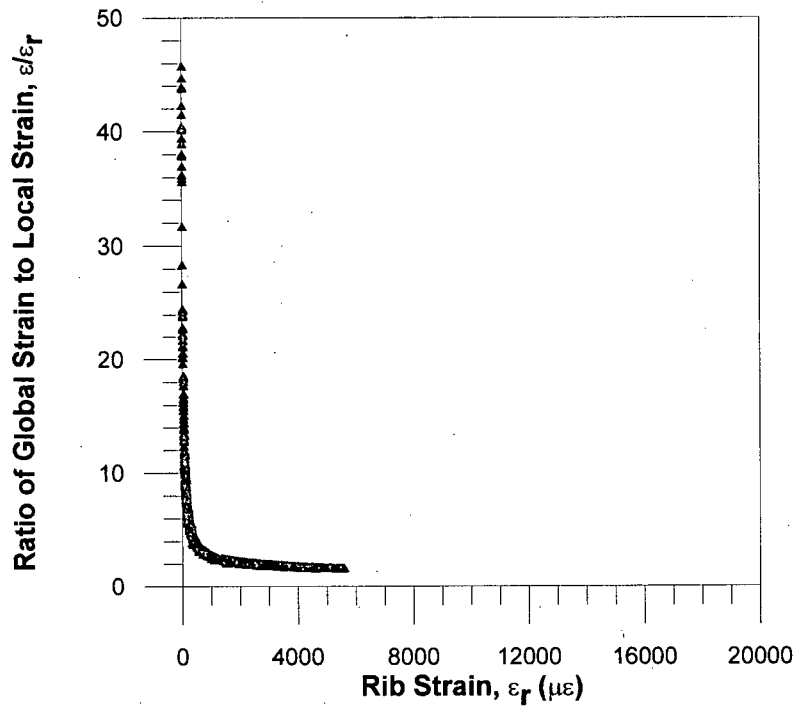
Figure 7.25: Global/local strain relations for the UX1600HS, on SG-2
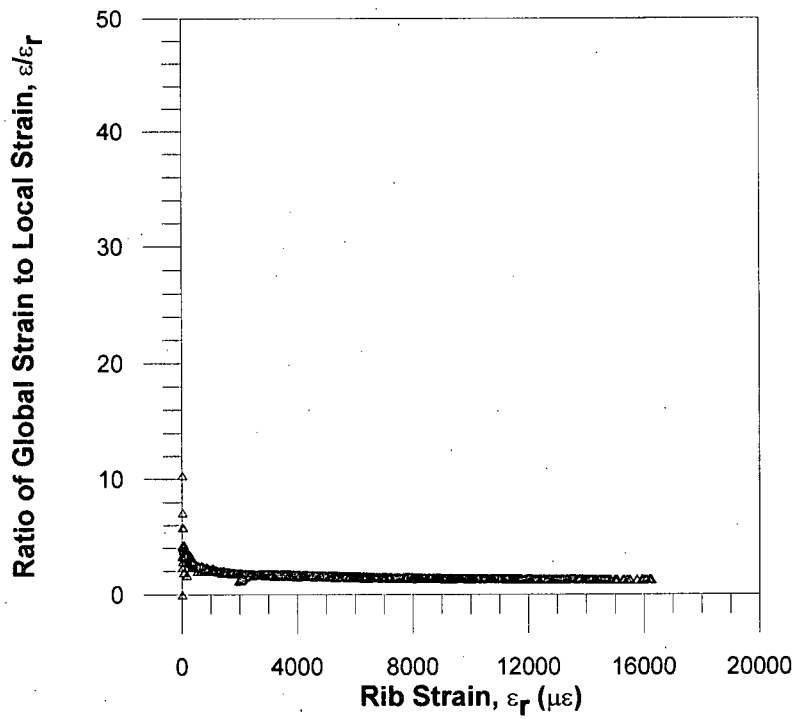
Figure 7.26: Global/local strain relations for the UX1400HS, on SG-2
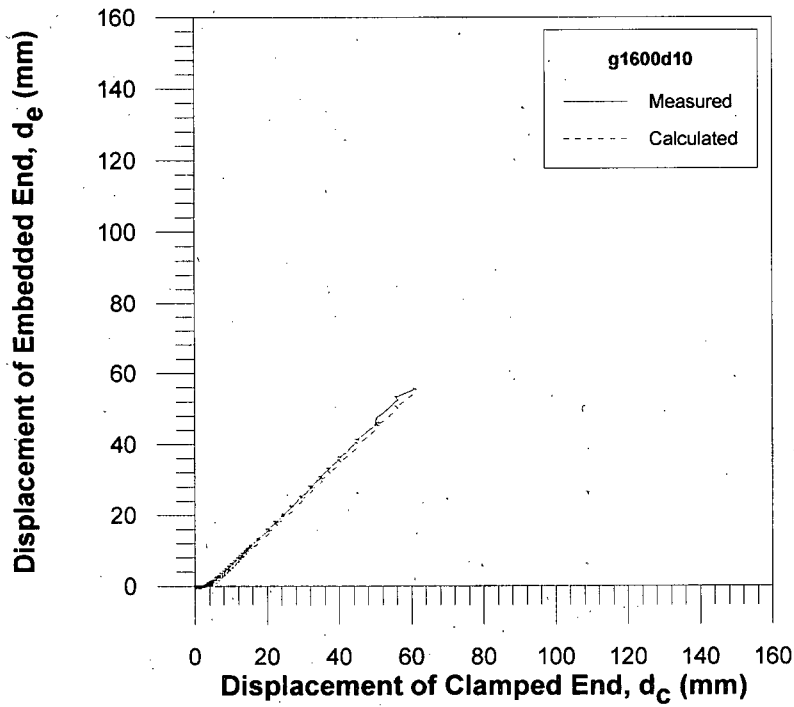
Figure 7.27: A comparison of measured and calculated embedded-end displacements for test g1600d10, using the Generalized Method
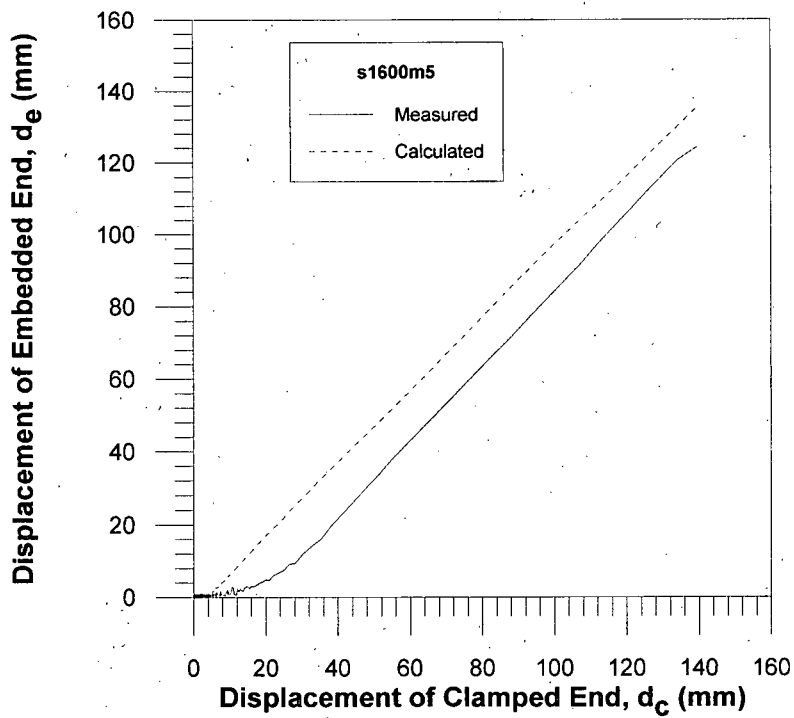
Figure 7.27: A comparison of measured and calculated embedded-end displacements for test s1600m5, using the Generalized Method
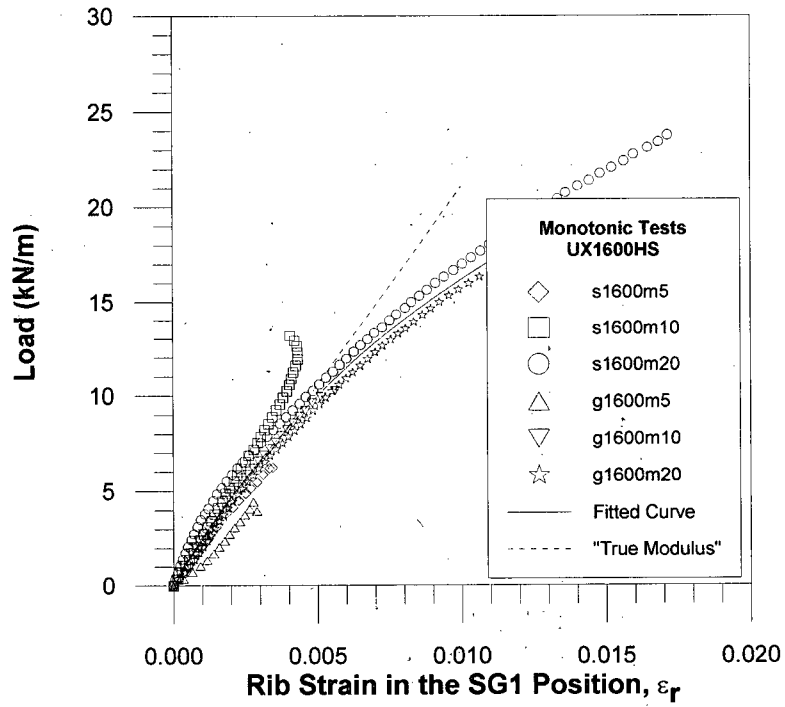
Figure 7.29: Load strain relations observed for the monotonic UX1600HS tests (the "true modulus" is reported by Tensar for the UX1600HS)
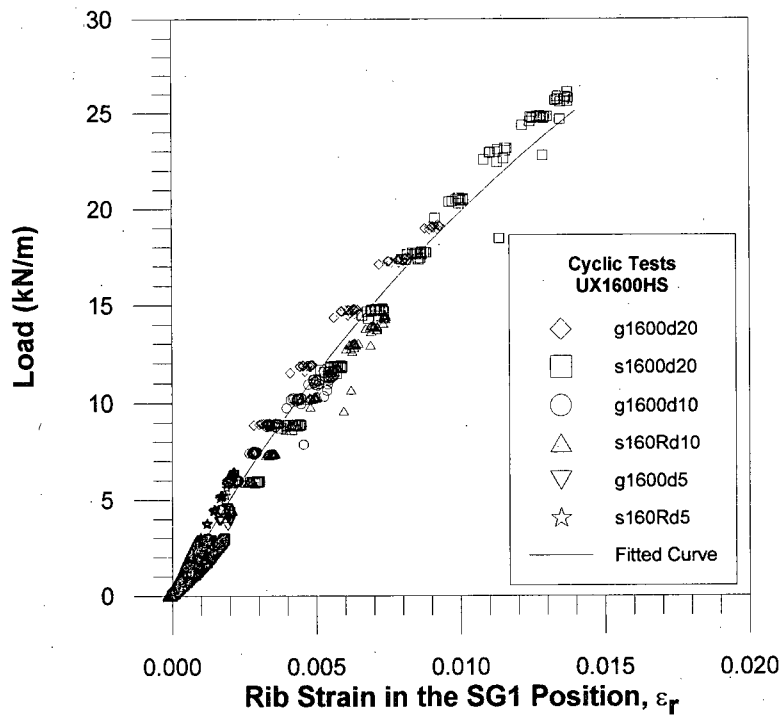
Figure 7.30: Load-strain relations observed for the cyclic UX1600HS tests
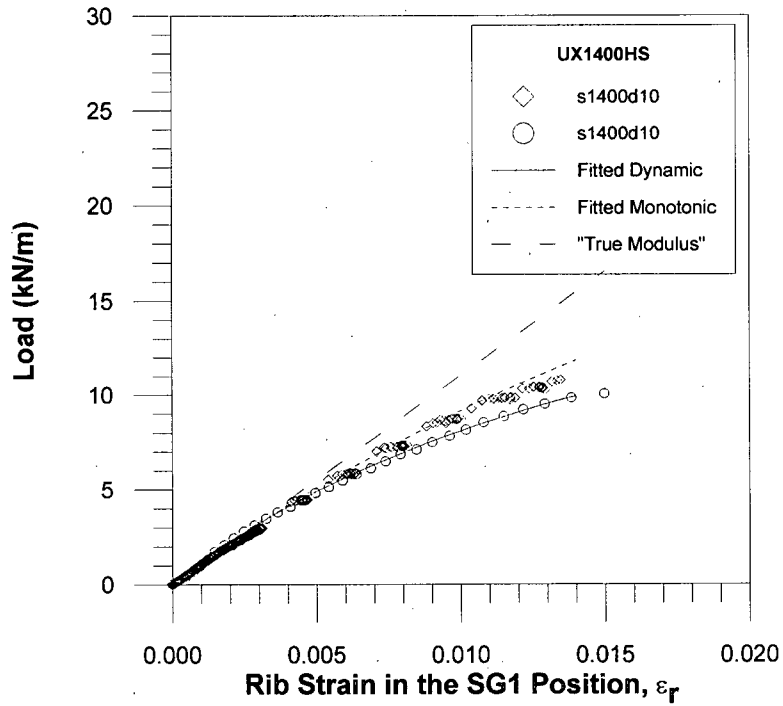
Figure 7.31: Load-strain relations observed for the monotonic and cyclic UX1400HS tests (the "true modulus" is reported by Tensar)
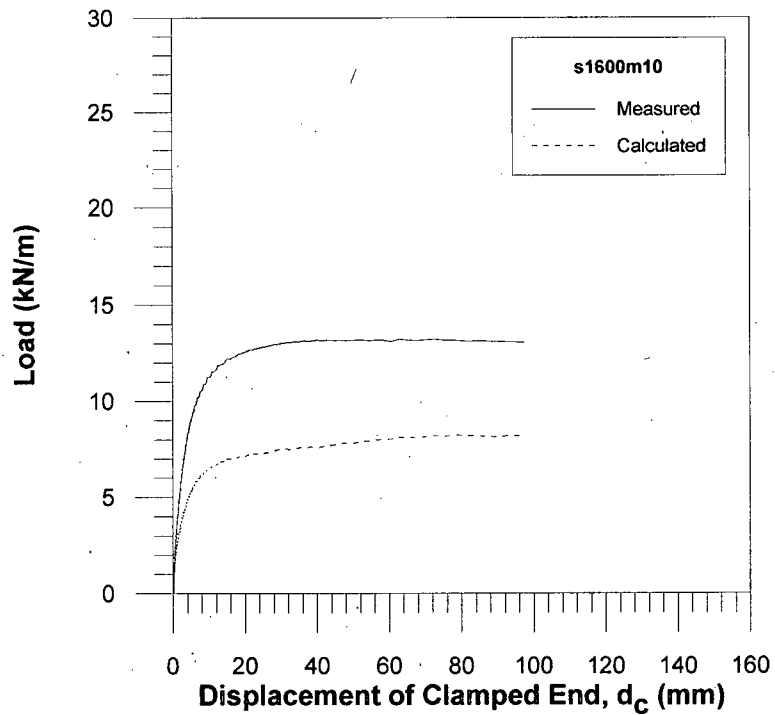
Figure 7.32: A comparison of the measured pullout load versus the calculated pullout using the Generalized Method, for test s1600m10
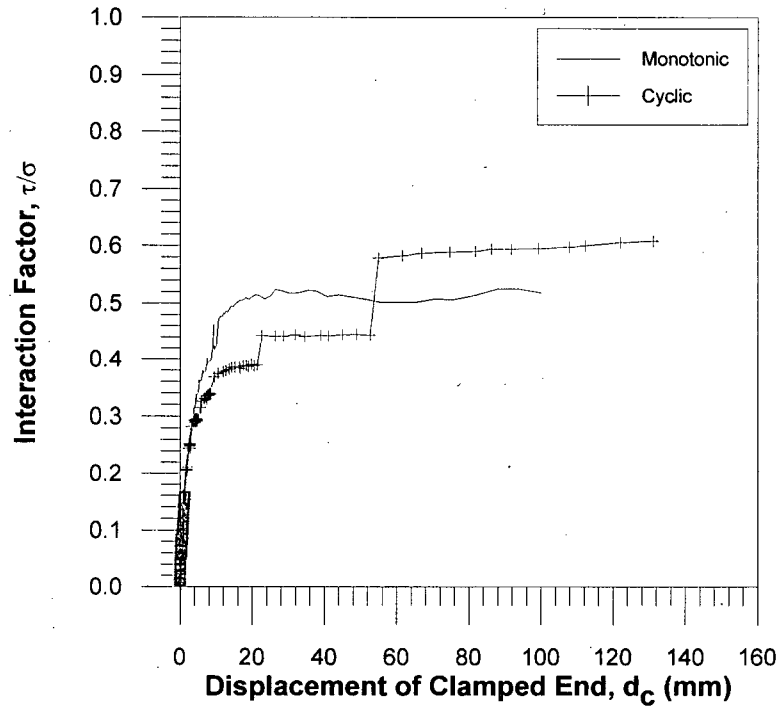
Figure 7.33: Interaction factors calculated by the Generalized Method for the UX1600HS in sand under σ_v=5 kPa
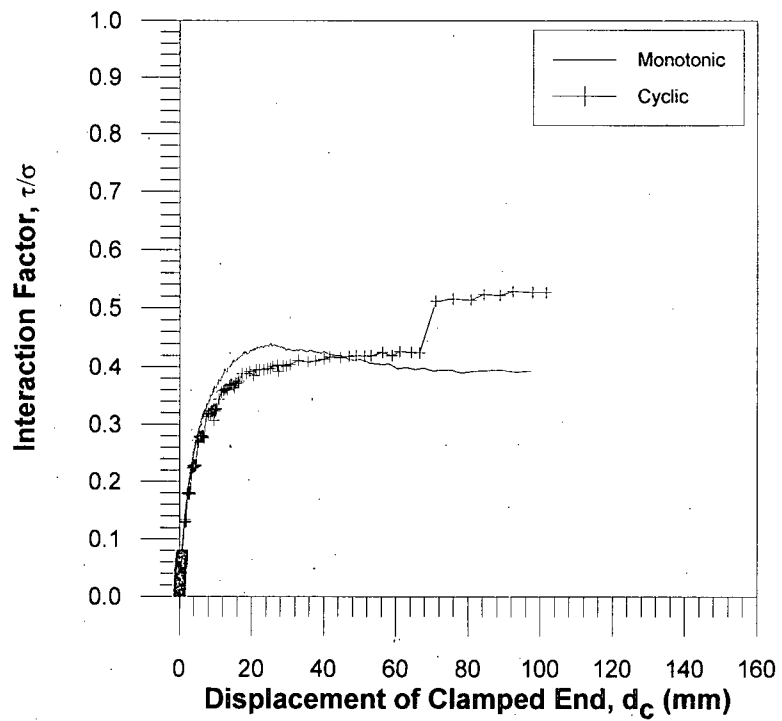
Figure 7.34: Interaction factors calculated by the Generalized Method for the UX1600HS in sand under σ_v=10 kPa
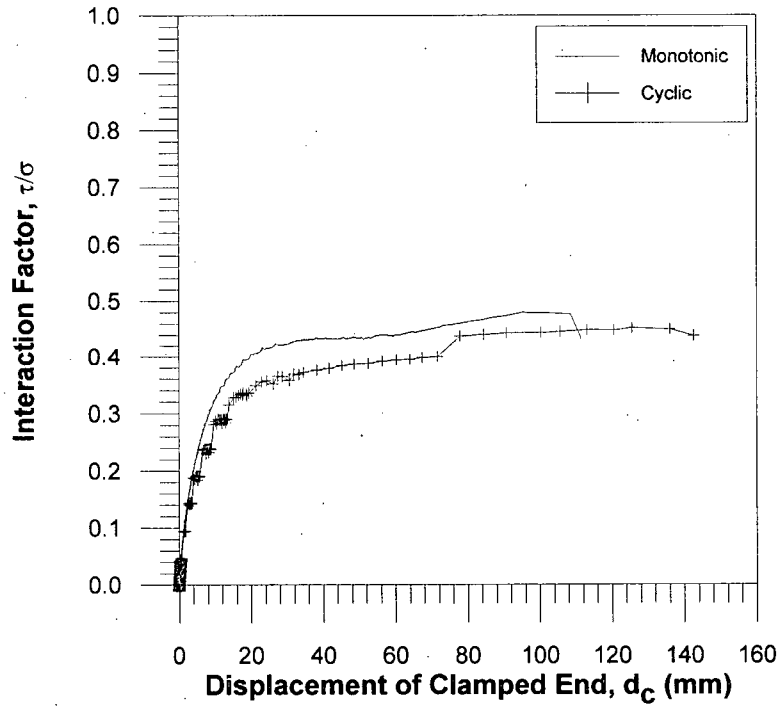
Figure 7.35: Interaction factors calculated by the Generalized Method for the UX1600HS in sand under σ_v=20 kPa
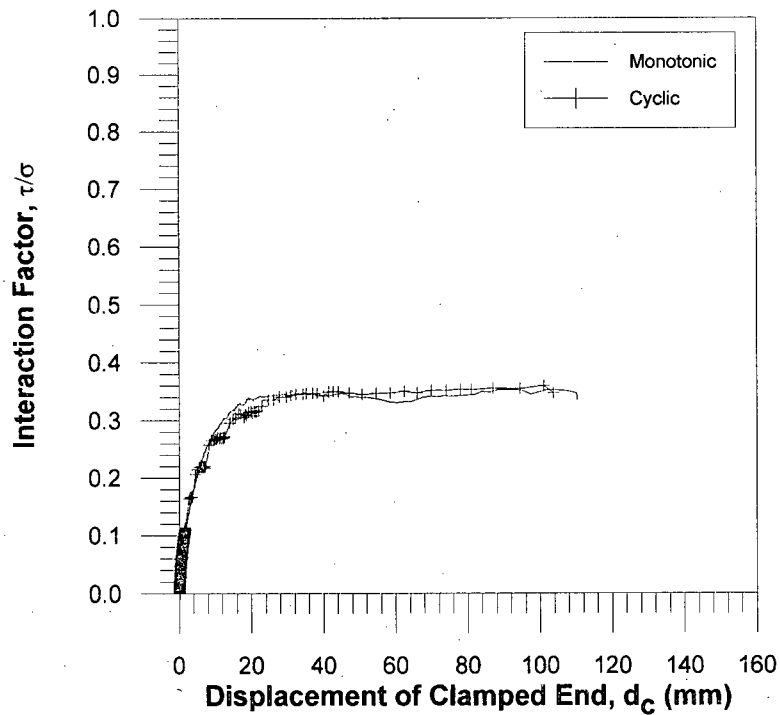
Figure 7.36: Interaction factors calculated by the Generalized Method for the UX1400HS in sand under σ_v=10 kPa
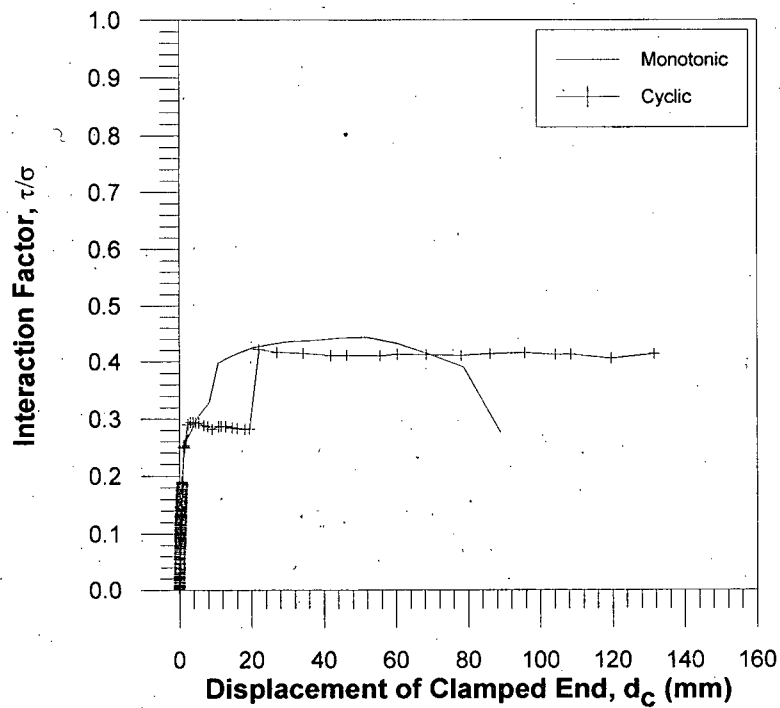
Figure 7.37: Interaction factors calculated by the Generalized Method for the UX1600HS in glass beads under σ_v=5 kPa
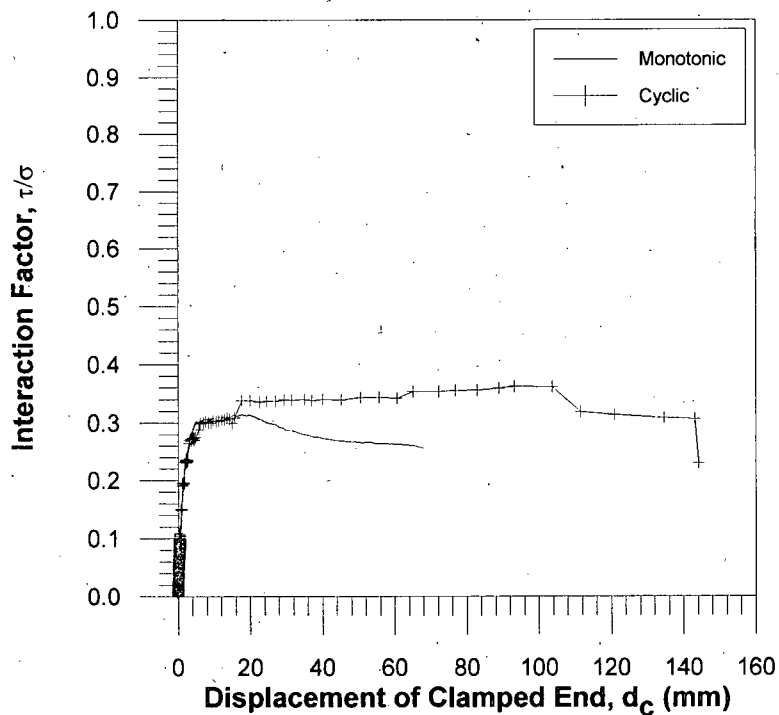
Figure 7.38: Interaction factors calculated by the Generalized Method for the UX1600HS in glass beads under σ_v=10 kPa
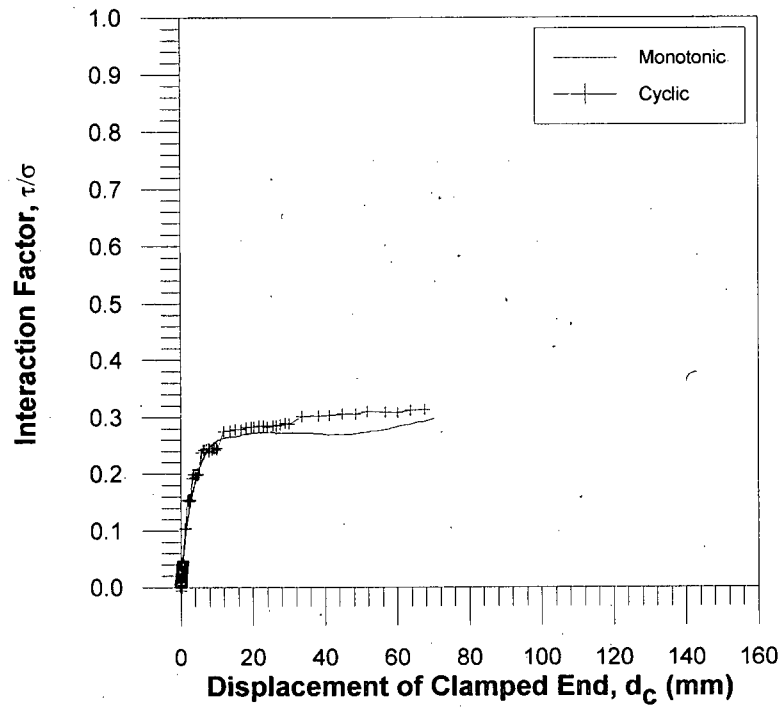
Figure 7.39: Interaction factors calculated by the Generalized Method for the UX1600HS in glass beads under σ_v=20 kPa

CHAPTER 8

CONCLUSIONS AND RECOMMENDATIONS FOR FURTHER STUDY

8.1   Conclusions

The preceding chapters describe the results of a testing program focused on addressing the four objectives set out in Chapter 1. The objectives are centered on describing how the performance of uniaxial geogrids embedded in different granular media under various normal stresses varies in pullout when the loading scheme is dynamic rather than static.

Based on the results and analyses performed on the results, the following general conclusions are drawn:

1. The maximum pullout load sustained by the UX1600HS in the sand material was approximately 20 percent higher than that sustained by the UX1600HS in the glass beads.

2. The spacing and thickness of the geogrids' transverse bearing bars appears to have a significant impact on the maximum pullout load each grid series sustains. More specifically, a closer spacing and greater thickness yield a higher pullout load.

3. Due to the extensible nature of these geogrids, pullout resistance is mobilized progressively along the length of the geogrid.

4. In some tests, compression at the strain gauge locations was noted. This indicates uneven stress distribution along the width of the specimen even though the specimen was loaded evenly across the width of the clamp.

5. Strains measured locally on a rib may not represent the local strain at another location on the rib or the "global" strain over the length of the rib.

6. Tensar geogrid load-strain behavior is non-linear and can best be described by a hyperbolic function.

7. Plastic strains occur at very low strains (on the order of 0.25 percent).

The following specific conclusions are drawn regarding the interaction of the geogrids and soil:

1. Irrespective of the grid series, surcharge pressure, or embedding soil type, the interaction between the soil and geogrid (expressed either as an interaction factor or coefficient of interaction) was found to be approximately equal in static and dynamic loading.

2. The behavior of the geogrid in cyclic pullout remained stable to loads in excess of that sustained in the corresponding monotonic tests.

3. It appears that for cyclic loading, an increase in frequency decreases the likelihood of catastrophic failure. This is due to the reduced time a load in excess of the maximum monotonic load ($P_{P,m}$) is held.

4. While the Improved Total Area Method for calculation of coefficients of interaction is appropriate for a geogrid that is pulling out as an inextensible specimen, the Generalized Method can be used to examine details of soil/geogrid interaction at small strains. However, it appears that the Generalized Method is sensitive to the number of strain gauges supplying strain information and may not account for some of the pullout load being taken up in bearing by the transverse bars.

8.2   Implications for Design Practice

The results generated in this research suggest several items for consideration regarding the analysis and design of GRS structures.

1. It appears that the AASHTO (1998) requirement of discounting by 20 percent the interaction factor for dynamic loading does not adequately describe the behavior for the geogrids tested. However, there still may be valid concern for pullout occurring during a seismic event due to a momentary decrease in the overburden pressure because of vertical ground motion. If this is the case, a more rigorous method of load reduction should be put into place rather than discounting the interaction factor generally.

2. Numerous agencies/organizations have adopted methods for determination of coefficients of interaction (C_i) from pullout tests. A common calculation uses the peak friction angle of a soil (ϕ_p determined from direct shear tests) to calculate a coefficient of interaction for a geosynthetic in pullout. However, this coefficient of interaction applies only when the geosynthetic is moving inextensibly. By the

time this occurs, it is safe to say the soil has mobilized a friction angle considerably less than its peak value. The use of ϕ_p to calculate C_i at large displacement (and hence a pullout resistance) will underestimate the actual capacity of the geosynthetic/soil composite to resist pullout. The designer must be aware of this detail and must select the proper friction angle to account for the possible discount in interaction.

8.3   Recommendations for Future Research

The research performed in this study has raised issues that bear further examination in future studies. The primary issues are:

1. The frequency of loading under a cyclic pullout loading scheme appears to have an impact on the stability of the soil/geogrid composite, or at least on how it may be determined (whether it is measured by a catastrophic failure or by exceeding a given displacement after N cycles of loading). Further data on the stability of GRS may prove useful for determining how dangerous characteristic earthquakes for an area might be for GRS structures based on the measured cyclic frequency and duration of historic seismic events.

2. This research focused only on Tensar geogrids. It would be useful to examine other geogrids to determine whether the ratio of cyclic to monotonic coefficients of interaction is product-specific or general to all products.

3. Limited field data has been released regarding the likelihood of both a horizontal and vertical acceleration in the worst possible combination occurring within a GRS structure, and the likely effects on the structure. In order to address these concerns within a regulatory framework, further research and testing are required.

LIST OF SYMBOLS (NOMENCLATURE)

a'	interaction coefficient
C_i	coefficient of shear stress interaction
$(C_{i,c})_{60}$	coefficient of interaction at d_c=60 mm under cyclic loading
$(C_{i,m})_{60}$	coefficient of interaction at d_c=60 mm under monotonic loading
C_u	coefficient of uniformity
D_{10}	diameter of particles at 10 percent passing
D_{50}	diameter of particles at 50 percent passing
D_{60}	diameter of particles at 60 percent passing
d_c	displacement of clamped end
d_e	displacement of embedded end
D_R	relative density
F*	pullout resistance factor
f	frequency
f_b	bond coefficient
g	gravitational acceleration (9.81 m/s^2)
G_s	specific gravity
L_e	instantaneous geogrid specimen embedded length
L_{ei}	initial geogrid specimen embedded length
L_o	initial geogrid specimen length
LR	load ratio
n	number of rib sections along the length of a geogrid specimen
N	number of cycles at the same amplitude in cyclic loading
P	measured pullout load (kN/m width)
$P_{P,m}$	peak measured monotonic load
P_w	working load, the point at which cyclic loading begins
R_{ci}	ratio of cyclic to monotonic coefficients of interaction (at d_c=60 mm)
r_d	rate of displacement
r_l	rate of loading
W	width of specimen

α	scale effect factor
δ	angle of interface friction
Δd_c	incremental displacement of clamped end
ΔP	amplitude increase of cyclic loads after each set of N cycles
ΔP_N	total amplitude increase above the working load (P_w) at a given cycle set
$\varepsilon_{g,x}$	global strain for the xth rib
ε_r	measured rib strain
ϕ	angle of internal friction
ϕ_{cv}	angle of internal friction at large displacement (constant volume)
ϕ_p, ϕ'_p	peak angle of internal friction
σ, σ_v	vertical (normal) stress
τ	shear stress

BIBLIOGRAPHY

American Association of State Highway Transportation Officials (1998), LRFD Bridge Design Specifications. SI Units, Second Edition. AASHTO, Washington, DC.

Bathurst, R.J. (1998), Segmental Retaining Walls—Seismic Design Manual. First Edition. National Concrete Masonry Association, Herndon, Virginia.

Bathurst, R.J. and Alfaro, M.C. (1997), "Review of seismic design, analysis and performance of geosynthetic reinforced walls, slopes and embankements", *Earth Reinforcement: Proceedings of the International Symposium on Earth Reinforcement, Fukuoka, Kyushu, Japan, 12-14 November, 1996*, A.A. Balkema, Rotterdam, pp. 887-918.

British Standards Institution (1995), Code of Practice for Strengthened/Reinforced Soils and Other Fills. BS 8006. British Standards Institution, London.

Cai, Z. and Bathurst, R.J. (1995). "Seismic Response Analysis of Geosynthetic Reinforced Soil Segmental Retaining Walls by Finite Element Method", *Computers and Geotechnics*, Vol. 17, pp. 523-546.

Christopher, B.R., Gill, S.A., Giroud, J.P., Juran, I., Mitchell, J.K., Schlosser, F., and Dunnicliff, J. (1990), "Design and Construction Guidelines for Reinforced Soil Structures—Volume I", and "Summary of Research—Volume II", *Report No. FHWA-RD-89-043*, Federal Highway Administration, U.S. Department of Transportation.

Houlsby, G.T. (1994), "How the Dilatancy of Soils Affects Their Behaviour", *Proceedings of the Tenth European Conference on Soil Mechanics and Foundation Engineering, Florence, Italy, Volume 4*, A.A. Balkema, Rotterdam, pp. 1189-1202.

International Geosynthetics Society (2000), Recommended Descriptions of Geosynthetics Functions, Geosynthetics Terminology, Mathematical and Graphical Symbols. Fourth Edition. IGS, Easley, South Carolina.

Jewell, R.A., Milligan, G.W.E, Sarsby, R.W., and Dubois, D.D. (1984), "Interaction Between Soil and Geogrids", *Proceedings from the Symposium on Polymer Grid Reinforcement in Civil Engineering*, Thomas Telford, London, pp. 18-30.

Min, Y., Leshchinsky, D., Ling, H.I., and Kaliakin, V.N. (1995), "Effects of Sustained and Repeated Tensile Loads on Geogrid Embedded in Sand", *Geotechnical Testing Jounal*, Vol. 18, No. 2, pp. 204-225.

Moraci, N. and Montanelli, F. (1996), "Short and long term behaviour of geogrids under static and cyclic load", *Earth Reinforcement: Proceedings of the International Symposium on Earth Reinforcement, Fukuoka, Kyushu, Japan, 12-14 November, 1996*, A.A. Balkema, Rotterdam, pp. 117-122.

Perkins, S.W. and Lapeyre, J.A. (1997), "In-Isolation Strain Measurement of Geosynthetics in Wide-Width Strip Tension Test", *Geosynthetics International*, Vol. 4, No. 1, pp. 11-32.

Rad, N.S. and Tumay, M.T. (1987), "Factors Affecting Sand Specimen Preparation by Raining", *Geotechnical Testing Journal*, Vol. 10, No. 1, pp. 31-37.

Raju, D.M. (1991), "Large-Scale Pullout Testing of Geosynthetics", *The University of British Columbia*, thesis.

Raju, D.M. (1995), "Monotonic and Cyclic Pullout Resistance of Geosynthetics", *The University of British Columbia*, thesis.

Raju, D.M. and Fannin, R.J. (1997), "Monotonic and Cyclic Pull-out Resistance of Geogrids", *Geotechnique*, Vol. 47, No. 2, pp. 331-337.

Sandri, D. (1997), "A Performance Summary of Reinforced Soil Structures in the Greater Los Angeles Area after the Northridge Earthquake", *Geotextiles and Geomembranes*, Vol. 15, pp. 235-253.

Simac, M.R., Bathurst, R.J., Berg, R.R., and Lothspeich, S.E. (1997), Design Manual for Segmental Retaining Walls. Second Edition. National Concrete Masonry Association, Herndon, Michigan.

Sitar, N. and Nova-Roessig, L. (1999), "A review of experimental studies of seismic behavior of reinforced soil structures", *Earthquake Geotechnical Engineering: Proceedings of the Second International Conference on Earthquake Geotechnical Engineering, Lisbon, Portugal, 21-25 June 1999*, A.A. Balkema, Rotterdam, pp. 1083-1088.

Tatsuoka, F., Tateyama, M., and Koseki, J. (1996), "Performance of Soil Retaining Walls for Railway Embankments", *Special Issue of Soils and Foundations*, Japanese Geotechnical Society, pp. 311-324.

Vaid, Y.P. and Negussey, D. (1988), "Preparation of Reconstituted Sand Specimens", *Advanced Triaxial Testing of Soil and Rock, ASTM Special Technical Publication 977*, American Society of Testing and Materials, Philadelphia, pp. 405-417.

Wilson-Fahmy, R.F., Koerner, R.M., and Sansone, L.J. (1994), "Experimental Behavior of Polymeric Geogrids in Pullout", *Journal of Geotechnical Engineering*, Vol. 120, No. 4, pp. 661-677.

Yasuda, S., Nagase, H., and Marui, H. (1992), "Cyclic Pullout Tests of Geogrids in Soils", *Earth Reinforcement Practice—Proceedings of the International Symposium on Earth Reinforcement Practice, Fukuoka, Japan, November 1992*, A.A. Balkema, Rotterdam, pp. 185-190.

APPENDIX A

TECHNIQUE OF STRAIN GAUGING PLASTICS

A.1   Introduction

The following text is taken from Raju (1995) with changes made to reflect procedural modifications.

A.2   Strain Gauging Procedure

A.2.1   Materials for Surface Preparation

Rubbing alcohol is used to degrease the surface of the test specimen because of its inertness to polyethylene, and prevents embedment of contaminants in the surface of the geosynthetic specimen. A No. 320 grit sandpaper is used to roughen the surface of the geosynthetic for good bonding between the geosynthetic and the polyamide strain gauge backing. The surface is neutralized with a mild ammonia solution, leaving it slightly alkaline. Gauge installation is performed within a few minutes of completing the surface conditioning.

A.2.2   Adhesives used for Bonding

M-Bond AE 10 adhesive was used to obtain a high-elongation bond. Resin AE with Curing Agent 10 cures in 24 to 48 hours at 24°C to give an elongation capability of 10 percent.

A.2.3   Geosynthetic Surface Preparation

<u>**Supplies required**</u>: isopropyl (rubbing) alcohol, No. 320 grit sandpaper, cotton swabs, compressed air, and M-Prep neutralizer 5.

Steps involved in surface preparation are:

　　1.　Secure the geogrid on a clean, flat surface and mark the strain gauge locations.

2. A clean cotton swab dipped in isopropyl alcohol is rubbed on the strain gauge sites for degreasing and removal of any foreign matter. The isopropyl alcohol evaporates quickly.

3. Using the No. 320 grit sandpaper, roughen the surface of the rib at 45° angles to the axis of the rib in both directions to yield a pattern of cross hatches. This takes approximately 4 minutes. This is best accomplished by sanding in one direction for one minute, blowing off debris with the compressed air, then sanding in the other direction. Blow clean with the compressed air again.

4. Neutralize the strain gauge site with M-Prep Neutralizer, leaving the surface with a mildly alkaline surface.

5. Attach the strain gauge within two or three minutes of completing the surface preparation, using the procedure given below.

A.2.4 Gauge Preparation

Supplies required: plexiglas frame (rectangular hollow), isopropyl alcohol, gauze sponge, tweezers, eraser, MGJ-2 tape, and strain gauges

Steps involved in the preparation are:

1. Clean the plexiglas frame with the isopropyl alcohol using a gauze sponge.

2. Take a small length of MJG-2 tape and attach it to the plexiglas frame causing the tape to be exposed at the hollow portion.

3. Remove the strain gauge from it package with the tweezers, ensuring that it is gripped only at the unused edge.

4. Place the gauge on the exposed tape with the polyamide backing facing up, and aligned parallel to the edge of the tape. Use low pressure from the compressed air supply to ensure the gauge is firmly attached to the tape.

A.2.5 Application of the Gauge

Supplies required: AE 10 adhesive kit, gauze sponge, TFE-1 sheet, silicon pad, aluminum block, and MJG-2 tape

Steps involved in the adhesive preparation and attachment of the gauges are:

1. To prepare the adhesive mix, fill one of the calibrated droppers with Curing Agent 10 exactly to the number 10 imprinted on the side and dispense the contents into the jar of resin AE. Immediately cap the bottle of Curing Agent to avoid moisture absorption.

2. Using a plastic stirring rod supplied, thoroughly mix the Curing Agent and Resin for 5 minutes.

3. The pot life or working time after mixing is 15 to 20 minutes, after which time the adhesive will flash harden, becoming very hot in the process.

4. Lift a tape with strain gauge attached off the plexiglas frame and attach the tape to the geogrid at the desired location, ensuring the gauge is aligned parallel to the rib and the soldering tabs are facing the correct direction. Firmly attach the tape on the opposite side of the tabs to the specimen.

5. Once aligned, peel the tape back on the tab side, roll the tape under and attach the tape to the geogrid so that the gauge is facing polyamide side up with its non-terminal side just barely off the grid.

6. Taking a dentist's scraper, apply several drops of the adhesive to the geogrid in a T-pattern with the top of the T against the lifted tape. This ensures the adhesive will be pushed ahead of the gauge when attaching and will coat the entire area under the gauge.

7. Lift the free end of the tape and using thumb pressure, press the gauge down onto the geogrid from the taped end to the free end in one swift motion. This should align the gauge properly and squeeze any excess adhesive ahead of the gauge.

8. Overlay the gauge with TFE-1 tape, a silicon pad, an aluminum block, and weights to yield a total dead pressure of 135 kPa on the gauge. Allow the adhesive to cure overnight (15 to 20 hours) to obtain a reasonable elongation capability.

9. Discard the adhesive container, stirring rod, and dropper.

10. After the curing time has elapsed, remove the weights, block, pad, and TFE-1 tape, and peel the MJG-2 tape back from the terminal side at an angle of 180 degrees by sliding your thumb swiftly on the folded edge of the tape. This will remove the tape without debonding the gauge.

A.2.6 Gauge Soldering

Supplies required: Rosin solvent, flux, 3-strand wires, soldering iron, dentist's scraper and bent-nose pliers, ohm meter, solder

1. Cut the 3-strand wire to the desired lengths and pass them through the stiff plastic tubing used to protect the wires from damage by the soil.
2. Solder the ends of the wires and trim to leave approximately 5 mm exposed.
3. Using the dentist's scraper, lightly score the soldering pads on the strain gauges to expose the pad and roughen the surface. Clean the pad surfaces with the rosin solvent. Once dry, apply a drop of flux to the tabs.
4. Applying the soldering iron to the tabs, quickly place solder on the tabs of the gauges.
5. Using a thin sliver of duct tape, tape the wires to the geogrid rib so that the wires pass over the soldering tabs. Using the dentist's bent-nose pliers, bend the wires into semicircular shapes, so that the end of the wire is now centered over the soldering tabs. This provides strain relief to the gauge sites. Holding down the wire in the correct location using the scraper, quickly touch the soldering iron to the wire and tab. The wire should settle into the solder on the tab.
6. Clean the gauge surface with rosin solvent. Check the resistance of the gauge using an ohm-meter.
7. Run the protective tubing up against the back of the duct tape, and firmly tape the tubing to the rib using duct tape.

A.2.7 Gauge Protection

Supplies required: Cellophane tape, M-Coat A, TFE-1 and MJG-2 tape.

1. Coat the gauge assembly and wires ahead of the duct tape with M-Coat A, a polyurethane coating, placing three coats at 30 minute intervals.
2. Tape one end of the TFE-1 film to the rib ahead of the gauge site and wrap the film tightly over the gauge, past the start of the protective tubing. Firmly tape the film down to the rib at that point.

A.2.8   Gauge Calibration

Supplies required: shunt resistor

1. Once the geogrid specimen is in place and all gauges have been attached and wired using the procedures given above, turn on the computer and start the testing program.

2. Note the value of strain for SG1 (in bits), then short the positive and negative terminals of the gauge at the Bridge box using the shunt resistor. Note the new value of strain. Repeat this for all strain gauges.

3. Because this resistor of know resistance produces a known "strain", it can be used to provide a calibration factor for each gauge.

APPENDIX B

REASONS FOR ADOPTING COMPACTION AS THE SAMPLE PREPARATION METHOD FOR GLASS BEADS

Soil sample preparation for soil mechanics testing generally encompasses three objectives: to ensure test repeatability, to control in-place density, and to represent a field condition soil "fabric". Assuming the first objective is met, control over density is almost always the paramount concern.

It is generally recognized that soil sample preparation by pluviation to achieve these ends is the preferred technique (Vaid and Negussey 1988, Rad and Turnay 1987). Beyond a certain drop height and given a constant and certain rate of pour, a target density can be achieved with little variation. It should be noted that the research to date appears to have been conducted using medium-grained or larger sands; no work using fine-grained sand or silt size material was found.

Work initially began on pluviating the glass beads using the same apparatus designed for pluviation of the Badger Mining Corporation sand. It quickly became apparent the glass beads, because of their relatively small size, brought a unique set of challenges to placement by pluviation, which are discussed below. These challenges can be summarized by problems with pour rate and placement control.

First, it was discovered that the sudden release of the trap doors required a significant amount of air in a short time to be delivered through the sand sample in the hopper to allow full release of the doors. This was not a problem with the sand, but the naturally dense arrangement of the glass beads inhibited this air flow, resulting in the trap doors opening only half-way and remaining in that position throughout the pour. This resulted in the formation of a bead ridge (approximately 100 to 150 mm higher than the sides) down the central axis of the box. The topographical variation for the sand after a given pour was typically less than 20 mm.

Second, the beads push and entrap air during their travel from the hopper to their final resting places in the box. The resulting air currents distorted and interfered with the vertical drop of the particles, causing particle interaction during the fall and a varied topographical surface of peaks and valleys within the box.

To address the first challenge, the trap doors were sealed open and a PVC mat was fabricated to fit over the perforated twin steel plates, with coincident perforations. The mat was fixed to a wooden frame to provide stability. The idea was to seal the holes on the steel plates while beads were loaded into the hopper and shaped to provide a level surface in the box after pluviation. Once the surface was prepared, the mat was slid into place exposing the holes below and initiating pluvation. The scheme worked somewhat satisfactorily in terms of bypassing the trap doors but the pour rate was still too high and the generated wind currents prevented the formation of a level surface.

It was then discovered that offsetting the holes in the steel plates did not regulate the pour rate sufficiently partly due to design and partly due to lack of precision machining of the steel plates. A search began for materials that could use the twin steel plates for structural support but yet limit the pour rate. Two wire cloth screens (USS 50 and USS 80) were inserted in turn beween the plates and pluviation attempted with varied opening sizes in the twin steel plates. It was found that the 80-mesh cloth clogged and required significant and continuous vibration to sustain flow, regardless of the opening size of the twin plates. To accomplish the proper vibration would have required an expensive and time-consuming retrofit to the hopper to allow direct vibration of the screen. The 50-mesh cloth flowed freely for a time, then slowly clogged, depending on the amount of overburden. This also required vibration, but when vibrated would yield a "pulse" flow that generated a significant wind current due to the high rate of flow. The wind currents produced an uneven surface and prevented even locational spot-pours. It is thought that design of a new pattern of openings and spacings may yield an acceptable flow rate, but at the expense of time, materials, and the erection of a new structural support system for the hopper.

Spatial variation in density through all of this averaged around four to six percent, not significantly higher than the variation encountered in compaction (averaging less than four percent). However, because the pluviation apparatus did not allow the formation of a level surface—even with spot pours—the concern was for the fourth and eighth layers where a screed was required to level the surface by cutting off the peaks and filling the valleys. Tests showed the density of the glass beads soil rolling into a cup at $\rho=1.45$ g/cc whereas the typical pluviated density was $\rho=1.55$ g/cc.

Because the ultimate aim of the thesis was to examine the large-strain behavior of the geogrid in soil, it was decided in light of the above to abandon further attempts to prepare glass beads samples by pluviation and instead compact in-place as described in Chapter 5.